Development of catalysts and capture–reduction processes for N_2O abatement

（N_2O 除去に向けた分解触媒と捕集・還元プロセスの開発）

Chenxi He

Graduate School of Chemical Sciences and Engineering
Hokkaido University

2026

Table of contents

Chapter 1

General Introduction

1.1 Environmental issues of N_2O emissions

Nitrous oxide (N_2O) is a potent greenhouse gas with a global warming potential that is approximately 300 times greater than that of carbon dioxide (CO_2) on a per-mass basis. According to the special report on global warming of the Intergovernmental Panel on Climate Change (IPCC), N_2O is recognized as one of the key greenhouse gases emitted due to anthropogenic activities (**Figure 1.1**). Although N_2O contributes a smaller fraction by mass, the high GWP and longevity make its per-mass climate impact disproportionately large. Moreover, N_2O is a major ozone-depleting substance because it can reach the stratosphere and undergo photolytic decomposition, releasing nitrogen oxides (NO_x) that catalyze ozone breakdown.[1,2]

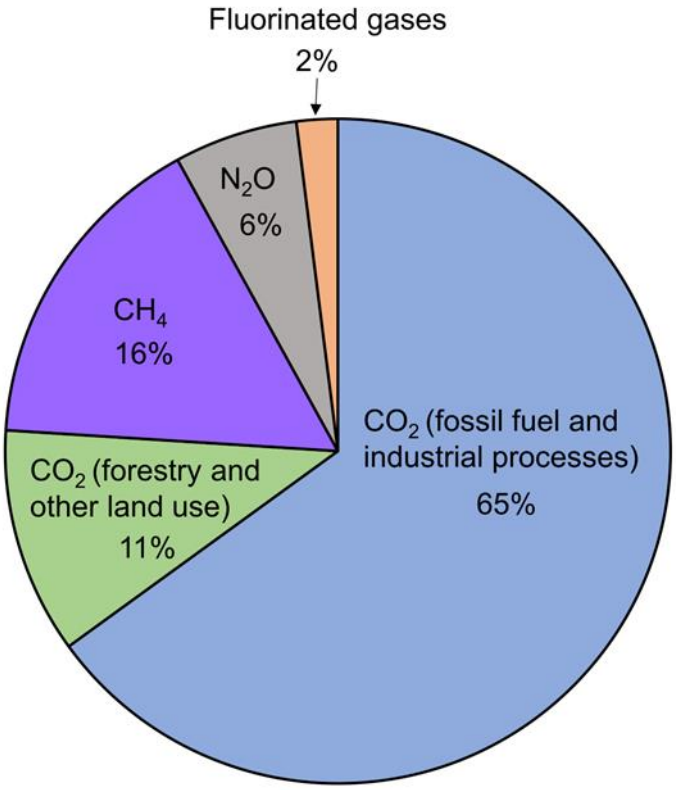

Figure 1.1 Global greenhouse gas emissions by gas from 2010 (IPCC, 2014)

Besides contributing to global warming, emissions of N_2O from industries that use fossil fuels, burn biomass, and chemical plants that produce nitric and adipic acids are increasing annually.[3] As reported in the latest global nitrous oxide budget (**Figure 1.2**), the total annual N_2O emissions have increased by 40 percent in the past four decades (1980-2020). Without global mitigation efforts, N_2O emissions are expected to nearly double by 2050.[4] Therefore, effective catalytic post-treatment technologies must be developed to treat the N_2O emissions from stationary systems and vehicles burning transportation fuels.

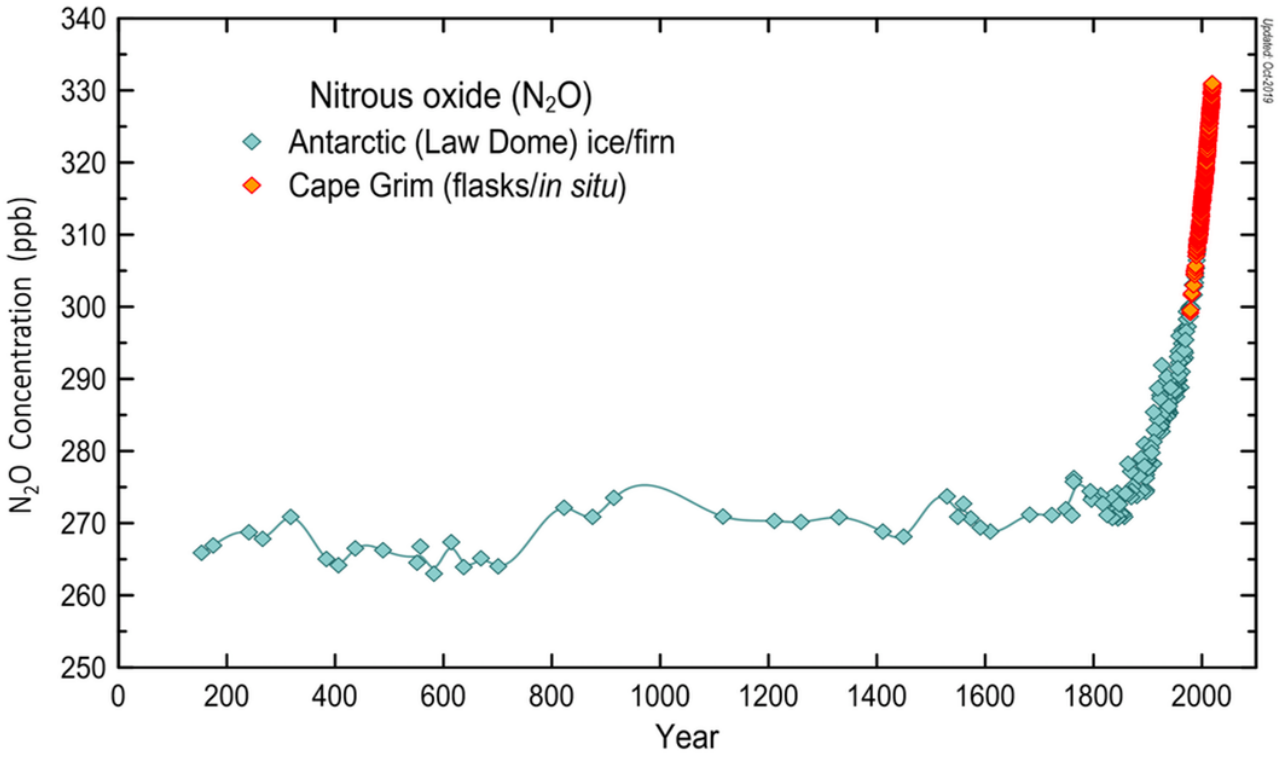

Figure 1.2 Atmospheric nitrous oxide concentrations over the last two millennia

1.2 Catalytic technologies for N_2O abatement

Decomposition of N_2O from exhaust gases of industrial origin is the main step in the abatement of its emission to the atmosphere. Various techniques, including thermal, photocatalytic, and electrocatalytic methods, are available for converting N_2O into harmless N_2. While photocatalytic and electrocatalytic systems can function at room temperature, these approaches are, however, not implemented in industrial-scale applications. Thermal decomposition of N_2O offers a straightforward solution, yet this approach requires extremely high temperatures (ca. >800 °C). Currently, direct decomposition[5–7] and reduction approaches[8–16] are generally considered the two main catalytic strategies for N_2O emissions proven to be effective in reducing N_2O to N_2.

Direct catalytic decomposition is particularly attractive because of its efficiency and the absence of external reducing agents, which lowers the operational costs. Over the past few decades, a wide range of catalysts, including supported noble and metal oxides,[17–20] composite oxides such as perovskites,[21–23] hydrotalcites,[7,24] spinels,[25–28] and zeolite-based catalysts[29–32] have been explored for direct N_2O decomposition. However, these catalysts typically suffer from reduced activity under practical conditions where common inhibitors such as O_2 are present (**Figure 1.3**).[26,33–35] This limitation highlights the need for robust catalysts

that can maintain a high activity in the presence of O_2, making them viable for practical applications.

Among the catalysts studied, Rh is generally considered one of the most effective for N_2O decomposition, especially in the presence of O_2.[33,36–39] However, Rh-based catalysts still require temperatures above 350 °C to achieve sufficient activity under practical conditions. In addition, the high cost of Rh, which exceeds that of most other platinum-group metals, remains a significant barrier to its widespread application. These limitations underscore the need for the development of active and cost-effective catalytic systems.

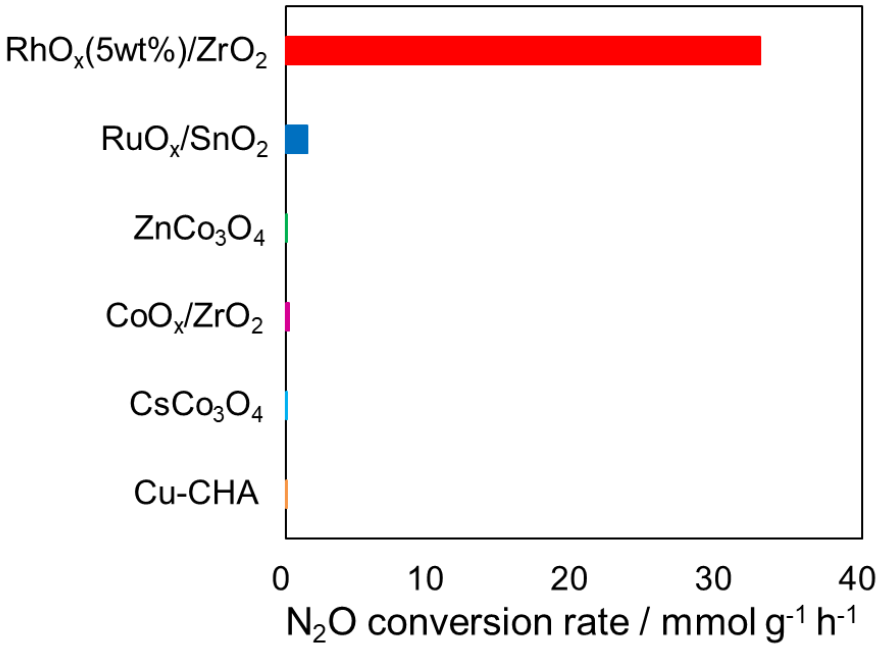

Figure 1.3 Relative comparison of the deN_2O performance of the most active MOs and Rh-based catalysts in the presence of O_2

1.3 Machine learning-assisted catalyst design

Recent developments in molecular and materials informatics have led to a paradigm shift in molecular and materials science, enabling the rational design of functional molecules and materials.[40–43] Although artificial intelligence (AI) has demonstrated proof-of-concept success in accelerating catalyst discovery and significantly reducing the associated time and cost, most studies have been limited to benchmark problems, with few cases leading to the discovery of fundamentally new molecules, materials, or synthetic transformations.[44,45] A major challenge is that machine learning (ML) models typically focus on interpolation within known data rather than extrapolation to unknown high-performance candidates. This limitation is particularly pronounced in catalysis informatics, where the underlying reactions

involve dynamic and time-dependent phenomena.[41,45,46] Furthermore, compared with materials informatics, catalysis research suffers from a lack of large, high-quality datasets because of the prohibitive computational costs of accurately modeling heterogeneous catalysts.[47–50] High-throughput experimental methods for catalysis that have successfully advanced other scientific fields remain underdeveloped.[51–53] Moreover, the scarcity of negative results in catalytic research poses a significant challenge for data-driven approaches.[54] To overcome these challenges, it is critical to develop ML models that can effectively identify novel catalysts within diverse chemical spaces using experimental catalytic data.[46,52,55–58]

Our group has developed an ML approach that employs elemental features, such as electronegativities and melting points, instead of directly using catalyst composition as input representation.[59,60] Each catalyst is represented as a weighted combination of elemental descriptors based on the proportion of each element.[59,60] This method enables catalyst design and discovery in chemical spaces that have little overlap with the training data and allows for the incorporation of elements that were not included in the original dataset, thereby enabling extrapolative predictions. Other studies have confirmed the effectiveness of this strategy using advanced feature engineering and selection techniques.[61] In addition to this theoretical foundation,[59,60,62] we recently applied this approach to the development of multi-elemental reverse water-gas shift catalysts.[63] The composition of optimal catalyst was Pt/Rb–Ba–Mo–Nb/TiO_2. Notably, Nb was not originally present in the dataset, and the resulting catalyst composition was beyond expectations, even by experts. This success demonstrated the ability of ML-driven catalyst design to overcome the limitations of conventional intuition-based exploration. However, although this approach successfully identified novel high-performance catalysts, it was limited to a single catalytic system, focusing only on the effect of additive oxides while keeping Pt and TiO_2 fixed as the support metal and support, respectively. More recently, we extended our extrapolative ML strategy to develop new multi-elemental catalysts for the selective catalytic reduction of NO_x using H_2 (H_2-SCR)[64] and low-temperature methanol synthesis from CO_2 and H_2[65]. The optimal catalysts for these reactions were found to be Pt–Ir/Ba–Co/H-ZSM-5 and Pt/Mo–Re–W/TiO_2, respectively. These studies further highlighted the potential of ML for identifying unexpected and highly efficient catalytic systems. There is a strong demand to apply this ML approach to other valuable catalytic reaction processes.

1.4 Continuous capture–reduction system

Besides development of high-performance catalysts to decompose N_2O, integrated capture and conversion systems have recently emerged as a promising approach for a low-energy-consumption method for effective N_2O removal from mixed tail gas.[66–74] For instance, this system for CO_2 utilization employs CO_2 adsorbents and CO_2 reduction materials that can operate in various reactors.[75–77] This process can be used for CO_2 transformation in the presence of O_2 because the chemical absorption of CO_2 is not inhibited by O_2, and H_2 as a reductant is not simultaneously introduced into the same reactor as O_2. This is advantageous from a practical viewpoint because O_2 is often present in waste gases containing CO_2.

Inspired by these integrated capture and conversion strategies, we developed a continuous capture and reduction system that uses porous adsorbents as N_2O adsorbents and Pd nanoparticles on La-containing Al_2O_3 (Pd/La/Al_2O_3) as the reduction catalyst. Specifically, a separate fixed-bed flow system was utilized to continuously perform N_2O capture and reduction experiments. Two reactors filled with adsorbents were set in parallel, where one reactor selectively captured N_2O from a mixture gas feed, and the other released N_2O under a flow of He by heating the adsorbents. The desorbed N_2O was subsequently fed into the downstream reactor containing a Pd/La/Al_2O_3 catalyst to reduce N_2O to N_2.

1.5 Thesis outline

In this thesis, the attention will be focused on the design and development of high-performance catalysts and processes for N_2O abatement. This thesis will be divided into the following chapters:

Chapter 2: Machine learning-assisted development of high-performance catalysts for direct N_2O decomposition

An extrapolated machine learning (ML) method was employed to develop highly efficient catalysts for low-temperature N_2O decomposition. Starting with an initial dataset of 51 catalysts, we conducted 37 iterations of a closed loop discovery system (ML predictions + experimental validation), testing a total of 633 catalysts. Among them, Rh(1)–Pd(2)/ZrO_2_EP exhibited the highest catalytic performance for N_2O decomposition. Moreover, this data-driven approach also led to the discovery of effective non-Rh-containing catalysts with activities approaching those of the Rh-based system. Through control experiments and a combination of *ex situ* and *in situ* characterizations, the essential role of each component in the optimal catalyst, Rh(1)–Pd(2)/ZrO_2_EP, was identified.

Chapter 3: Continuous N_2O capture and reduction to N_2 using Ca-zeolite adsorbent and Pd/La/Al_2O_3 reduction catalyst

Inspired by the integrated chemical-looping strategy, we developed an N_2O capture and reduction system that uses CaO-incorporated zeolites (Ca-zeolites) as N_2O adsorbents and Pd nanoparticles on La-containing Al_2O_3 (Pd/La/Al_2O_3) as the reduction catalyst. This new process is suitable for continuous operation under temperature-swing cycling between 50 and 150 °C. The N_2O capture capacity and subsequent reduction ability were maintained for at least 15 h (10 cycles). Notably, this process can be performed at low temperatures (below 150 °C) via a simple temperature-swing operation in the presence of O_2.

Chapter 4: Enhanced N_2O capture and reduction system using Cu/zeolite adsorbent and Pd/La/Al_2O_3 catalyst under O_2-CO_2-rich conditions

A series of materials were investigated to test N_2O adsorption and Cu oxides supported on CHA-type zeolite (Cu/CHA) were identified as an efficient N_2O adsorbent in environments containing both O_2 and CO_2. Using the Cu/CHA adsorbent, we developed an N_2O capture and reduction system that could operate effectively in the presence of O_2 and CO_2 at low temperatures (below 150 °C) for at least 12 h.

1.6 Reference

(1) Ravishankara, A. R.; Daniel, J. S.; Portmann, R. W. Nitrous Oxide (N_2O): The Dominant Ozone-Depleting Substance Emitted in the 21st Century. *Science (1979)* **2009**, *326* (5949), 123–125.
(2) Li, L.; Xu, J.; Hu, J.; Han, J. Reducing Nitrous Oxide Emissions to Mitigate Climate Change and Protect the Ozone Layer. *Environ. Sci. Technol.* **2014**, *48* (9), 5290–5297.
(3) Pérez-Ramírez, J.; Kapteijn, F.; Schöffel, K.; Moulijn, J. A. Formation and Control of N_2O in Nitric Acid Production: Where Do We Stand Today? *Appl Catal B* **2003**, *44*, 117–151.
(4) Konsolakis, M. Recent Advances on Nitrous Oxide (N_2O) Decomposition over Non-Noble-Metal Oxide Catalysts: Catalytic Performance, Mechanistic Considerations, and Surface Chemistry Aspects. *ACS Catal* **2015**, *5*, 6397–6421.
(5) Kapteijn, F.; Rodriguez-Mirasol, J.; Moulijn, J. A. Heterogeneous Catalytic Decomposition of Nitrous Oxide. *Appl. Catal., B* **1996**, *9* (1–4), 25–64.
(6) Jabłońska, M.; Palkovits, R. Nitrogen Oxide Removal over Hydrotalcite-Derived Mixed Metal Oxides. *Catal. Sci. Technol.* **2016**, *6* (1), 49–72.
(7) Jablońska, M.; Arán, M. A.; Beale, A. M.; Delahay, G.; Petitto, C.; Nocuń, M.; Palkovits, R. Understanding the Origins of N_2O Decomposition Activity in Mn(Fe)CoAlO Hydrotalcite Derived Mixed Metal Oxides. *Appl. Catal., B* **2019**, *243*, 66–75.
(8) Beale, A. M.; Gao, F.; Lezcano-Gonzalez, I.; Peden, C. H. F.; Szanyi, J. Recent Advances in Automotive Catalysis for NOx Emission Control by Small-Pore Microporous Materials. *Chem. Soc. Rev.* **2015**, *44* (20), 7371–7405.
(9) Lee, E.; Lee, J.; Park, D. C.; Moon, S.; Song, I.; Jung, H.; Kim, D. H. Pd Nanoparticles Fixed in Zeolites Promote Low-Temperature NO Reduction via Hydrogen Spillover. *Appl. Catal., B* **2025**, *366*, 125060.
(10) Lin, B.; Guo, Z.; Tang, J.; Chen, P.; Ye, D.; Hu, Y. Modulating the Microstructure and Surface Acidity of MnO_2 by Doping-Induced Phase Transition for Simultaneous Removal of Toluene and NO_x at Low Temperature. *Environ. Sci. Technol.* **2024**, *58* (23), 10398–10408.
(11) Xiong, T.; Xiao, G.; Lin, B.; Li, Q.; Fu, M.; Hu, Y. V_2O_5 Modified Mn/SAPO-34 Catalyst for the Synchronous Elimination of NO_x and Volatile Organic Compounds. *Catal. Today* **2024**, *430*, 114535.
(12) Shi, Z.; Sun, H.; Wang, L.; Deng, Q.; Gong, C. X.; Han, L.; Li, K.; Deng, W.; Zhu, Y. A.; Li, Z.; Chen, H.; Zhu, K. Generating Silicon-Rich AFX Zeolite Using Rigid Diquaternary Alkylammonium Structure Directing Agent towards Stable Selective Catalytic Reduction of NO_x by NH_3. *Appl. Catal., B* **2024**, *344*, 123637.
(13) Han, F.; Sun, H.; Zhao, Z.; Xu, Y.; Dong, H.; Liu, W.; Sun, L.; Wang, Z.; Hou, G.; Kitano, M.; Li, W.; Shen, M.; Chen, H. Selective Catalytic Reduction of NO_x by Methanol on Metal-Free Zeolite with Brønsted and Lewis Acid Pair. *ACS Catal.* **2022**, *12* (4), 2403–2414.
(14) Shibata, J.; Hashimoto, M.; Shimizu, K. I.; Yoshida, H.; Hattori, T.; Satsuma, A. Factors Controlling Activity and Selectivity for SCR of NO by Hydrogen over Supported Platinum Catalysts. *J. Phys. Chem. B* **2004**, *108* (47), 18327–18335.
(15) Buttignol, F.; Garbujo, A.; Biasi, P.; Kröcher, O.; Ferri, D. N_2O Activation and NO Adsorption Control the Simultaneous Conversion of N_2O and NO Using NH_3 over Fe-ZSM-5. *J. Am. Chem. Soc.* **2025**, *147* (10), 8978.
(16) Buttignol, F.; Fischer, J. W. A.; Clark, A. H.; Elsener, M.; Garbujo, A.; Biasi, P.; Czekaj, I.; Nachtegaal, M.; Jeschke, G.; Kröcher, O.; Ferri, D. Iron-Catalysed Cooperative Redox Mechanism for the Simultaneous Conversion of Nitrous Oxide and Nitric Oxide. *Nat. Catal.* **2024**, *7* (3), 1305.

(17) Oi, J.; Obuchi, A.; Bamwenda, G. R.; Ogata, A.; Yagita, H.; Kushiyama, S.; Mizuno, K. Decomposition of Nitrous Oxide over Supported Rhodium Catalysts and Dependency on Feed Gas Composition. *Appl. Catal., B* **1997**, *12*, 277–286.
(18) Hinokuma, S.; Iwasa, T.; Kon, Y.; Taketsugu, T.; Sato, K. N_2O Decomposition Properties of Ru Catalysts Supported on Various Oxide Materials and SnO_2. *Sci. Rep.* **2020**, *10* (1), 21605.
(19) Hinokuma, S.; Iwasa, T.; Kon, Y.; Taketsugu, T.; Sato, K. Effects of Support Materials and Ir Loading on Catalytic N_2O Decomposition Properties. *Catal. Commun.* **2021**, *149*, 106208.
(20) Kaczmarczyk, J.; Zasada, F.; Janas, J.; Indyka, P.; Piskorz, W.; Kotarba, A.; Sojka, Z. Thermodynamic Stability, Redox Properties, and Reactivity of Mn_3O_4, Fe_3O_4, and Co_3O_4 Model Catalysts for N_2O Decomposition: Resolving the Origins of Steady Turnover. *ACS Catal.* **2016**, *6* (2), 1235–1246.
(21) Peña, M. A.; Fierro, J. L. G. Chemical Structures and Performance of Perovskite Oxides. *Chem Rev* **2001**, *101* (7), 1981–2017.
(22) Richards, N.; Carter, J. H.; Parker, L. A.; Pattisson, S.; Hewes, D. G.; Morgan, D. J.; Davies, T. E.; Dummer, N. F.; Golunski, S.; Hutchings, G. J. Lowering the Operating Temperature of Perovskite Catalysts for N_2O Decomposition through Control of Preparation Methods. *ACS Catal.* **2020**, *10* (10), 5430–5442.
(23) Simböck, J.; Ghiasi, M.; Schönebaum, S.; Simon, U.; de Groot, F. M. F.; Palkovits, R. Electronic Parameters in Cobalt-Based Perovskite-Type Oxides as Descriptors for Chemocatalytic Reactions. *Nat Commun* **2020**, *11* (1), 1–10.
(24) Armor, J. N.; Braymer, T. A.; Farris, T. S.; Li, Y.; Petrocelli, F. P.; Weist, E. L.; Kannan, S.; Swamy, C. S. Calcined Hydrotalcites for the Catalytic Decomposition of N_2O in Simulated Process Streams. *Appl. Catal., B* **1996**, *7* (3–4), 397–406.
(25) Russo, N.; Fino, D.; Saracco, G.; Specchia, V. N_2O Catalytic Decomposition over Various Spinel-Type Oxides. *Catal. Today* **2007**, *119* (1–4), 228–232.
(26) Asano, K.; Ohnishi, C.; Iwamoto, S.; Shioya, Y.; Inoue, M. Potassium-Doped Co_3O_4 Catalyst for Direct Decomposition of N_2O. *Appl. Catal., B* **2008**, *78* (3–4), 242–249.
(27) Stelmachowski, P.; Maniak, G.; Kotarba, A.; Sojka, Z. Strong Electronic Promotion of Co_3O_4 towards N_2O Decomposition by Surface Alkali Dopants. *Catal. Commun.* **2009**, *10* (7), 1062–1065.
(28) Grzybek, G.; Stelmachowski, P.; Gudyka, S.; Indyka, P.; Sojka, Z.; Guillén-Hurtado, N.; Rico-Pérez, V.; Bueno-López, A.; Kotarba, A. Strong Dispersion Effect of Cobalt Spinel Active Phase Spread over Ceria for Catalytic N_2O Decomposition: The Role of the Interface Periphery. *Appl. Catal., B* **2016**, *180*, 622–629.
(29) Lin, F.; Andana, T.; Wu, Y.; Szanyi, J.; Wang, Y.; Gao, F. Catalytic Site Requirements for N_2O Decomposition on Cu-, Co-, and Fe-SSZ-13 Zeolites. *J. Catal.* **2021**, *401*, 70–80.
(30) Bols, M. L.; Snyder, B. E. R.; Rhoda, H. M.; Cnudde, P.; Fayad, G.; Schoonheydt, R. A.; Van Speybroeck, V.; Solomon, E. I.; Sels, B. F. Coordination and Activation of Nitrous Oxide by Iron Zeolites. *Nat. Catal.* **2021**, *4* (4), 332–340.
(31) Kondratenko, E. V.; Pérez-Ramírez, J. Mechanism and Kinetics of Direct N_2O Decomposition over Fe-MFI Zeolites with Different Iron Speciation from Temporal Analysis of Products. *J. Phys. Chem. B* **2006**, *110* (45), 22586–22595.
(32) Pérez-Ramírez, J.; Hevia, M. A. G.; Abelló, S. SO_2-Promoted Catalytic N_2O Removal over Iron Zeolites. *Chem. Commun.* **2008**, No. 42, 5351–5353.
(33) Satsuma, A.; Maeshima, H.; Watanabe, K.; Suzuki, K.; Hattori, T. Effects of Methane and Oxygen on Decomposition of Nitrous Oxide over Metal Oxide Catalysts. *Catal. Today* **2000**, *63*.

(34) Ohnishi, C.; Asano, K.; Iwamoto, S.; Chikama, K.; Inoue, M. Alkali-Doped Co_3O_4 Catalysts for Direct Decomposition of N_2O in the Presence of Oxygen. *Catal. Today* **2007**, *120* (2), 145–150.
(35) Giecko, G.; Borowiecki, T.; Gac, W.; Kruk, J. Fe_2O_3/Al_2O_3 Catalysts for the N_2O Decomposition in the Nitric Acid Industry. *Catal. Today* **2008**, *137* (2–4), 403–409.
(36) Parres-Esclapez, S.; López-Suárez, F. E.; Bueno-López, A.; Illán-Gómez, M. J.; Ura, B.; Trawczynski, J. Rh-Sr/Al_2O_3 Catalyst for N_2O Decomposition in the Presence of O_2. *Top. Catal.* **2009**, *52* (13–20), 1832–1836.
(37) Zhang, N.; He, C.; Jing, Y.; Qian, Y.; Toyao, T.; Shimizu, K. ichi. Enhanced N_2O Decomposition on Rh/ZrO_2 Catalysts through the Promotional Effect of Palladium. *Surf. Interface* **2024**, *46*.
(38) Jing, Y.; He, C.; Zhang, N.; Murano, Y.; Toyoshima, R.; Kondoh, H.; Kageyama, Y.; Inomata, H.; Toyao, T.; Shimizu, K. I. Promotional Effect of Ag on the Catalytic Decomposition of N_2O in the Presence of O_2 over the Al_2O_3-Supported Rh Catalyst. *ACS Catal.* **2023**, *13* (19), 12983–12993.
(39) Zhang, N.; He, C.; Jing, Y.; Qian, Y.; Obuchi, M.; Toyoshima, R.; Kondoh, H.; Oka, K.; Wu, B.; Li, L.; Anzai, A.; Toyao, T.; Shimizu, K. I. Enhanced Nitrous Oxide Decomposition on Zirconium-Supported Rhodium Catalysts by Iridium Augmentation. *Environ. Sci. Technol.* **2025**, *59* (3), 1598–1607.
(40) Chanussot, L.; Das, A.; Goyal, S.; Lavril, T.; Shuaibi, M.; Riviere, M.; Tran, K.; Heras-Domingo, J.; Ho, C.; Hu, W.; Palizhati, A.; Sriram, A.; Wood, B.; Yoon, J.; Parikh, D.; Zitnick, C. L.; Ulissi, Z. Open Catalyst 2020 (OC20) Dataset and Community Challenges. *ACS Catal* **2021**, *11* (10), 6059–6072.
(41) Takahashi, K.; Takahashi, L.; Miyazato, I.; Fujima, J.; Tanaka, Y.; Uno, T.; Satoh, H.; Ohno, K.; Nishida, M.; Hirai, K.; Ohyama, J.; Nguyen, T. N.; Nishimura, S.; Taniike, T. The Rise of Catalyst Informatics: Towards Catalyst Genomics. *ChemCatChem* **2019**, *11* (4).
(42) Kitchin, J. R. Machine Learning in Catalysis. *Nat Catal* **2018**, *1* (4), 230–232.
(43) Fung, V.; Hu, G.; Ganesh, P.; Sumpter, B. G. Machine Learned Features from Density of States for Accurate Adsorption Energy Prediction. *Nat Commun* **2021**, *12* (1), 1–11.
(44) Murdock, R. J.; Kauwe, S. K.; Wang, A. Y. T.; Sparks, T. D. Is Domain Knowledge Necessary for Machine Learning Materials Properties? *Integr Mater Manuf Innov* **2020**, *9* (3), 221–227.
(45) Toyao, T.; Maeno, Z.; Takakusagi, S.; Kamachi, T.; Takigawa, I.; Shimizu, K. I. Machine Learning for Catalysis Informatics: Recent Applications and Prospects. *ACS Catal* **2020**, *10* (3).
(46) Ras, E. J.; Rothenberg, G. Heterogeneous Catalyst Discovery Using 21st Century Tools: A Tutorial. *RSC Adv.* **2014**, *4* (12), 5963–5974.
(47) Calle-Vallejo, F.; Loffreda, D.; Koper, M. T. M.; Sautet, P. Introducing Structural Sensitivity into Adsorption-Energy Scaling Relations by Means of Coordination Numbers. *Nat Chem* **2015**, *7* (5).
(48) Ulissi, Z. W.; Medford, A. J.; Bligaard, T.; Nørskov, J. K. To Address Surface Reaction Network Complexity Using Scaling Relations Machine Learning and DFT Calculations. *Nat Commun* **2017**, *8*.
(49) Li, Z.; Wang, S.; Xin, H. Toward Artificial Intelligence in Catalysis. *Nat Catal* **2018**, *1* (9).
(50) Bruix, A.; Margraf, J. T.; Andersen, M.; Reuter, K. First-Principles-Based Multiscale Modelling of Heterogeneous Catalysis. *Nat Catal* **2019**, *2* (8).
(51) Mou, T.; Pillai, H. S.; Wang, S.; Wan, M.; Han, X.; Schweitzer, N. M.; Che, F.; Xin, H. Bridging the Complexity Gap in Computational Heterogeneous Catalysis with Machine Learning. *Nat Catal* **2023**, *6* (2).

(52) Kalikadien, A. V.; Valsecchi, C.; van Putten, R.; Maes, T.; Muuronen, M.; Dyubankova, N.; Lefort, L.; Pidko, E. A. Probing Machine Learning Models Based on High Throughput Experimentation Data for the Discovery of Asymmetric Hydrogenation Catalysts. *Chem. Sci.* **2024**, *15* (34), 13618–13630.
(53) Mosquera-Lois, I.; Kavanagh, S. R.; Ganose, A. M.; Walsh, A. Machine-Learning Structural Reconstructions for Accelerated Point Defect Calculations. *NPJ Comput Mater* **2024**, *10* (1).
(54) Taniike, T.; Takahashi, K. The Value of Negative Results in Data-Driven Catalysis Research. *Nat Catal* **2023**, *6* (2).
(55) Bae, S.; Lee, H.; Shin, J.; Kim, H. S.; Kim, Y.; Kim, D. H.; Lee, J. M. Data-Driven Inference of Synthesis Guidelines for High-Performance Zeolite-Based Selective Catalytic Reduction Catalysts at Low Temperatures. *Chemistry of Materials* **2022**, *34* (17), 7761–7773.
(56) Madaan, N.; Shiju, N. R.; Rothenberg, G. Predicting the Performance of Oxidation Catalysts Using Descriptor Models. *Catal. Sci. Technol.* **2016**, *6* (1), 125–133.
(57) Erdem Günay, M.; Yıldırım, R. Recent Advances in Knowledge Discovery for Heterogeneous Catalysis Using Machine Learning. *Catal. Rev.* **2021**, *63* (1).
(58) Ramirez, A.; Lam, E.; Gutierrez, D. P.; Hou, Y.; Tribukait, H.; Roch, L. M.; Copéret, C.; Laveille, P. Accelerated Exploration of Heterogeneous CO_2 Hydrogenation Catalysts by Bayesian-Optimized High-Throughput and Automated Experimentation. *Chem Catal.* **2024**, *4* (2).
(59) Mine, S.; Takao, M.; Yamaguchi, T.; Toyao, T.; Maeno, Z.; Hakim Siddiki, S. M. A.; Takakusagi, S.; Shimizu, K. ichi; Takigawa, I. Analysis of Updated Literature Data up to 2019 on the Oxidative Coupling of Methane Using an Extrapolative Machine-Learning Method to Identify Novel Catalysts. *ChemCatChem* **2021**, *13* (16), 3636–3655.
(60) Mine, S.; Jing, Y.; Mukaiyama, T.; Takao, M.; Maeno, Z.; Shimizu, K. I.; Takigawa, I.; Toyao, T. Machine Learning Analysis of Literature Data on the Water Gas Shift Reaction toward Extrapolative Prediction of Novel Catalysts. *Chem Lett* **2022**, *51* (3), 269–273.
(61) Wang, A. Y. T.; Kauwe, S. K.; Murdock, R. J.; Sparks, T. D. Compositionally Restricted Attention-Based Network for Materials Property Predictions. *NPJ Comput Mater* **2021**, *7* (1), 1–10.
(62) Falkowski, A. R.; Kauwe, S. K.; Sparks, T. D. Optimizing Fractional Compositions to Achieve Extraordinary Properties. *Integr Mater Manuf Innov* **2021**, *10* (4), 689–695.
(63) Wang, G.; Mine, S.; Chen, D.; Jing, Y.; Ting, K. W.; Yamaguchi, T.; Takao, M.; Maeno, Z.; Takigawa, I.; Matsushita, K.; Shimizu, K. ichi; Toyao, T. Accelerated Discovery of Multi-Elemental Reverse Water-Gas Shift Catalysts Using Extrapolative Machine Learning Approach. *Nat. Commun.* **2023**, *14* (1), 1–12.
(64) Jing, Y.; Zhang, C.; Shinya, M.; Zhang, X.; He, C.; Zhang, N.; Guo, X.; Anzai, A.; Oka, K.; Toyoshima, R.; Kondoh, H.; Takigawa, I.; Shimizu, K.; Toyao, T. Extrapolative-Machine-Learning-Guided Discovery of Multi-Elemental Heterogeneous Catalysts for Low-Temperature NO Reduction by H_2. *Res Sq* **2025**.
(65) Zhao, S.; Mine, S.; Wang, G.; Zhang, W.; Fakir, A. A. El; Yang, B.; Qin, Z.; Dostagir, N. H. M.; Matsushita, K.; Takigawa, I.; Shimizu, K.; Toyao, T. Development of Highly Active Catalysts for Low-Temperature CO_2 Hydrogenation to Methanol Using Machine Learning Approach. *ChemRxiv* **2025**.
(66) Yamaguchi, S.; Hu, P.; Ya, H.; Xiao, P.; Nakata, A.; Miyazaki, T.; Morikawa, Y.; Kondo, J. N.; Tange, K.; Tonokura, K.; Takemoto, M.; Yonezawa, Y.; Yokoi, T.; Iyoki, K.; Okubo, T.; Wakihara, T. Adsorption Behavior of Low-Concentration Nitrous Oxide on Natural Mordenite Zeolite. *Microporous and Mesoporous Materials* **2025**, *388*.
(67) Yue, B.; Lian, X.; Liu, S.; Wu, G.; Xu, J.; Li, L. Efficient Nitrous Oxide Capture by Cationic Forms of FAU and CHA Zeolites. *Chemical Engineering Journal* **2023**, *462*.

(68) Hiraki, S.; Baba, H.; Kobayashi, I.; Oda, A.; Ohkubo, T.; Ikemoto, Y.; Moriwaki, T.; Kuroda, Y. Excellent Capture of N2O Functioning at RT and Lower Pressure by Utilizing an NaCaA-85 Zeolite. *Chemical Communications* **2024**, *60* (34), 4597–4600.
(69) Meloni, E.; Martino, M.; Pierro, M.; Pullumbi, P.; Brandani, F.; Palma, V. MW-Assisted Regeneration of 13X Zeolites after N2O Adsorption from Concentrated Streams: A Process Intensification. *Energies (Basel)* **2022**, *15* (11).
(70) Saha, D.; Bao, Z. Adsorption of CO_2, CH_4, N_2O, and N_2 on MOF-5, MOF-177, and Zeolite 5A. *Environ. Sci. Technol.* **2010**, *44* (5), 1820–1826.
(71) Tolman, W. B. Binding and Activation of N_2O at Transition-Metal Centers: Recent Mechanistic Insights. *Angew. Chem. Int. Ed.* **2010**, *49* (6), 1018–1024.
(72) Yang, J.; Du, B.; Liu, J.; Krishna, R.; Zhang, F.; Zhou, W.; Wang, Y.; Li, J.; Chen, B. MIL-100Cr with Open Cr Sites for a Record N_2O Capture. *Chem. Commun.* **2018**, *54* (100), 14061–14064.
(73) Wu, T.; Shen, Y.; Feng, L.; Tang, Z.; Zhang, D. Adsorption Properties of N_2O on Zeolite 5A, 13X, Activated Carbon, ZSM-5, and Silica Gel. *J. Chem. Eng. Data* **2019**, *64* (8), 3473–3482.
(74) Yamashita, K.; Liu, Z.; Iyoki, K.; Chen, C. T.; Miyagi, S.; Yanaba, Y.; Yamauchi, Y.; Okubo, T.; Wakihara, T. Synthetic and Natural MOR Zeolites as High-Capacity Adsorbents for the Removal of Nitrous Oxide. *Chem. Commun.* **2021**, *57* (11), 1312–1315.
(75) Kosaka, F.; Liu, Y.; Chen, S. Y.; Mochizuki, T.; Takagi, H.; Urakawa, A.; Kuramoto, K. Enhanced Activity of Integrated CO_2 Capture and Reduction to CH_4 under Pressurized Conditions toward Atmospheric CO_2 Utilization. *ACS Sustain Chem Eng* **2021**, *9* (9), 3452–3463.
(76) Li, L.; Wu, Z.; Miyazaki, S.; Toyao, T.; Maeno, Z.; Shimizu, K. Continuous CO_2 Capture and Methanation over Ni-Ca/Al_2O_3 Dual Functional Materials. *RSC Adv* **2023**, *13* (4), 2213–2219.
(77) Li, L.; Miyazaki, S.; Wu, Z.; Toyao, T.; Selyanchyn, R.; Maeno, Z.; Fujikawa, S.; Shimizu, K. Continuous Direct Air Capture and Methanation Using Combined System of Membrane-Based CO_2 Capture and Ni-Ca Based Dual Functional Materials. *Appl Catal B* **2023**, *339*, 123151.

Chapter 2

Machine learning-assisted development of high-performance catalysts for direct N_2O decomposition

2.1 Introduction

Nitrous oxide (N_2O) is a potent greenhouse gas with a global warming potential that is approximately 300 times greater than that of carbon dioxide (CO_2) on a per-mass basis. In addition to its contribution to climate change, N_2O is a major ozone-depleting substance because it can reach the stratosphere and undergo photolytic decomposition, releasing nitrogen oxides (NO_x) that catalyze ozone breakdown.[1,2] Given a rapid increase in N_2O emissions from agricultural practices, industrial activities, and fossil fuel combustion, controlling its level in the atmosphere has become a pressing environmental priority.[3,4] Therefore, the development of efficient strategies for N_2O abatement is of great significance to both climate protection and ozone layer preservation.

Direct decomposition[5–7] and reduction approaches[8–16] are generally considered the two main catalytic strategies for N_2O emissions. Direct catalytic decomposition is particularly attractive because of its efficiency and the absence of external reducing agents, which lowers the operational costs. Over the past few decades, a wide range of catalysts, including supported noble and metal oxides,[17–20] composite oxides such as perovskites,[21–23] hydrotalcites,[7,24] spinels,[25–28] and zeolite-based catalysts[29–32] have been explored for direct N_2O decomposition. However, these catalysts typically suffer from reduced activity under practical conditions where common inhibitors such as O_2 are present.[26,33–35] This limitation highlights the need for robust catalysts that can maintain a high activity in the presence of O_2, making them viable for practical applications.

Among the catalysts studied, Rh is generally considered one of the most effective for N_2O decomposition, especially in the presence of O_2.[33,36–39] Our previous research has demonstrated that supported RhO_x catalysts are particularly effective at a relatively low temperature (~350 °C), with RhO_x/ZrO_2 containing 5 wt.% Rh identified as one of the best performers.[40] However, Rh-based catalysts still require temperatures above 350 °C to achieve sufficient activity under practical conditions. In addition, the high cost of Rh, which exceeds that of most other platinum-group metals, remains a significant barrier to its widespread application. These limitations underscore the need for the development of more active and cost-effective catalytic systems.

Recent developments in molecular and materials informatics have led to a paradigm shift in molecular and materials science, enabling the rational design of functional molecules and materials.[41–44] Although artificial intelligence (AI) has demonstrated proof-of-concept success

in accelerating catalyst discovery and significantly reducing the associated time and cost, most studies have been limited to benchmark problems, with few cases leading to the discovery of fundamentally new molecules, materials, or synthetic transformations.[45,46] A major challenge is that machine learning (ML) models typically focus on interpolation within known data rather than extrapolation to unknown high-performance candidates. This limitation is particularly pronounced in catalysis informatics, where the underlying reactions involve dynamic and time-dependent phenomena.[42,46,47] Furthermore, compared with materials informatics, catalysis research suffers from a lack of large, high-quality datasets because of the prohibitive computational costs of accurately modeling heterogeneous catalysts.[48–51] High-throughput experimental methods for catalysis that have successfully advanced other scientific fields remain underdeveloped.[52–54] Moreover, the scarcity of negative results in catalytic research poses a significant challenge for data-driven approaches.[55] To overcome these challenges, it is critical to develop ML models that can effectively identify novel catalysts within diverse chemical spaces using experimental catalytic data.[47,53,56–59]

In this context, our group has developed an ML approach that employs elemental features, such as electronegativities and melting points, instead of directly using catalyst composition as input representation.[60,61] Each catalyst is represented as a weighted combination of elemental descriptors based on the proportion of each element.[60,61] This method enables catalyst design and discovery in chemical spaces that have little overlap with the training data and allows for the incorporation of elements that were not included in the original dataset, thereby enabling extrapolative predictions. Other studies have confirmed the effectiveness of this strategy using advanced feature engineering and selection techniques.[62] In addition to this theoretical foundation,[60,61,63] we recently applied this approach to the development of multi-elemental reverse water-gas shift catalysts.[64] The composition of optimal catalyst was Pt/Rb–Ba–Mo–Nb/TiO_2. Notably, Nb was not originally present in the dataset, and the resulting catalyst composition was beyond expectations, even by experts. This success demonstrated the ability of ML-driven catalyst design to overcome the limitations of conventional intuition-based exploration. However, although this approach successfully identified novel high-performance catalysts, it was limited to a single catalytic system, focusing only on the effect of additive oxides while keeping Pt and TiO_2 fixed as the support metal and support, respectively. More recently, we extended our extrapolative ML strategy to develop new multi-elemental catalysts for the selective catalytic reduction of NO_x

using H_2 (H_2-SCR)[65] and low-temperature methanol synthesis from CO_2 and H_2[66]. The optimal catalysts for these reactions were found to be Pt–Ir/Ba–Co/H-ZSM-5 and Pt/Mo–Re–W/TiO_2, respectively. These studies further highlighted the potential of ML for identifying unexpected and highly efficient catalytic systems. There is a strong demand to apply this ML approach to other valuable catalytic reaction processes.

In this study, we developed efficient N_2O decomposition catalysts using this approach. Using 51 catalysts as the initial dataset, we performed 37 cycles of the closed-loop discovery system (ML prediction + experiment) and experimentally tested 633 catalysts. This process led to the identification of more than ten multi-elemental catalysts with superior activity compared to the previously identified best catalyst, with Rh(1)–Pd(2)/ZrO_2_EP emerging as the best catalyst for N_2O decomposition in the presence of O_2, H_2O, and CO_2.

2.2 Experimental details

2.2.1 Chemicals and catalyst preparation

The catalysts in this study can be described by the general formula $PGM_1(X_{P1})$–$PGM_2(X_{P2})$–$PGM_3(X_{P3})$–$PGM_4(X_{P4})$/$Add_1(X_{A1})$–$Add_2(X_{A2})$–$Add_3(X_{A3})$/Support (where PGM = platinum group metal, namely, Pt, Pd, Ru, Rh, Ir, Au, or Re in the present study. Au and Re are included in this category because of their similar chemical properties and high cost; Add_X = additive element; X_{PX} = loading amount of PGM_X, and X_{AX} = loading amount of Add_X). The catalysts were prepared using the sequential impregnation method. Note that elements with atomic numbers (AN) from 3 (Li) to 83 (Bi), except for Be, B, C, N, O, F, Cl, As, Br, Tc, Pm, Hg, Tl, noble gases, and platinum group metals, were used as the catalyst components in this work. First, the additive-loaded support ($Add_1(X_{A1})$–$Add_2(X_{A2})$–$Add_3(X_{A3})$/Support) was prepared via an impregnation process. A mixture of the related amount of support and corresponding sources of the Add elements were added to a 100 mL glass vessel containing an appropriate amount of deionized water and stirred for 30 min with 200 rpm agitation at 50 °C. The mixture was evaporated to dryness at 50 °C, dried at 110 °C for 1 h and calcined in air at 700 °C for 3 h to give $Add_1(X_{A1})$–$Add_2(X_{A2})$–$Add_3(X_{A3})$/Support. The formed additive-loaded support was then added to an aqueous solution containing the PGM precursors. The mixture was stirred for 15 min with 200 rpm agitation at 50 °C, evaporated to dryness at 50 °C and further dried in air at 110 °C for 1 h, then calcined in air at 700 °C for 3 h to obtain $PGM_1(X_{P1})$–$PGM_2(X_{P2})$–$PGM_3(X_{P3})$–$PGM_4(X_{P4})$/$Add_1(X_{A1})$–$Add_2(X_{A2})$–$Add_3(X_{A3})$/Support. Calcination at high

temperature (700 °C) was conducted to ensure the thermal stability of the catalysts. Note that the maximum Rh loading was set to 1 wt.% and the maximum PGM loading was set to 3 wt.%.

2.2.2 Characterization

X-ray diffraction (XRD) patterns were recorded on Rigaku Miniflex software using Cu-Kα radiation from 20° to 70° at 40 kV and 40 mA with a scanning speed of 1° / min. High-angle annular dark-field scanning transmission electron microscopy (HAADF-STEM) and energy-dispersive X-ray (EDX) were performed using a FEI Titan G2 microscope. Samples were prepared by dropping an ethanol solution containing the catalyst on carbon-supported Cu grids.

In situ Rh K-edge and Pd K-edge X-ray absorption spectroscopy (XAS) was performed in the transmittance mode at the BL01B1 beamline with a Si(311) double crystal monochromator (proposal 2023A1931). 40 mg of sample pellets (ϕ 7mm) was placed in a quartz cell connected to a conventional gas-flow system. The catalyst was heated to 280 °C from room temperature with a heating rate of 10 °C/min. After the catalyst was heated to 280 °C, 0.5% N_2O/He was introduced into the cell with a total flow rate of 300 mL/min for 15 min followed by a He purge for 15 min. The space velocity was ~ 30, 000 h^{-1}. The XANES results were analyzed using the Athena software ver. 0.9.25, which is included in the Demeter package.[67]

Ambient Pressure X-ray photoelectron spectroscopy (AP-XPS) measurements were performed at beamline 13B of the Photon Factory (PF) of the High Energy Accelerator Research Organization (KEK). The powder catalysts were coated onto a Si substrate using a drop-and-dry method with ethanol as the dispersant. The sample temperature was measured using a K-type thermocouple attached directly to the sample holder in the analysis chamber. The N_2O gas (99.5%, GL Science Inc.) were introduced into the chamber using variable leak valves. The catalyst was exposed to N_2O at 0.1 Torr, followed by evacuation under vacuum for 30 min at 280 °C for 3 cycles. The binding energy was calibrated by setting the Zr 3d in ZrO_2_EP at 182.8 eV. The Rh 3d and Pd 3d AP-XPS spectra were deconvoluted with Gaussian and Lorentzian functions and a Shirley-type background. The signal intensities in the AP-XPS spectra were normalized to the Zr 3d peak to account for the attenuation caused by the ambient gases.

In situ Diffuse reflectance UV-vis spectroscopy measurements were performed using a UV-vis spectrometer (JASCO V-750) equipped with a commercial *in situ* flow cell. The powdered catalyst (50 mg) was heated (~7 mm diameter) to obtain a smooth surface. $BaSO_4$ was used to collect the background spectra at room temperature. Time-resolved measurements at 798 nm using the Kubelka-Munk function were recorded every 10 s. During the *in situ* UV-vis spectroscopy measurement, 1% N_2O/He was introduced into the cell with a total flow rate of 100 mL/min following the catalyst temperature reaching 280 °C. After reaching steady state, the feed gas was switched from 1% N_2O/He to He.

2.2.3 Catalytic reaction

Catalytic tests were carried out using 20 mg of the catalyst in a fixed-bed flow reactor by feeding a gas mixture containing 0.1% N_2O, 10% O_2, 5% CO_2, 1% H_2O, and He balance, at a flow rate of 100 mL/min. After pretreating the catalyst under a flow of reaction gas at 500 °C for 30 min, the catalyst was cooled to 250 °C and light-off tests (i.e., monitoring catalytic activity during a controlled temperature ramp) were performed at a heating rate of 3 °C/min. The concentration of N_2O in the effluent was monitored using an online IR spectrometer (JASCO FT/IR-4600) equipped with a thermal conductivity detector (TCD) and a homemade gas cell (CaF_2 window).

2.2.4 ML methods

Each catalyst consisted of three components (PGM, Add, and Support). This study aimed to explore and optimize catalysts using ML predictions, requiring the design of catalyst feature representations as inputs to the ML model. Two representations were considered for catalysts composed of mixtures of multiple elements. The first is a conventional approach in which the composition ratios of potential elements are stored and expressed in a one-hot encoding format. The second approach, which we refer to as "element descriptors", abstracts the representation by focusing solely on certain chemical properties rather than specific types of elements. For example, consider a catalyst consisting of m elements, $E_1(X_1), E_2(X_2), \ldots, E_m(X_m)$, where $E_1, \ldots, E_m$ are the elements and $X_1, \ldots, X_m$ are their corresponding contents. If we choose each E_i from the candidate set of n elements, the first representation becomes a numerical vector of length n, where only the components corresponding to each E_i have a nonzero value with X_i. On the other hand, the second representation is defined as the weighted sum of elemental descriptors for E_i scaled by its composition fraction X_i as

$$X_1\ vec(E_1) + X_2 vec(E_2) + \cdots + X_m vec(E_m)$$

where $vec(E_i)$ denotes the elemental descriptor vector for element E_i. This representation is also known as the composition-based feature vector (CBFV).[68]

Based on these two choices, three types of input representations were investigated for each PGM, Add, and Support component: (0) a direct representation, which uses only the first approach; (1) an exploitative representation, which concatenates the first and second approaches; and (2) an explorative representation, which uses only the second approach. The representation choice for a catalyst is denoted as ijk, where $i, j, k \in \{0,1,2\}$, and i, j, and k represent the choice for PGM, Add, and Support, respectively. Thus, code 012 represents a catalyst with representation 0 for PGM, 1 for Add, and 2 for Support. A representative list of the elemental and support descriptors for each component is provided in **Table 2.1**. A detailed list of the descriptors used for each iteration is provided as a separate Excel file on authors' institutional repository (https://aist.repo.nii.ac.jp/records/2003399).

As elemental descriptors for the PGM, we used the following four parameters for the post-analysis of the final dataset: atomic radius, electronegativity according to Pauling (EN(Pauling)), group and adsorption energy (E_{ads}) of an O atom on metallic surfaces calculated using VASP code (version 5.4.4).[69,70] For VASP calculations, the Perdew–Burke–Ernzerhof functional revised for solids (PBEsol)[71] was employed in combination with the projector-augmented wave (PAW) method.[72] A kinetic energy cutoff of 400 eV was used for the plane-wave basis sets. Gaussian smearing with a width of 0.2 eV was applied for electronic level occupation. The Brillouin zone was sampled using 2×2×1 Monkhorst-Pack grids. The van der Waals interactions were described using the dispersion-corrected DFT-D3 (BJ) function.[73] The convergence of the force on each atom was set to 0.03 eV $Å^{-1}$. The most stable and common metallic bulk structures and facets were used for each element.

As elemental descriptors for Add, we selected the following five parameters for the post-analysis of the final dataset: atomic radius, group, enthalpy of formation (ΔH_{fus}), molecular weight in the most stable oxide form (MW_Oxide), molecular weight of the precursor used for catalyst preparation (MW_Precursor).

As support descriptors for Support, we selected the following six parameters for the post-analysis of the final dataset: band gap energy calculated using VASP and the PBEsol functional (BG_PBEsol), surface energy (E_{surf}), adsorption energy (E_{ads}) of an N_2O molecule on support surfaces calculated using Matlantis,[74] specific surface area without calcination

(SSA_w/o cal), peak intensities around 1550–1540 cm^{-1} (IR B-acid intensity) observed during pyridine adsorption IR measurements performed at 200 °C (corresponding to Brønsted acid sites) and wavenumber values around ~1460–1440 cm^{-1} (IR L-acid cm^{-1}) observed during pyridine adsorption IR measurements performed at 200 °C (corresponding to Lewis acid sites).

Table 2.1 Descriptors used in ML-based catalyst exploration and statistical analysis of this study[a].

Type	Descriptors
PGM	Electronegativity (EN(Pauling))
	Atomic radius
	Group
	Adsorption energy of an O atom on metallic surfaces (E_{ads}(O))
Add	Atomic radius
	Group
	Enthalpy of formation (ΔH_{fus})
	Molecular weight in the most stable oxide form (MW_Oxide)
	Molecular weight of the precursor used for catalyst preparation (MW_Precursor)
Support	Band gap energy ($E_{\text{Band Gap}}$)
	Surface energy (E_{surf})
	Adsorption energy of an N_2O molecule on support surfaces ($E_{ads}(N_2O)$)
	Specific Surface Area without calcination (SSA_w/o cal)
	Peak intensities around 1550–1540 cm^{-1}, corresponding to Brønsted acid sites, observed during pyridine adsorption IR measurements (IR B-acid intensity)
	Wavenumber values around ~1460–1440 cm^{-1}, corresponding to Lewis acid sites, observed during pyridine adsorption IR measurements (IR L-acid cm^{-1})

[a] Descriptors for PGM, Add and Support shown in this table were used in the post-analysis of the final dataset consisting of 633 points.

The direct input representation (code number = 0) generates 7-dimensional, 56-dimensional, and 17-dimensional feature vectors because the numbers of elements considered as PGM and Add in this study were 7 and 56, respectively, with the exploration of 17 supports. Therefore, this representation tends to be very sparse and statistically uninformative, particularly for Add, when the training dataset is not large but contains a large number of elements and supports. Moreover, it is incapable of handling elements that are absent or statistically infrequent in the training data. On the other hand, the explorative representation (code number = 2) has the same dimensions as the user-specified elemental descriptor, which often produces statistically much more stable results for small-data problems and is not explicitly constrained by the elements included in the training dataset. Technically, this representation is regarded as feature generation by applying global average

pooling to a set of descriptors for individually contained elements through weighted sum pooling, which is a permutation-invariant operation, with its composition fraction as the weight.

Notably, the explorative representation (code number = 2) represents catalysts only in terms of their physicochemical properties via certain descriptors without directly specifying the individual contributions of distinct elements. This abstracted representation enables a more extrapolative and ambitious exploration, focusing only on the physicochemical property space defined by the user, regardless of whether an element is used in the training data.[75] However, because this representation is irreversible, the corresponding catalyst composition cannot be determined directly even if an optimal value is obtained in the physicochemical property space. In our previous study,[60] we developed a procedure to estimate the potential catalyst composition from elemental property representations. In the present study, we employed a more direct "grid search" approach, systematically testing all combinations of possible values for the loading amounts of individual elements within a predefined discrete grid, ensuring that the original catalyst composition is obtained.

2.2.5 ML methods

The overall pipeline of our ML-based catalyst exploration was based on the sequential model-based optimization developed by us.[75–77] Considering the stabilities and efficiencies attained previously using Extra-Trees regression (ETR)[60] in Scikit-learn (version 1.2.2)[78] as the base ML model, and the expected improvement (EI)[79] score as the guiding acquisition criterion, these methods were applied herein.

First, 51 data points were constructed from the above-described catalytic experiments for the initial seeds and labeled as "iteration" = 0. The catalyst compositions in this initial dataset of 51 points were manually determined by the authors without the use of ML. Next, we selected a batch of catalyst candidates for the next experiment by identifying those with high EI values, as predicted by the base ML model trained on the initial dataset (51 data points) using a grid search. The selected catalysts were then synthesized via the sequential impregnation method and employed in the N_2O decomposition reaction to obtain the T_{20} value (the temperature for 20% N_2O conversion during a light-off experiment) as the ML prediction target, and the dataset was updated by adding the obtained dataset to close the loop. Subsequently, the base ML model was retrained using the updated dataset, and the next batch of catalyst candidates was selected for the subsequent experiment. This procedure of candidate selection and experimentation was continued until 37 loops were performed to test

a total of 633 catalysts. For the first ten iterations of the initial exploration, we used the ETR (with n_estimators =100, keeping the other hyperparameters at scikit-learn defaults) of 222 representations using only the explorative representation (code number = 2) for PGM, Add, and Support, with the intention of allocating resources to probe new candidates. From the 11th iteration onward, we used the results up to the t-th iteration ($t \geq 11$) to evaluate the prediction accuracy through 5-fold cross-validation for all combinations of catalyst representation patterns ijk from 000 to 222, totaling 27 patterns, and hyperparameter settings (n_estimators in [100, 500, 1000, 1500], and bootstrap in [True, False]) employing a grid search. The ETR model with the highest accuracy was then employed to conduct the $(t+1)$-th exploration together with 222 and 111 representations, and this cycle was repeated.

A notable feature of our approach is that we implemented human-in-the-loop exploration involving expert judgment when selecting multiple catalyst candidates (the batch) at each iteration. When selecting catalysts for experiments, it is often necessary to consider multiple objectives and ambiguous criteria such as novelty, diversity, cost, availability, and safety.[80] This renders it extremely challenging to reduce these considerations to a single formulaic metric. To address this, we adopted an approach in which the ML system generated a list of the top 100 promising candidates for each representation, and experts then selected those that would proceed to the experimental stage. Because no candidates outside the ML-suggested catalysts were considered, narrowing down the options to this extent makes human selection practical, given the infeasibility of testing all suggested candidates in actual experiments. Even if some degree of bias was introduced despite candidates with high EI values being prioritized, any selected candidates were safeguarded by systematic exploration and ensured to be the top candidates suggested by ML. A list of 100 top-ranking candidates for each representation explored at each iteration was obtained after clustering with K = 100 for candidates with the highest EI values. It should also be noted that in the current study, the ML target T_{20} is a value where lower values correspond to higher activity. Therefore, the ML code was designed such that catalyst systems expected to show lower T_{20} values result in higher EI values (for details, please refer to the ML code available in our repository: https://aist.repo.nii.ac.jp/records/2003399).

2.3 Results and discussion

2.3.1 ML-assisted discovery of catalysts for N_2O decomposition

We explored up to four types of PGM elements, up to three types of additive elements, and one type of support for $PGM_1(X_{P1})$–$PGM_2(X_{P2})$–$PGM_3(X_{P3})$–$PGM_4(X_{P4})$/$Add_1(X_{A1})$–$Add_2(X_{A2})$–$Add_3(X_{A3})$/Support N_2O decomposition catalysts. Each PGM and added element had a unique loading amount (X) for each catalyst. The numbers of PGM elements, additive elements, and supports explored were 7, 56, and 17, respectively. Thus, even with only three and five distinct values assumed for the loading amounts of PGM and additive elements, respectively, the total number of catalyst candidates exceeded 10^{11}. The catalyst composition grid for exploration consisted of ${}_7C_4 \times 3^4 \times {}_{56}C_3 \times 5^3 \times 17 \approx 170$ billion possible combinations. We began by constructing an initial dataset of 51 data points, labeled as “iteration 0”. These catalyst compositions were determined manually by the authors without using ML. Based on this initial dataset, we performed predictions using the base ML model via a grid search employing extra-tree regression (ETR) (see the Methods section for detailed information). We selected a batch of catalyst candidates for the next experiment, considering their expected improvement (EI) values and compositional diversity.[60] The selected catalysts were synthesized via a sequential impregnation method, and evaluated for N_2O decomposition activity. The T_{20} value, which is defined as the temperature required for 20% N_2O conversion during the light-off experiment, was used as the ML prediction target. Note that all the samples were calcined at 700 °C in air to ensure thermal stability, as N_2O decomposition catalysts are expected to require high thermal durability.[37] The performance data from the newly tested catalysts were then added to the dataset to complete one iteration of the closed-loop system. Thus, the ML model was retrained using the updated dataset, and the next batch of promising candidates was selected for synthesis and evaluation. In each subsequent iteration, the EI values were recalculated across all grid points using an ML model trained on all the data obtained up to the previous iteration, and the most promising candidates were suggested to the researchers to perform actual experiments in the next cycle.

Through experimental testing of 633 ML-predicted new catalysts corresponding to 37 cycles of the closed loop discovery system (ML prediction + experimental validation), we found several catalysts that showed higher activity (lower T_{20} value) than the originally identified high-performance catalyst (Rh(1)–Pd(2)/ZrO_2_RC-100) with a T_{20} value of 378 °C, as shown in **Figure 2.1B**. The composition of the best catalyst identified by this approach was Rh(1)–Pd(2)/ZrO_2_EP with a T_{20} of 355 °C. Despite the simple components of our best

catalyst, more than 10 multi-elemental catalysts with superior activity were identified using this approach, including Rh(1)/Sr(0.5)/Al_2O_3_G07 (T_{20} = 363 °C), Rh(1)–Pd(0.5)–Pt(0.5)–Ir(0.7)/Ta(1.6)–W(0.4)/ZrO_2_RC-100 (T_{20} = 369 °C), Rh(1)–Ir(0.7)/Ba(4)–Nd(4)/SnO_2 (T_{20} = 370 °C), and Rh(1)–Pd(0.8)–Pt(1)/Ba(2)/Al_2O_3_G07 (T_{20} = 371 °C). Notably, although many high-performance catalysts contain Rh, our iterative exploration strategy has gradually led to the discovery of effective non-Rh-containing catalysts. Among PGM catalysts, Rh is particularly expensive; therefore, developing catalysts that do not contain Rh is highly important. Initially, the best non-Rh-containing catalyst identified was Ir(1)/ZrO_2_RC-100 with T_{20} of 509 °C. As the iterations progressed, catalysts with improved performance were found, such as Ru(2)–Pd(1)/ZrO_2_EP (T_{20} = 448 °C) at iteration 6, Pd(2)–Ru(1)/MgO (T_{20} = 423 °C) at iteration 13, and Pd(2.6)–Ru(0.2)–Pt(0.2)/Nd(0.5)/Al_2O_3_G07 (T_{20} = 383 °C) at iteration 36. This trend highlights the capability of our ML-guided approach to expand the catalyst design space beyond Rh-based systems and to continuously discover non-Rh-containing catalysts with enhanced performance, even though they have not yet surpassed Rh-based benchmarks. Catalytic reactions using these catalysts were tested at least three times, and the average values were calculated. Notably, these catalysts included elements and supports not included in the initial dataset, as shown in the periodic tables in **Figure 2.2A**. Our approach employs continuous-valued elemental descriptors characterized by user-selected properties such as electronegativity and atomic radius, rather than discrete categorical representations of elements. Each element is represented by a vector of continuous properties, enabling interpolation across the chemical space and extrapolation to elements that were not present in the initial training dataset. This allows the model to consider chemical-feature-based similarities among elements, thereby enhancing the generalization and exploration capacity of the approach. A representative list of the elemental and support descriptors for each component is presented in **Table 2.1**.

Figure 2.1A illustrates the changes in prediction accuracy of the ML models for several representation choices (000, 111, 222, and 121) for each iteration. The prediction accuracy was estimated via a 10-fold cross-validation based on the accumulated data at each iteration. In the actual exploration process, we used 222 for the first ten iterations. Subsequently, 000, 111, 222, and the best model at each iteration were employed according to the estimated prediction accuracies. In the early phase, the model exhibited limited predictive accuracy owing to the small size and high chemical diversity of the dataset. However, as experimental data were accumulated, the prediction accuracy improved, and we began to identify good

catalysts, indicating that the model was becoming better at capturing statistical trends in the available data. This progression reflects the classic exploration–exploitation trade-off in ML, which emphasizes the need to balance between "exploration," that is, probing uncertain regions of chemical space, and "exploitation," capitalizing on accumulated knowledge to refine predictions.[81] Accordingly, descriptor representation 222 was employed during the early phases and after 10 iterations we switched to the best models based on prediction accuracy .

Figure 2.2 display histograms for each (B) Add, (C) PGM, and (D) Support component, respectively, categorized by their N_2O decomposition activity (T_{20} value). Among the Add elements, Si, Sr, and Al appeared most frequently, and catalysts containing these elements exhibited relatively high activities. Additionally, although Se, Sn, Ga, and Hf appeared less frequently, they were associated with a high proportion of highly active catalysts. For the PGM elements, Rh and Pd were the most frequent and were also linked to a relatively high ratio of highly active catalysts compared to that of Au, Re. Among the supports, Al_2O_3_G07 appeared most frequently and was associated with a high proportion of highly active catalysts. Although the optimal catalyst component, Rh(1)–Pd(2)/ZrO_2_EP, is very simple, this approach still identified several additive elements and supports that are effective for multi-elemental N_2O decomposition catalysts.

The light-off curves for N_2O decomposition over Rh(1)–Pd(2)/ZrO_2_EP, along with those of the compared catalysts, are presented in **Figure 2.3**. Rh(1)–Pd(2)/ZrO_2_EP shows the lowest T_{20} of 355 °C, whereas Rh(1)/ZrO_2_EP, Pd(2)/ZrO_2_EP and Rh(1)–Pd(2)/ZrO_2_RC-100 exhibit higher T_{20} values of 415 °C, 448 °C and 378 °C, respectively. These results indicate that the combination of Rh, Pd, and ZrO_2_EP supports is essential for achieving high catalytic activity of Rh(1)–Pd(2)/ZrO_2_EP.

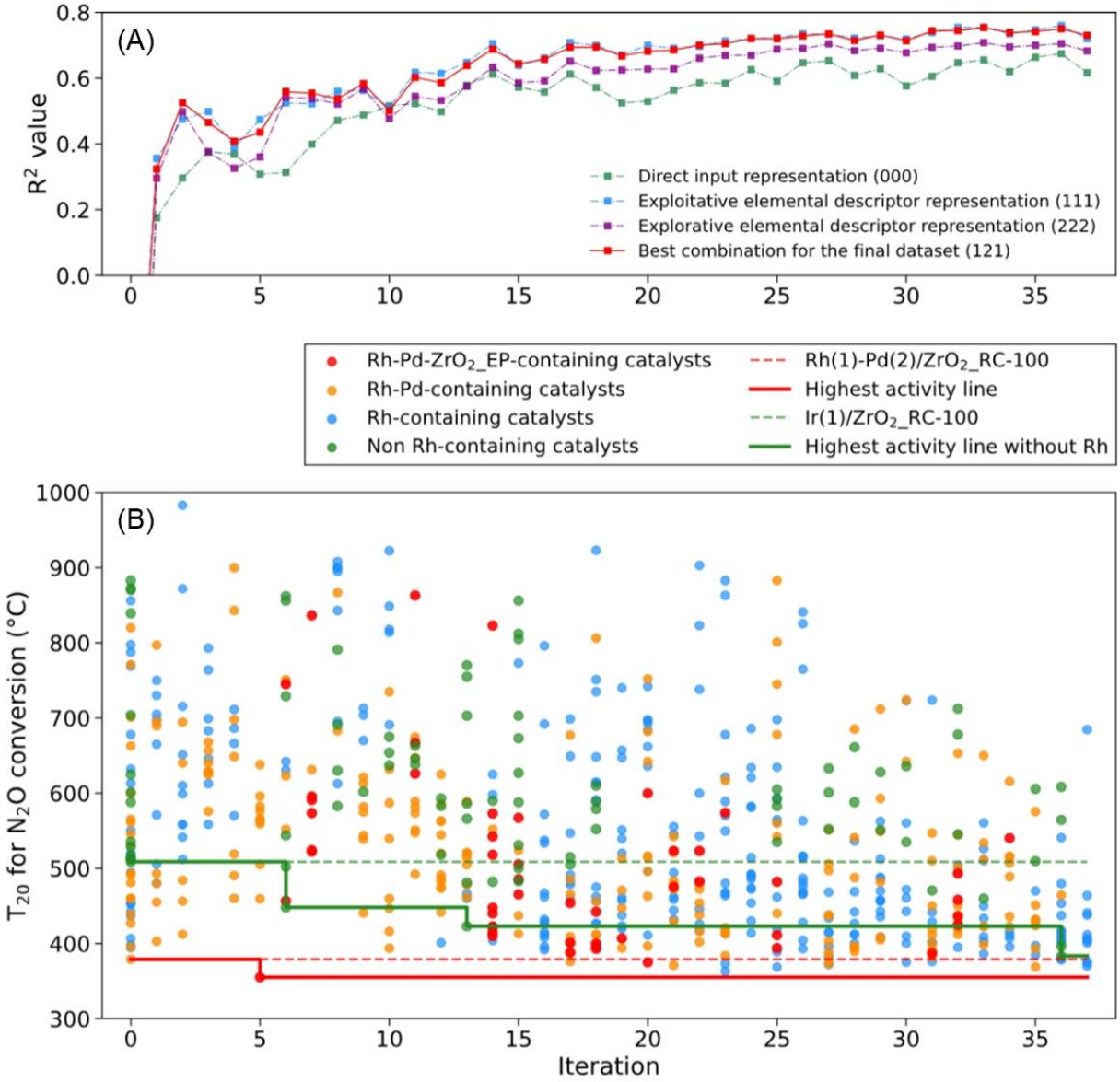

Figure 2.1 (A) Prediction accuracies (R^2 values) evaluated via 10-fold cross-validation (CV), as described in the ML Methods section, using the dataset obtained prior to experimental validation at each iteration. The three numbers in each representation label represent the descriptor representations for PGM, Add, and Support, from left to right. 0 represents a direct input representation using only elemental compositions or support names, 1 represents an exploitative representation incorporating both elemental composition/support name and associated properties, and 2 represents an explorative representation using only elemental/support properties. (B) ML-assisted exploration of the catalysts for N_2O decomposition. Catalysts containing different elements or supports are shown as circles in distinct colors. The solid red line represents the best N_2O decomposition performance (lowest T_{20}) achieved at each iteration, while the dashed red line indicates the best performance in the initial dataset. Similarly, the solid green line represents the best performance for non-Rh catalysts at each iteration, and the dashed green line indicates the best performance for non-Rh catalysts in the initial dataset.

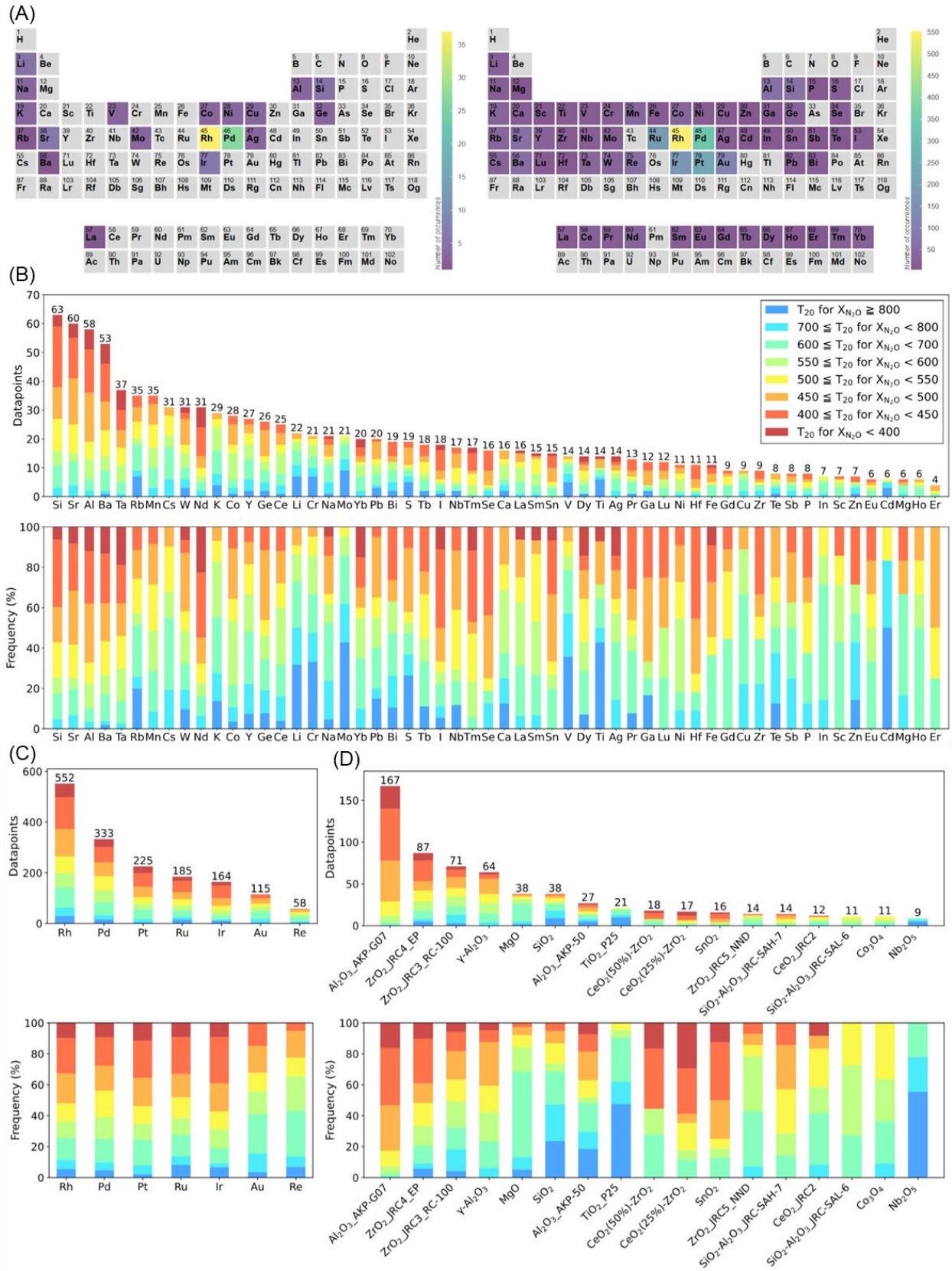

Figure 2.2 (A) Elements used for PGM and Add in the original (left) and final (right) datasets are shown in the periodic table. Histograms for each (B) Add, (C) PGM, and (D) support component categorized by the N_2O decomposition activity (T_{20}). The maximum values on the Y axis for the upper figures represent the sum of the number of data points while that for the bottom figures represent percentage of the N_2O decomposition activity category.

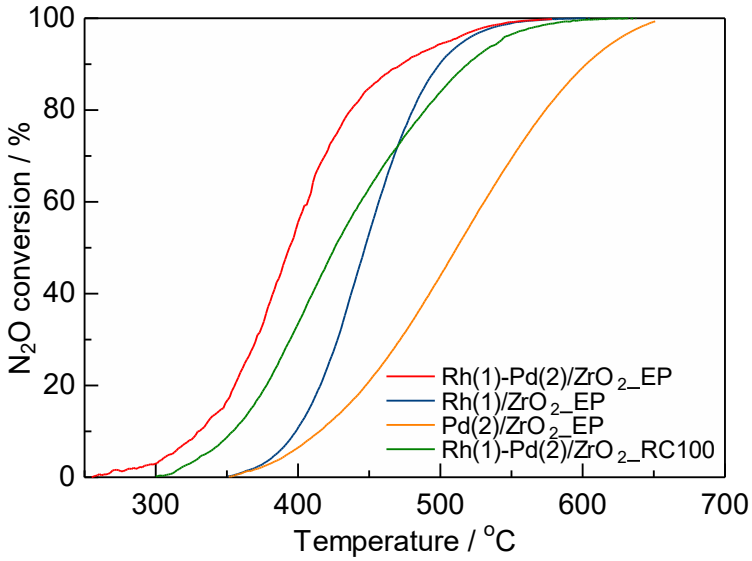

Figure 2.3 Catalytic conversion of N_2O for the light-off test for Rh(1)–Pd(2)/ZrO_2_EP, Rh(1)/ZrO_2_EP, Pd(2)/ZrO_2_EP and Rh(1)–Pd(2)/ZrO_2_RC100 with a heating rate of 3 °C/min under a gas mixture containing 0.1% N_2O, 10% O_2, 1% H_2O, and 5% CO_2 with He balance. Conditions: weight of catalyst: 20 mg, total flow rate: 100 mL/min.

2.3.2 ML-based statistical analysis

Although multi-element catalysts have been discovered through ML-assisted research in other reactions, such as Pt/Ba–Rb–Mo–Nb/TiO_2 for the reverse water–gas shift (RWGS) reaction,[64] Pt–Ir/Ba–Co/H-ZSM-5 for the selective catalytic reduction of NO_x with hydrogen (H_2-SCR),[65] and Pt/Mo–Re–W/TiO_2 for low-temperature methanol synthesis from CO_2 and H_2,[66] the most active catalyst identified for N_2O decomposition in this study was a relatively simple system composed of only two elements and a support. Although the simplicity of this catalyst might appear boring at first glance, clarifying which types of reactions that benefit from multi-element catalyst systems and which do not is an important challenge in the field of catalysis. This highlights the need for detailed mechanistic studies and a deeper understanding of each reaction as well as a comprehensive understanding of different reaction systems.

While ML is frequently used as a black box, supervised ML models can uncover important chemical insights influencing the prediction, even without any explicit knowledge of its underlying principles. Extrapolative ML can reveal not only effective catalyst composition, but also the necessary elemental features and electronic properties for precise catalyst design. SHapley Additive exPlanation (SHAP) analyses were used to understand the importance of descriptors for ML prediction, as shown in **Figure 2.4A**. Al_2O_3_AKP-G07, Rh, and TiO_2_P25 were the most important descriptors. For the element/support descriptors, the

atomic radius, molecular weight of the most stable oxide form (MW_Oxide), and molecular weight of the metal precursor (MW_Precursor) for the Add elements were identified as the most important factors for predicting T_{20}. This was confirmed by the feature-importance scores of the descriptors (**Figure 2.4B**). SHAP can be used to visualize the dependence of the model output (e.g., T_{20}) on the value of each descriptor. For instance, relatively high feature values (red color) for "Rh" and "Al_2O_3_AKP-G07" are correlated to a low T_{20} (SHAP value), indicating that these two descriptors give positive impacts to obtain good activity. On the other hand, a high feature value for "TiO_2_P25" correlates to a high T_{20}, indicating that TiO_2_P25 has a negative impact on the activity.

The SHAP values were analyzed using waterfall plots for the best catalyst, Rh(1)–Pd(2)/ZrO_2_EP, as shown in **Figure 2.4C**. The waterfall plot analysis highlights the descriptors responsible for deviations from the dataset's average value (T_{20} = 538.12 °C) relative to the predicted value for each catalyst. Although the absence of Al_2O_3_AKP-G07 negatively contributes to the T_{20} (low catalytic activity), the presence of Rh and several properties of the support positively contribute to the high activity of our best catalyst. It is well-known that Rh is an effective active metal for direct N_2O decomposition reactions in the presence of O_2.[33,36–39] The results of this ML-based statistical analysis demonstrate that, even without domain knowledge of N_2O decomposition catalysts, such information can be extracted from the dataset created in the present study.

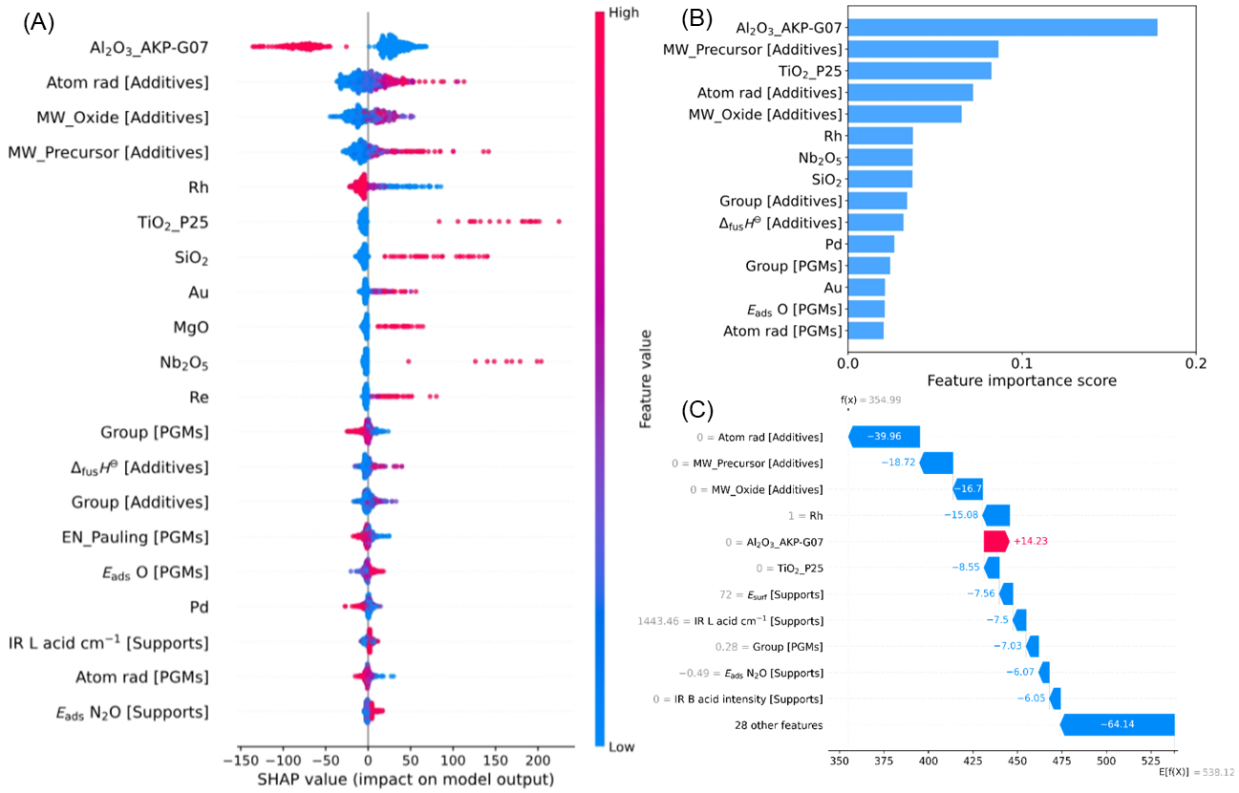

Figure 2.4 (A) SHAP values and (B) feature-importance scores of the descriptors used to predict N_2O decomposition activity (T_{20}). In the SHAP plot, red and blue colors represent high and low feature values, respectively, with corresponding negative and positive contributions to the predicted T_{20} values. Features are ranked by the sum of their absolute SHAP values, indicating their overall contribution to the model. The vertical dispersion of dots reflects the density of data points at corresponding SHAP values. (C) Waterfall plot showing the SHAP value breakdown for the current best catalyst, Rh(1)–Pd(2)/ZrO_2_EP, highlighting how individual features contribute to increasing or decreasing the predicted T_{20} value relative to the model base value. Positive and negative contributions are shown in blue and red, respectively. The model was trained using the best descriptor representation for the final dataset (121).

2.3.3 Catalyst characterization

With the best catalyst composition in hand, structural analyses and mechanistic studies were conducted. This is important because the investigation of extraordinary materials can provide new scientific insights. **Figure 2.5** shows the XRD pattern of Rh(1)–Pd(2)/ZrO_2_EP, which is essentially identical to that of ZrO_2_EP, without the peaks corresponding to Rh oxide or Pd oxide. This suggests that both the RhO_x and PdO_x species are well dispersed in the catalysts. Furthermore, in the XRD pattern of Rh(1)–Pd(2)/ZrO_2_RC-100, which is identified as the original best-performance catalyst in our dataset, the peak attributable to tetragonal ZrO_2 is observed at approximately 2θ = 30°, indicating that the ZrO_2_EP support is monoclinic while the ZrO_2_RC-100 support is a mixture of monoclinic and tetragonal. The HAADF-STEM and EDX mapping images of Rh(1)–Pd(2)/ZrO_2_EP (**Figure 2.6**) demonstrate that the RhO_x particles overlap with the PdO_x particles.

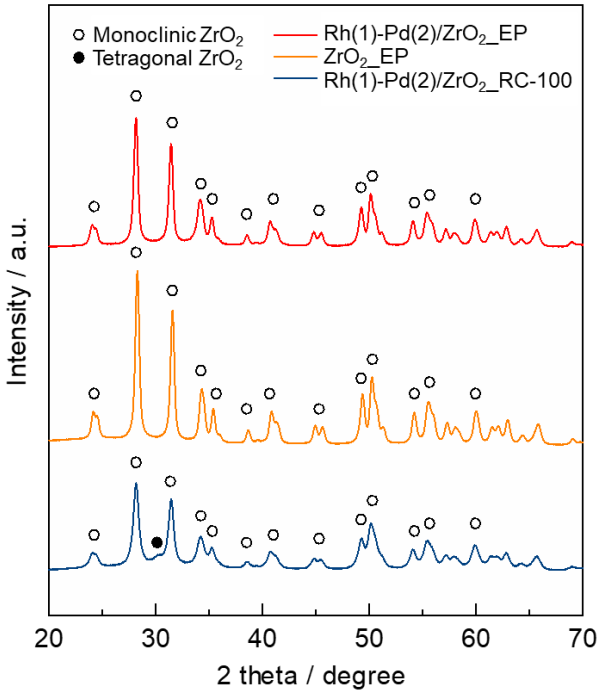

Figure 2.5 XRD patterns of ZrO_2_EP, Rh(1)–Pd(2)/ZrO_2_EP and Rh(1)–Pd(2)/ZrO_2_RC-100.

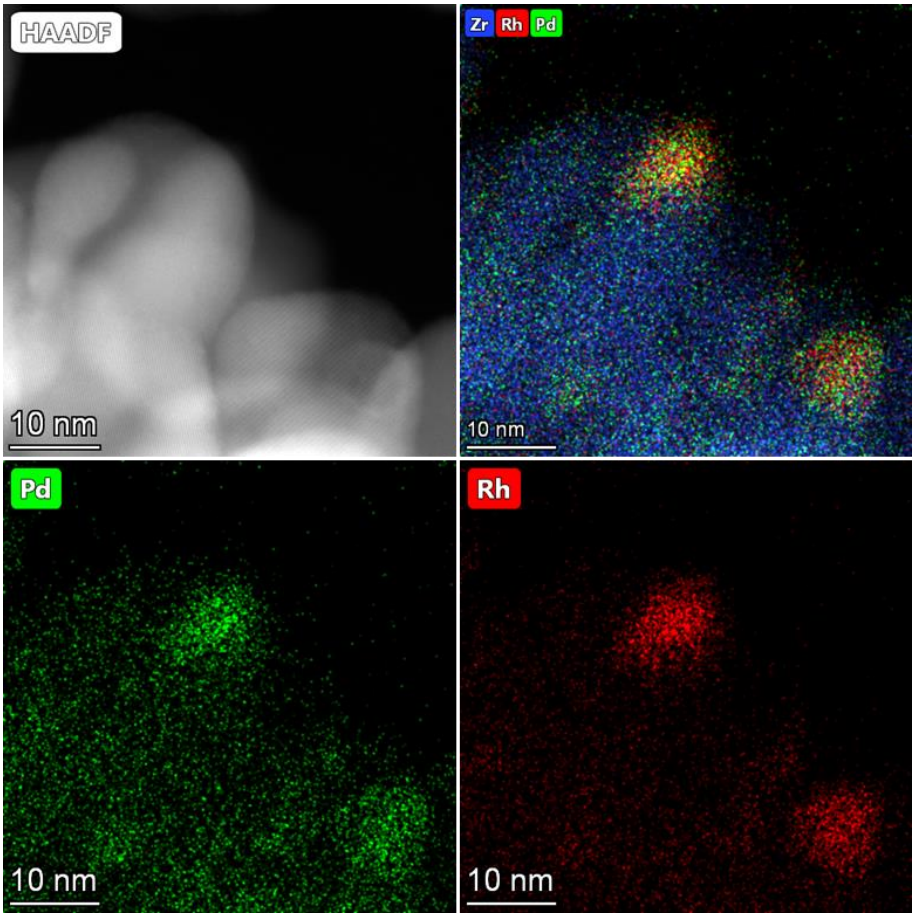

Figure 2.6 HAADF-STEM image and the corresponding EDX mapping images for Rh(1)–Pd(2)/ZrO_2_EP. Note that the sample was calcined at 700 °C in air to ensure thermal stability. See the catalyst preparation section for detailed information.

2.3.4 Mechanistic studies

Kinetic studies were conducted on the current best catalyst (Rh(1)–Pd(2)/ZrO_2_EP). Apparent activation energy (E_a) values calculated from the slopes of the Arrhenius plots are shown in **Figure 2.7**. The apparent activation energy for Rh(1)–Pd(2)/ZrO_2_EP (E_a = 55.0 kJ/mol) is significantly smaller than that of Rh(1)/ZrO_2_EP (E_a = 99.4 kJ/mol). This suggests that the addition of Pd enhances the efficiency of Rh(1)–Pd(2)/ZrO_2_EP for N_2O decomposition compared to Rh(1)/ZrO_2_EP, which is consistent with catalytic activity.

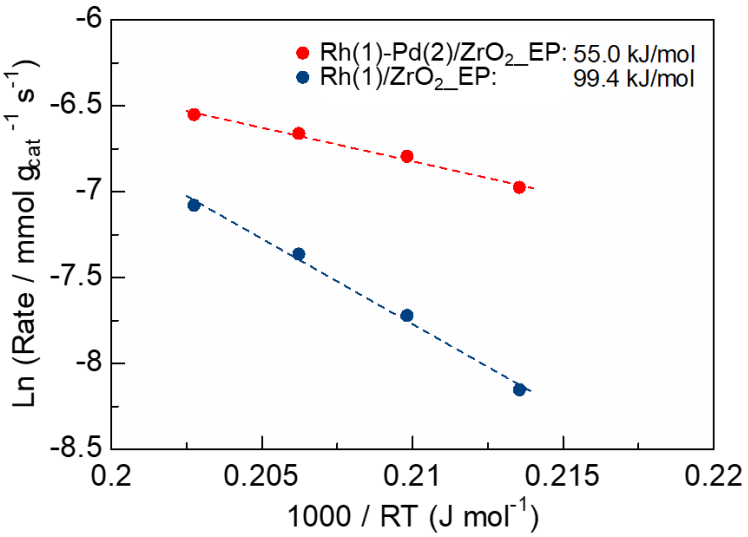

Figure 2.7 Arrhenius plots for the catalytic decomposition of N_2O over Rh(1)–Pd(2)/ZrO_2_EP and Rh(1)/ZrO_2_EP. Quantity of catalyst used, 20 mg; temperature, 200–260 °C; total flow rate, 100 mL/min; N_2O concentration, 0.1% in He.

Figure 2.8 shows *in situ* Rh K-edge and Pd K-edge XANES spectra of Rh(1)–Pd(2)/ZrO_2_EP and the Rh K-edge XANES spectra of Rh(1)/ZrO_2_EP during N_2O decomposition. For Rh(1)–Pd(2)/ZrO_2_EP, the absorption edge of the Rh K-edge XANES spectra shifts to a higher energy after the initial introduction of 0.5% N_2O, indicating that the Rh species is oxidized by N_2O. After subsequent purging under He, the Rh K-edge XANES spectra shift to a lower energy, with the energy at the normalized absorption of 0.4 decreasing from 23229.2 eV to 23228.4 eV. This suggests that N_2O decomposes over the Rh species in Rh(1)–Pd(2)/ZrO_2_EP via a redox cycle. In contrast, the absorption edge of the Pd K-edge XANES spectra showed a noticeable shift during the initial cycles, reflecting active oxidation and reduction of PdO_x. However, as the reaction progressed, the redox activity of PdO_x gradually diminishes, suggesting that PdO_x initially serves as a redox site on its own, but later plays only a supporting role by promoting the redox cycle of RhO_x without directly undergoing redox reactions under steady-state conditions.

For Rh(1)/ZrO_2_EP, negligible changes were observed in the Rh K-edge XANES spectra during the alternation between N_2O and He, with the energy at the normalized absorption (0.4) remaining steady at approximately 23228.8 eV. The absence of detectable changes may result from the limited surface sensitivity of the XAS measurements. XAS generally provides bulk information about the oxidation states of the supported RhO_x and PdO_x species but lacks sensitivity to surface changes. To gain more detailed insights into the surface oxidation state of RhO_x and PdO_x species during N_2O decomposition, we conducted surface-

sensitive ambient pressure X-ray photoelectron spectroscopy (AP-XPS) measurements on Rh(1)–Pd(2)/ZrO_2_EP and Rh(1)/ZrO_2_EP.

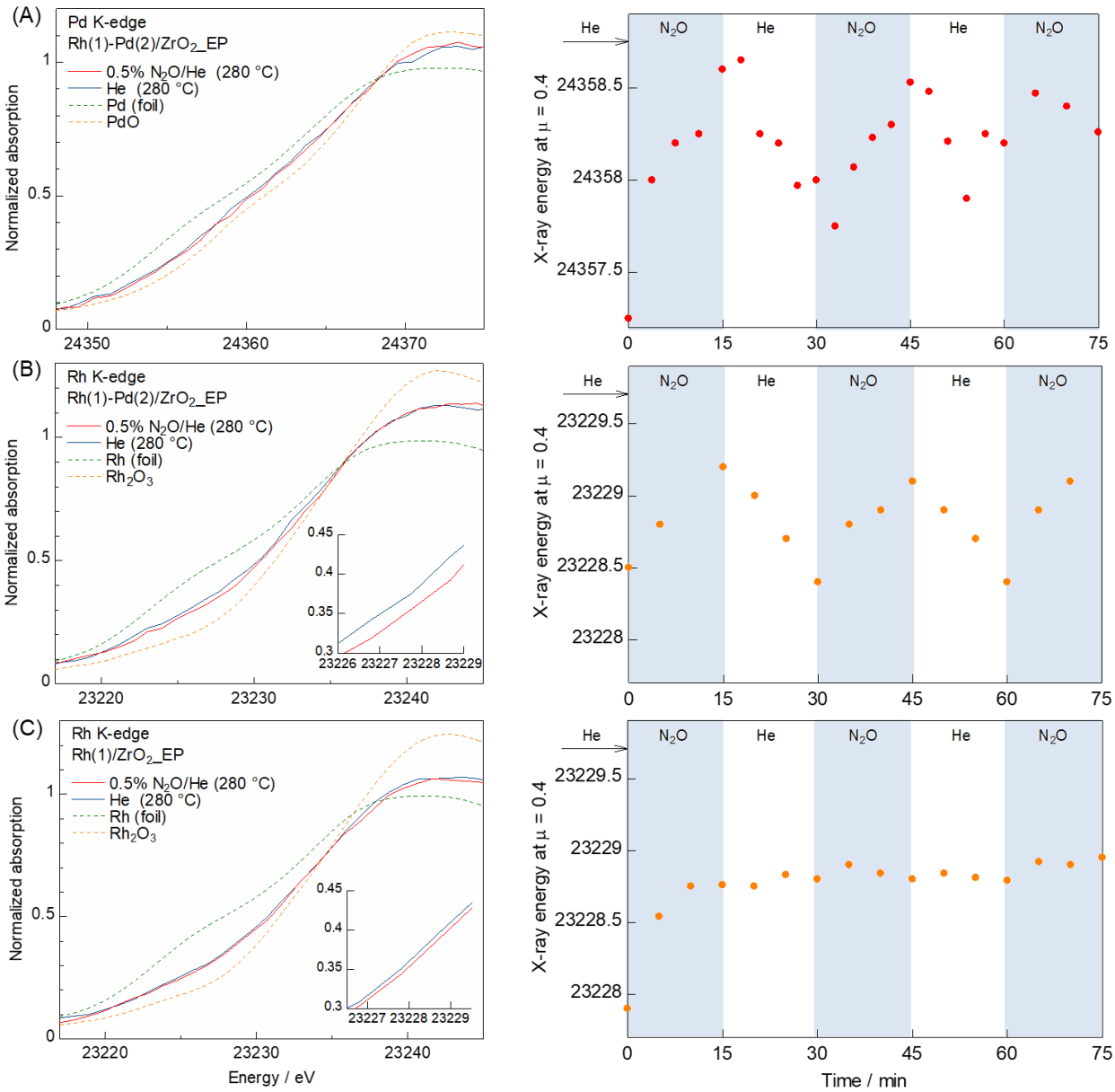

Figure 2.8 *In situ* XANES spectra and the shift in X-ray energy at normalized absorption (0.4): (A) Rh, (B) Pd K-edge for Rh(1)–Pd(2)/ZrO_2_EP and (C) Rh K-edge for Rh(1)/ZrO_2_EP at 280 °C under a flow of 0.5% N_2O/He, with intermittent He purges.

Figure 2.9 shows the AP-XPS spectra of Rh(1)–Pd(2)/ZrO_2_EP and Rh(1)/ZrO_2_EP recorded under various conditions shown in **Figure 2.9A**. The peaks at 307.5, 308.6, and 309.3 eV are assigned to Rh^0 $3d_{5/2}$, Rh^{3+} $3d_{5/2}$, and Rh^{4+} $3d_{5/2}$,[82] respectively, as shown in **Figure 2.9B-D**. The Rh(1)/ZrO_2_EP and Rh(1)–Pd(2)/ZrO_2_EP catalysts were subsequently exposed to various conditions to record their AP-XPS spectra after the temperature was increased to 280 °C. For both Rh(1)/ZrO_2_EP and Rh(1)–Pd(2)/ZrO_2_EP, the intensity of the

Rh^0 peak decreased, and the overall peak intensity of Rh^{4+} increased under exposure to N_2O at 0.1 Torr compared with those under vacuum, indicating that the Rh^0 species were oxidized by N_2O. During the subsequent exposure to vacuum, the Rh^0 peak increased and the peak of Rh^{4+} decreased, demonstrating that the Rh oxide species were thermally reduced to Rh^0 species. Notably, this behavior was reversible during the course of the experiment. This result suggests the N_2O decomposition over the Rh species via a reversible redox process between Rh^0 and Rh^{3+}/Rh^{4+} species for both catalysts. The similar binding energies of Rh^{3+} and Rh^{4+} make reliable deconvolution challenging. Therefore, although the ratio of Rh^{3+} to Rh^{4+} may be inaccurate, this study focused on the relative changes between Rh^0 and the combined oxidized Rh species (Rh^{3+} + Rh^{4+}), rather than attempting to quantify each oxidized state individually. Nonetheless, the redox behavior of Rh upon N_2O introduction is apparent. Rh(1)–Pd(2)/ZrO_2_EP shows a higher fraction of Rh^0 species under vacuum and a higher fraction of oxidized Rh species under exposure to N_2O than that of Rh(1)/ZrO_2_EP (**Figure 2.9E-G**), indicating that the Rh species in Rh(1)–Pd(2)/ZrO_2_EP exhibits higher redox ability than that of Rh(1)/ZrO_2_EP, highlighting the synergistic effect of Pd in enhancing redox dynamics.

The Pd 3d AP-XPS spectra of Rh(1)–Pd(2)/ZrO_2_EP were also obtained using the same experimental procedure as that used for the Rh 3d AP-XPS spectra. As shown in **Figure 2.9C**, the spectra include overlapping signals from the Pd 3d and Zr 3p orbitals originating from the ZrO_2 support. The peaks at 335.1 eV and 336.5 eV are attributed to Pd^0 $3d_{5/2}$ and Pd^{2+} $3d_{5/2}$,[83] while the peaks at 330.7 eV and 332.3 eV are assigned to Zr^{3+} $3p_{3/2}$ and Zr^{4+} $3p_{3/2}$,[84,85] respectively. The fractions of the Zr oxidation states were confirmed using the Zr 3d spectra (not shown), which exhibited slight variations under N_2O-to-vacuum switching. This suggests minor redox behavior on the surface of the Zr species in the ZrO_2 support. **Figure 2.9F** shows the redox behavior of the PdO_x species. However, the redox activity gradually diminished as the reaction proceeded, with the relative amounts of Pd^0 and Pd^{2+} remaining nearly constant throughout the final cycle. These results indicate that PdO_x initially serves as a redox site on its own, but later plays a supporting role by promoting the redox cycle of RhO_x without directly participating in the redox process under steady-state conditions, which is consistent with the results of the *in situ* XANES.

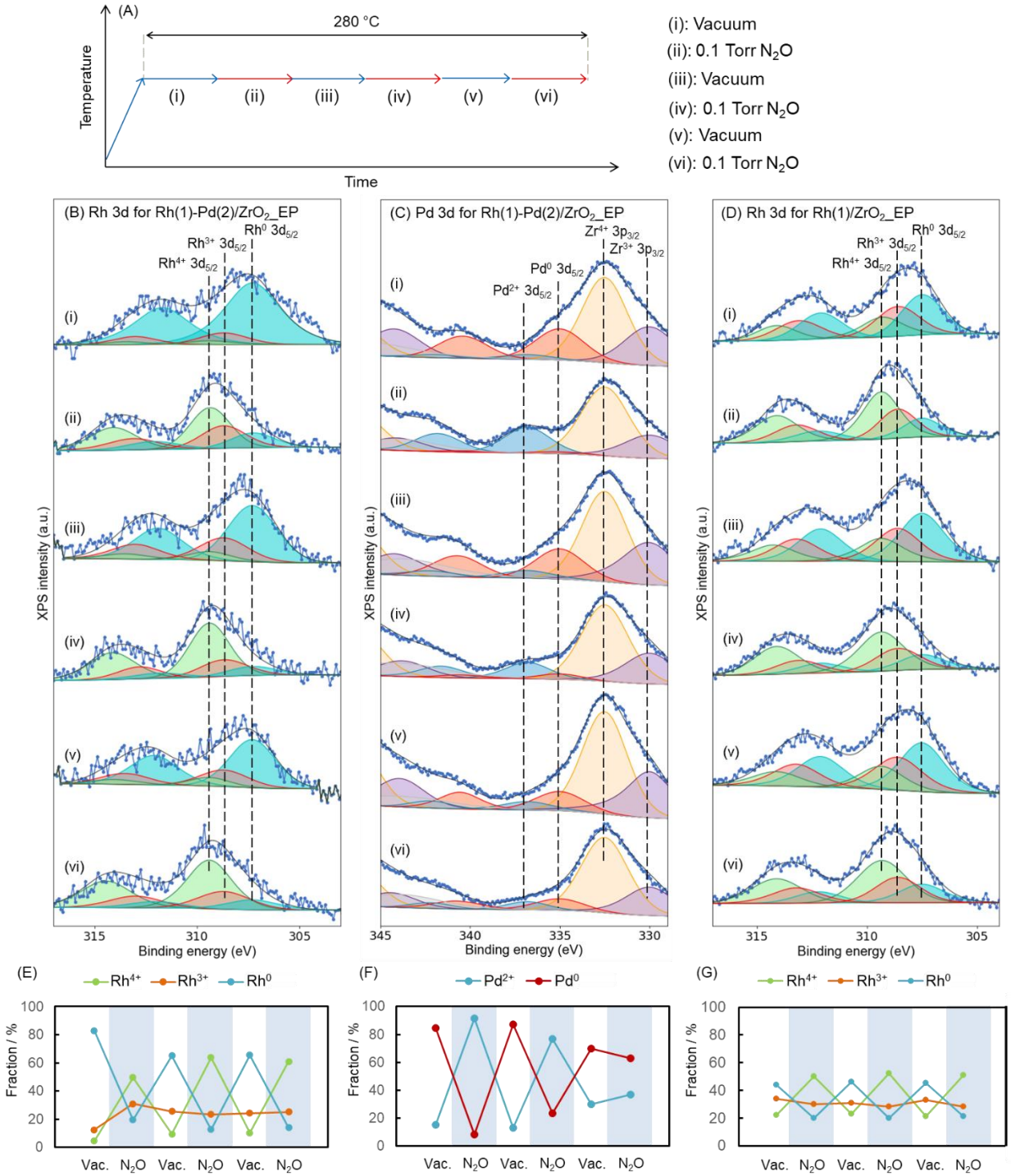

Figure 2.9 (A) Experimental conditions during the AP-XPS study. (B) Rh 3d and (C) Pd 3d AP-XPS spectra of Rh(1)–Pd(2)/ZrO_2_EP and (D) Rh 3d AP-XPS spectra of Rh(1)/ZrO_2_EP under exposure to vacuum, with an interval of 0.1 Torr N_2O at 280 °C. For the Rh 3d spectra: blue dots: raw spectrum; black line: sum; light blue: Rh^0; orange: Rh^{3+}; green: Rh^{4+}. For the Pd 3d AP-XPS spectra: blue dots: raw spectra; black line: sum; red: Pd^0; blue: Pd^{2+}; purple: Zr^{3+} species; yellow: Zr^{4+} species. (E), (F) Fraction of Rh and Pd oxidation states for Rh(1)–Pd(2)/ZrO_2_EP and (G) fraction of Rh oxidation states for Rh(1)/ZrO_2_EP during the redox cycle, respectively.

2.4 Conclusion

Using the ML approach, 633 catalysts were experimentally tested through iterative cycles of ML prediction and validation starting from 51 initial data points. As a result, more than ten catalysts with activity superior to that of the best originally identified catalyst were discovered. Rh(1)–Pd(2)/ZrO_2_EP was the best catalyst for N_2O decomposition in the presence of O_2. In addition to guiding experimental discovery, our ML model provides insights into the important physical and chemical properties governing catalytic performance. Specifically, the model identified both effective catalyst compositions and elemental/support descriptors that correlate with high activity. Experimental mechanistic studies using *in situ* techniques were also performed to elucidate the role of each catalyst component and the reaction mechanism. The obtained results indicated that RhO_x acts as a redox species, whereas PdO_x facilitates the redox reaction of RhO_x under steady-state conditions. Although this study focused on the influence of catalyst composition under fixed preparation and reaction conditions to limit the search space, we acknowledge that preparation methods can significantly impact the catalyst structure and, consequently, performance. Future studies should extend the ML approach to include process variables; however, this will require a substantially larger experimental dataset.

2.5 References

(1) Ravishankara, A. R.; Daniel, J. S.; Portmann, R. W. Nitrous Oxide (N_2O): The Dominant Ozone-Depleting Substance Emitted in the 21st Century. *Science (1979)* **2009**, *326* (5949), 123–125.

(2) Li, L.; Xu, J.; Hu, J.; Han, J. Reducing Nitrous Oxide Emissions to Mitigate Climate Change and Protect the Ozone Layer. *Environ. Sci. Technol.* **2014**, *48* (9), 5290–5297.

(3) Pérez-Ramírez, J.; Kapteijn, F.; Schöffel, K.; Moulijn, J. A. Formation and Control of N_2O in Nitric Acid Production: Where Do We Stand Today? *Appl. Catal., B* **2003**, *44* (2), 117–151.

(4) Konsolakis, M. Recent Advances on Nitrous Oxide (N_2O) Decomposition over Non-Noble-Metal Oxide Catalysts: Catalytic Performance, Mechanistic Considerations, and Surface Chemistry Aspects. *ACS Catal.* **2015**, *5* (11), 6397–6421.

(5) Kapteijn, F.; Rodriguez-Mirasol, J.; Moulijn, J. A. Heterogeneous Catalytic Decomposition of Nitrous Oxide. *Appl. Catal., B* **1996**, *9* (1–4), 25–64.

(6) Jabłońska, M.; Palkovits, R. Nitrogen Oxide Removal over Hydrotalcite-Derived Mixed Metal Oxides. *Catal. Sci. Technol.* **2016**, *6* (1), 49–72.

(7) Jablońska, M.; Arán, M. A.; Beale, A. M.; Delahay, G.; Petitto, C.; Nocuń, M.; Palkovits, R. Understanding the Origins of N_2O Decomposition Activity in Mn(Fe)CoAlO Hydrotalcite Derived Mixed Metal Oxides. *Appl. Catal., B* **2019**, *243*, 66–75.

(8) Beale, A. M.; Gao, F.; Lezcano-Gonzalez, I.; Peden, C. H. F.; Szanyi, J. Recent Advances in Automotive Catalysis for NOx Emission Control by Small-Pore Microporous Materials. *Chem. Soc. Rev.* **2015**, *44* (20), 7371–7405.

(9) Lee, E.; Lee, J.; Park, D. C.; Moon, S.; Song, I.; Jung, H.; Kim, D. H. Pd Nanoparticles Fixed in Zeolites Promote Low-Temperature NO Reduction via Hydrogen Spillover. *Appl. Catal., B* **2025**, *366*, 125060.

(10) Lin, B.; Guo, Z.; Tang, J.; Chen, P.; Ye, D.; Hu, Y. Modulating the Microstructure and Surface Acidity of MnO_2 by Doping-Induced Phase Transition for Simultaneous Removal of Toluene and NO_x at Low Temperature. *Environ. Sci. Technol.* **2024**, *58* (23), 10398–10408.

(11) Xiong, T.; Xiao, G.; Lin, B.; Li, Q.; Fu, M.; Hu, Y. V_2O_5 Modified Mn/SAPO-34 Catalyst for the Synchronous Elimination of NO_x and Volatile Organic Compounds. *Catal. Today* **2024**, *430*, 114535.

(12) Shi, Z.; Sun, H.; Wang, L.; Deng, Q.; Gong, C. X.; Han, L.; Li, K.; Deng, W.; Zhu, Y. A.; Li, Z.; Chen, H.; Zhu, K. Generating Silicon-Rich AFX Zeolite Using Rigid Diquaternary Alkylammonium Structure Directing Agent towards Stable Selective Catalytic Reduction of NO_x by NH_3. *Appl. Catal., B* **2024**, *344*, 123637.

(13) Han, F.; Sun, H.; Zhao, Z.; Xu, Y.; Dong, H.; Liu, W.; Sun, L.; Wang, Z.; Hou, G.; Kitano, M.; Li, W.; Shen, M.; Chen, H. Selective Catalytic Reduction of NO_x by Methanol on Metal-Free Zeolite with Brønsted and Lewis Acid Pair. *ACS Catal.* **2022**, *12* (4), 2403–2414.

(14) Shibata, J.; Hashimoto, M.; Shimizu, K. I.; Yoshida, H.; Hattori, T.; Satsuma, A. Factors Controlling Activity and Selectivity for SCR of NO by Hydrogen over Supported Platinum Catalysts. *J. Phys. Chem. B* **2004**, *108* (47), 18327–18335.

(15) Buttignol, F.; Garbujo, A.; Biasi, P.; Kröcher, O.; Ferri, D. N_2O Activation and NO Adsorption Control the Simultaneous Conversion of N_2O and NO Using NH_3 over Fe-ZSM-5. *J. Am. Chem. Soc.* **2025**, *147* (10), 8978.

(16) Buttignol, F.; Fischer, J. W. A.; Clark, A. H.; Elsener, M.; Garbujo, A.; Biasi, P.; Czekaj, I.; Nachtegaal, M.; Jeschke, G.; Kröcher, O.; Ferri, D. Iron-Catalysed Cooperative Redox Mechanism for the Simultaneous Conversion of Nitrous Oxide and Nitric Oxide. *Nat. Catal.* **2024**, *7* (3), 1305.

(17) Oi, J.; Obuchi, A.; Bamwenda, G. R.; Ogata, A.; Yagita, H.; Kushiyama, S.; Mizuno, K. Decomposition of Nitrous Oxide over Supported Rhodium Catalysts and Dependency on Feed Gas Composition. *Appl. Catal., B* **1997**, *12*, 277–286.
(18) Hinokuma, S.; Iwasa, T.; Kon, Y.; Taketsugu, T.; Sato, K. N_2O Decomposition Properties of Ru Catalysts Supported on Various Oxide Materials and SnO_2. *Sci. Rep.* **2020**, *10* (1), 21605.
(19) Hinokuma, S.; Iwasa, T.; Kon, Y.; Taketsugu, T.; Sato, K. Effects of Support Materials and Ir Loading on Catalytic N_2O Decomposition Properties. *Catal. Commun.* **2021**, *149*, 106208.
(20) Kaczmarczyk, J.; Zasada, F.; Janas, J.; Indyka, P.; Piskorz, W.; Kotarba, A.; Sojka, Z. Thermodynamic Stability, Redox Properties, and Reactivity of Mn_3O_4, Fe_3O_4, and Co_3O_4 Model Catalysts for N_2O Decomposition: Resolving the Origins of Steady Turnover. *ACS Catal.* **2016**, *6* (2), 1235–1246.
(21) Peña, M. A.; Fierro, J. L. G. Chemical Structures and Performance of Perovskite Oxides. *Chem Rev* **2001**, *101* (7), 1981–2017.
(22) Richards, N.; Carter, J. H.; Parker, L. A.; Pattisson, S.; Hewes, D. G.; Morgan, D. J.; Davies, T. E.; Dummer, N. F.; Golunski, S.; Hutchings, G. J. Lowering the Operating Temperature of Perovskite Catalysts for N_2O Decomposition through Control of Preparation Methods. *ACS Catal.* **2020**, *10* (10), 5430–5442.
(23) Simböck, J.; Ghiasi, M.; Schönebaum, S.; Simon, U.; de Groot, F. M. F.; Palkovits, R. Electronic Parameters in Cobalt-Based Perovskite-Type Oxides as Descriptors for Chemocatalytic Reactions. *Nat Commun* **2020**, *11* (1), 1–10.
(24) Armor, J. N.; Braymer, T. A.; Farris, T. S.; Li, Y.; Petrocelli, F. P.; Weist, E. L.; Kannan, S.; Swamy, C. S. Calcined Hydrotalcites for the Catalytic Decomposition of N_2O in Simulated Process Streams. *Appl. Catal., B* **1996**, *7* (3–4), 397–406.
(25) Russo, N.; Fino, D.; Saracco, G.; Specchia, V. N_2O Catalytic Decomposition over Various Spinel-Type Oxides. *Catal. Today* **2007**, *119* (1–4), 228–232.
(26) Asano, K.; Ohnishi, C.; Iwamoto, S.; Shioya, Y.; Inoue, M. Potassium-Doped Co_3O_4 Catalyst for Direct Decomposition of N_2O. *Appl. Catal., B* **2008**, *78* (3–4), 242–249.
(27) Stelmachowski, P.; Maniak, G.; Kotarba, A.; Sojka, Z. Strong Electronic Promotion of Co_3O_4 towards N_2O Decomposition by Surface Alkali Dopants. *Catal. Commun.* **2009**, *10* (7), 1062–1065.
(28) Grzybek, G.; Stelmachowski, P.; Gudyka, S.; Indyka, P.; Sojka, Z.; Guillén-Hurtado, N.; Rico-Pérez, V.; Bueno-López, A.; Kotarba, A. Strong Dispersion Effect of Cobalt Spinel Active Phase Spread over Ceria for Catalytic N_2O Decomposition: The Role of the Interface Periphery. *Appl. Catal., B* **2016**, *180*, 622–629.
(29) Lin, F.; Andana, T.; Wu, Y.; Szanyi, J.; Wang, Y.; Gao, F. Catalytic Site Requirements for N_2O Decomposition on Cu-, Co-, and Fe-SSZ-13 Zeolites. *J. Catal.* **2021**, *401*, 70–80.
(30) Bols, M. L.; Snyder, B. E. R.; Rhoda, H. M.; Cnudde, P.; Fayad, G.; Schoonheydt, R. A.; Van Speybroeck, V.; Solomon, E. I.; Sels, B. F. Coordination and Activation of Nitrous Oxide by Iron Zeolites. *Nat. Catal.* **2021**, *4* (4), 332–340.
(31) Kondratenko, E. V.; Pérez-Ramírez, J. Mechanism and Kinetics of Direct N_2O Decomposition over Fe-MFI Zeolites with Different Iron Speciation from Temporal Analysis of Products. *J. Phys. Chem. B* **2006**, *110* (45), 22586–22595.
(32) Pérez-Ramírez, J.; Hevia, M. A. G.; Abelló, S. SO_2-Promoted Catalytic N_2O Removal over Iron Zeolites. *Chem. Commun.* **2008**, No. 42, 5351–5353.
(33) Satsuma, A.; Maeshima, H.; Watanabe, K.; Suzuki, K.; Hattori, T. Effects of Methane and Oxygen on Decomposition of Nitrous Oxide over Metal Oxide Catalysts. *Catal. Today* **2000**, *63*.

(34) Ohnishi, C.; Asano, K.; Iwamoto, S.; Chikama, K.; Inoue, M. Alkali-Doped Co_3O_4 Catalysts for Direct Decomposition of N_2O in the Presence of Oxygen. *Catal. Today* **2007**, *120* (2), 145–150.
(35) Giecko, G.; Borowiecki, T.; Gac, W.; Kruk, J. Fe_2O_3/Al_2O_3 Catalysts for the N_2O Decomposition in the Nitric Acid Industry. *Catal. Today* **2008**, *137* (2–4), 403–409.
(36) Parres-Esclapez, S.; López-Suárez, F. E.; Bueno-López, A.; Illán-Gómez, M. J.; Ura, B.; Trawczynski, J. Rh-Sr/Al_2O_3 Catalyst for N_2O Decomposition in the Presence of O_2. *Top. Catal.* **2009**, *52* (13–20), 1832–1836.
(37) Zhang, N.; He, C.; Jing, Y.; Qian, Y.; Toyao, T.; Shimizu, K. ichi. Enhanced N_2O Decomposition on Rh/ZrO_2 Catalysts through the Promotional Effect of Palladium. *Surf. Interface* **2024**, *46*.
(38) Jing, Y.; He, C.; Zhang, N.; Murano, Y.; Toyoshima, R.; Kondoh, H.; Kageyama, Y.; Inomata, H.; Toyao, T.; Shimizu, K. I. Promotional Effect of Ag on the Catalytic Decomposition of N_2O in the Presence of O_2 over the Al_2O_3-Supported Rh Catalyst. *ACS Catal.* **2023**, *13* (19), 12983–12993.
(39) Zhang, N.; He, C.; Jing, Y.; Qian, Y.; Obuchi, M.; Toyoshima, R.; Kondoh, H.; Oka, K.; Wu, B.; Li, L.; Anzai, A.; Toyao, T.; Shimizu, K. I. Enhanced Nitrous Oxide Decomposition on Zirconium-Supported Rhodium Catalysts by Iridium Augmentation. *Environ. Sci. Technol.* **2025**, *59* (3), 1598–1607.
(40) Jing, Y.; Taketoshi, K.; Zhang, N.; He, C.; Toyao, T.; Maeno, Z.; Ohori, T.; Ishikawa, N.; Shimizu, K. I. Catalytic Decomposition of N_2O in the Presence of O_2 through Redox of Rh Oxide in a RhO_x/ZrO_2 Catalyst. *ACS Catal.* **2022**, *12* (11), 6325–6333.
(41) Chanussot, L.; Das, A.; Goyal, S.; Lavril, T.; Shuaibi, M.; Riviere, M.; Tran, K.; Heras-Domingo, J.; Ho, C.; Hu, W.; Palizhati, A.; Sriram, A.; Wood, B.; Yoon, J.; Parikh, D.; Zitnick, C. L.; Ulissi, Z. Open Catalyst 2020 (OC20) Dataset and Community Challenges. *ACS Catal* **2021**, *11* (10), 6059–6072.
(42) Takahashi, K.; Takahashi, L.; Miyazato, I.; Fujima, J.; Tanaka, Y.; Uno, T.; Satoh, H.; Ohno, K.; Nishida, M.; Hirai, K.; Ohyama, J.; Nguyen, T. N.; Nishimura, S.; Taniike, T. The Rise of Catalyst Informatics: Towards Catalyst Genomics. *ChemCatChem* **2019**, *11* (4).
(43) Kitchin, J. R. Machine Learning in Catalysis. *Nat Catal* **2018**, *1* (4), 230–232.
(44) Fung, V.; Hu, G.; Ganesh, P.; Sumpter, B. G. Machine Learned Features from Density of States for Accurate Adsorption Energy Prediction. *Nat Commun* **2021**, *12* (1), 1–11.
(45) Murdock, R. J.; Kauwe, S. K.; Wang, A. Y. T.; Sparks, T. D. Is Domain Knowledge Necessary for Machine Learning Materials Properties? *Integr Mater Manuf Innov* **2020**, *9* (3), 221–227.
(46) Toyao, T.; Maeno, Z.; Takakusagi, S.; Kamachi, T.; Takigawa, I.; Shimizu, K. I. Machine Learning for Catalysis Informatics: Recent Applications and Prospects. *ACS Catal* **2020**, *10* (3).
(47) Ras, E. J.; Rothenberg, G. Heterogeneous Catalyst Discovery Using 21st Century Tools: A Tutorial. *RSC Adv.* **2014**, *4* (12), 5963–5974.
(48) Calle-Vallejo, F.; Loffreda, D.; Koper, M. T. M.; Sautet, P. Introducing Structural Sensitivity into Adsorption-Energy Scaling Relations by Means of Coordination Numbers. *Nat Chem* **2015**, *7* (5).
(49) Ulissi, Z. W.; Medford, A. J.; Bligaard, T.; Nørskov, J. K. To Address Surface Reaction Network Complexity Using Scaling Relations Machine Learning and DFT Calculations. *Nat Commun* **2017**, *8*.
(50) Li, Z.; Wang, S.; Xin, H. Toward Artificial Intelligence in Catalysis. *Nat Catal* **2018**, *1* (9).
(51) Bruix, A.; Margraf, J. T.; Andersen, M.; Reuter, K. First-Principles-Based Multiscale Modelling of Heterogeneous Catalysis. *Nat Catal* **2019**, *2* (8).

(52) Mou, T.; Pillai, H. S.; Wang, S.; Wan, M.; Han, X.; Schweitzer, N. M.; Che, F.; Xin, H. Bridging the Complexity Gap in Computational Heterogeneous Catalysis with Machine Learning. *Nat Catal* **2023**, *6* (2).
(53) Kalikadien, A. V.; Valsecchi, C.; van Putten, R.; Maes, T.; Muuronen, M.; Dyubankova, N.; Lefort, L.; Pidko, E. A. Probing Machine Learning Models Based on High Throughput Experimentation Data for the Discovery of Asymmetric Hydrogenation Catalysts. *Chem. Sci.* **2024**, *15* (34), 13618–13630.
(54) Mosquera-Lois, I.; Kavanagh, S. R.; Ganose, A. M.; Walsh, A. Machine-Learning Structural Reconstructions for Accelerated Point Defect Calculations. *NPJ Comput Mater* **2024**, *10* (1).
(55) Taniike, T.; Takahashi, K. The Value of Negative Results in Data-Driven Catalysis Research. *Nat Catal* **2023**, *6* (2).
(56) Bae, S.; Lee, H.; Shin, J.; Kim, H. S.; Kim, Y.; Kim, D. H.; Lee, J. M. Data-Driven Inference of Synthesis Guidelines for High-Performance Zeolite-Based Selective Catalytic Reduction Catalysts at Low Temperatures. *Chemistry of Materials* **2022**, *34* (17), 7761–7773.
(57) Madaan, N.; Shiju, N. R.; Rothenberg, G. Predicting the Performance of Oxidation Catalysts Using Descriptor Models. *Catal. Sci. Technol.* **2016**, *6* (1), 125–133.
(58) Erdem Günay, M.; Yıldırım, R. Recent Advances in Knowledge Discovery for Heterogeneous Catalysis Using Machine Learning. *Catal. Rev.* **2021**, *63* (1).
(59) Ramirez, A.; Lam, E.; Gutierrez, D. P.; Hou, Y.; Tribukait, H.; Roch, L. M.; Copéret, C.; Laveille, P. Accelerated Exploration of Heterogeneous CO_2 Hydrogenation Catalysts by Bayesian-Optimized High-Throughput and Automated Experimentation. *Chem Catal.* **2024**, *4* (2).
(60) Mine, S.; Takao, M.; Yamaguchi, T.; Toyao, T.; Maeno, Z.; Hakim Siddiki, S. M. A.; Takakusagi, S.; Shimizu, K. ichi; Takigawa, I. Analysis of Updated Literature Data up to 2019 on the Oxidative Coupling of Methane Using an Extrapolative Machine-Learning Method to Identify Novel Catalysts. *ChemCatChem* **2021**, *13* (16), 3636–3655.
(61) Mine, S.; Jing, Y.; Mukaiyama, T.; Takao, M.; Maeno, Z.; Shimizu, K. I.; Takigawa, I.; Toyao, T. Machine Learning Analysis of Literature Data on the Water Gas Shift Reaction toward Extrapolative Prediction of Novel Catalysts. *Chem Lett* **2022**, *51* (3), 269–273.
(62) Wang, A. Y. T.; Kauwe, S. K.; Murdock, R. J.; Sparks, T. D. Compositionally Restricted Attention-Based Network for Materials Property Predictions. *NPJ Comput Mater* **2021**, *7* (1), 1–10.
(63) Falkowski, A. R.; Kauwe, S. K.; Sparks, T. D. Optimizing Fractional Compositions to Achieve Extraordinary Properties. *Integr Mater Manuf Innov* **2021**, *10* (4), 689–695.
(64) Wang, G.; Mine, S.; Chen, D.; Jing, Y.; Ting, K. W.; Yamaguchi, T.; Takao, M.; Maeno, Z.; Takigawa, I.; Matsushita, K.; Shimizu, K. ichi; Toyao, T. Accelerated Discovery of Multi-Elemental Reverse Water-Gas Shift Catalysts Using Extrapolative Machine Learning Approach. *Nat. Commun.* **2023**, *14* (1), 1–12.
(65) Jing, Y.; Zhang, C.; Shinya, M.; Zhang, X.; He, C.; Zhang, N.; Guo, X.; Anzai, A.; Oka, K.; Toyoshima, R.; Kondoh, H.; Takigawa, I.; Shimizu, K.; Toyao, T. Extrapolative-Machine-Learning-Guided Discovery of Multi-Elemental Heterogeneous Catalysts for Low-Temperature NO Reduction by H_2. *Res Sq* **2025**.
(66) Zhao, S.; Mine, S.; Wang, G.; Zhang, W.; Fakir, A. A. El; Yang, B.; Qin, Z.; Dostagir, N. H. M.; Matsushita, K.; Takigawa, I.; Shimizu, K.; Toyao, T. Development of Highly Active Catalysts for Low-Temperature CO_2 Hydrogenation to Methanol Using Machine Learning Approach. *ChemRxiv* **2025**.
(67) Ravel, B.; Newville, M. ATHENA, ARTEMIS, HEPHAESTUS: Data Analysis for X-Ray Absorption Spectroscopy Using IFEFFIT. *J Synchrotron Radiat* **2005**, *12* (4), 537–541.

(68) Schmack, R.; Friedrich, A.; Kondratenko, E. V.; Polte, J.; Werwatz, A.; Kraehnert, R. A Meta-Analysis of Catalytic Literature Data Reveals Property-Performance Correlations for the OCM Reaction. *Nat Commun* **2019**, *10* (1), 1–10.
(69) Kresse, G.; Furthmüller, J. Efficiency of Ab-Initio Total Energy Calculations for Metals and Semiconductors Using a Plane-Wave Basis Set. *Comput Mater Sci* **1996**, *6* (1), 15–50.
(70) Kresse, G.; Furthmüller, J. Efficient Iterative Schemes for Ab Initio Total-Energy Calculations Using a Plane-Wave Basis Set. *Phys Rev B Condens Matter Mater Phys* **1996**, *54*, 11169–11186.
(71) Perdew, J. P.; Ruzsinszky, A.; Csonka, G. I.; Vydrov, O. A.; Scuseria, G. E.; Constantin, L. A.; Zhou, X.; Burke, K. Restoring the Density-Gradient Expansion for Exchange in Solids and Surfaces. *Phys Rev Lett* **2008**, *100* (13), 136406.
(72) Blöchl, P. E. Projector Augmented-Wave Method. *Phys Rev B* **1994**, *50* (24), 17953.
(73) Grimme, S.; Ehrlich, S.; Goerigk, L. Effect of the Damping Function in Dispersion Corrected Density Functional Theory. *J Comput Chem* **2011**, *32* (7), 1456–1465.
(74) Mine, S.; Toyao, T.; Shimizu, K. I.; Hinuma, Y. Comparison of Matlantis and VASP Bulk Formation and Surface Energies in Metal Hydrides, Carbides, Nitrides, Oxides, and Sulfides. *Chem. Lett.* **2023**, *52* (9), 757–759.
(75) Wang, G.; Mine, S.; Chen, D.; Jing, Y.; Ting, K. W.; Yamaguchi, T.; Takao, M.; Maeno, Z.; Takigawa, I.; Matsushita, K.; Shimizu, K. ichi; Toyao, T. Accelerated Discovery of Multi-Elemental Reverse Water-Gas Shift Catalysts Using Extrapolative Machine Learning Approach. *Nat Commun* **2023**, *14* (1).
(76) Oviedo, F.; Ferres, J. L.; Buonassisi, T.; Butler, K. T. Interpretable and Explainable Machine Learning for Materials Science and Chemistry. *Acc Mater Res* **2022**, *3* (6), 597–607.
(77) Choudhary, K.; DeCost, B.; Chen, C.; Jain, A.; Tavazza, F.; Cohn, R.; Park, C. W.; Choudhary, A.; Agrawal, A.; Billinge, S. J. L.; Holm, E.; Ong, S. P.; Wolverton, C. Recent Advances and Applications of Deep Learning Methods in Materials Science. *NPJ Comput Mater* **2022**, *8* (1), 1–26.
(78) Pedregosa, F.; Varoquaux, G. Scikit-Learn: Machine Learning in Python. *J. Mach. Learn. Res* **2011**, *12*, 2825–2830.
(79) Jones, D. R.; Schonlau, M.; Welch, W. J. Efficient Global Optimization of Expensive Black-Box Functions. *Journal of Global Optimization* **1998**, *13*, 455–492.
(80) Scheurer, C.; Reuter, K. Role of the Human-in-the-Loop in Emerging Self-Driving Laboratories for Heterogeneous Catalysis. *Nat Catal* **2025**, *8* (1), 13–19.
(81) Taniike, T.; Takahashi, K. The Value of Negative Results in Data-Driven Catalysis Research. *Nat Catal* **2023**, *6* (2), 108–111.
(82) Toyoshima, R.; Kawai, J.; Isegawa, K.; Kondoh, H.; Junkaew, A.; Nakayama, A.; Asano, T.; Tamura, M.; Nakagawa, Y.; Yabushita, M.; Tomishige, K. Detailed Characterization of MoO_x-Modified Rh Metal Particles by Ambient-Pressure XPS and DFT Calculations. *J. Phys. Chem. C* **2021**, *125* (8), 4540–4549.
(83) Chetyrin, I. A.; Bukhtiyarov, A. V.; Prosvirin, I. P.; Khudorozhkov, A. K.; Bukhtiyarov, V. I. In Situ XPS and MS Study of Methane Oxidation on the Pd–Pt/Al_2O_3 Catalysts. *Top. Catal.* **2020**, *63* (1–2), 66–74.
(84) Minelli, S.; Rondinini, S.; He, X.; Vertova, A.; Lenardi, C.; Piazzoni, C.; Locarno, S.; Minguzzi, A. Highly Active Pd-ZrO_2 Electrodes for Hydrogen Evolution Reaction. *Sustainable Energy Fuels* **2023**, *7* (5), 1333–1342.
(85) Paredis, K.; Ono, L. K.; Behafarid, F.; Zhang, Z.; Yang, J. C.; Frenkel, A. I.; Cuenya, B. R. Evolution of the Structure and Chemical State of Pd Nanoparticles during the in Situ Catalytic Reduction of NO with H_2. *J. Am. Chem. Soc.* **2011**, *133* (34), 13455–13464.

Chapter 3

Continuous N_2O capture and reduction to N_2 using Ca-zeolite adsorbent and $Pd/La/Al_2O_3$ reduction catalyst

3.1 Introduction

It is well known that N_2O has a global warming potential approximately 300 times greater than that of CO_2 on a per-mass basis. Additionally, N_2O is a significant contributor to stratospheric ozone depletion.[1–3] Emissions of N_2O from industries that use fossil fuels, burn biomass, and chemical plants that produce nitric and adipic acids are increasing annually.[4] Without global mitigation efforts, N_2O emissions are expected to nearly double by 2050.[5] Consequently, effective catalytic post-treatment technologies must be developed to treat the N_2O emissions from stationary systems and vehicles burning transportation fuels.

Various methods exist for decomposing N_2O into harmless N_2, such as thermal, electrocatalytic, and photocatalytic systems.[6–12] Although electrocatalytic and photocatalytic systems can operate at ambient temperatures, their catalytic activities are reduced in the presence of O_2. Processes based on thermal catalysis can decompose N_2O even in the presence of O_2 through direct decomposition ($2N_2O = 2N_2 + O_2$)[13–22] or selective catalytic reduction[23–29] methods but both of these require high temperatures, typically above 300 °C. Such high reaction temperatures not only consume large amounts of energy but also limit the applicability of these techniques, especially in agriculture, which is the largest source of N_2O emission.[30,31] Therefore, it is essential to devise methods that can efficiently decompose N_2O even in the presence of O_2, especially at low temperatures.

In recent years, chemical looping has been increasingly recognized as an effective technique for various chemical transformations, particularly those associated with CO_2 utilization.[32,33] For instance, a chemical-looping system for CO_2 utilization employs CO_2 adsorbents and CO_2 reduction materials that can operate in various reactors.[34–36] This process can be used for CO_2 transformation in the presence of O_2 because the chemical absorption of CO_2 is not inhibited by O_2, and H_2 as a reductant is not simultaneously introduced into the same reactor as O_2. This is advantageous from a practical viewpoint because O_2 is often present in waste gases containing CO_2.

In this study, inspired by the aforementioned chemical-looping strategy, we developed an N_2O capture and reduction system that uses CaO-incorporated zeolites (Ca-zeolites) as N_2O adsorbents and Pd nanoparticles on La-containing Al_2O_3 (Pd/La/Al_2O_3) as the reduction catalyst. This new process is suitable for continuous operation under temperature-swing cycling between 50 and 150 °C. The N_2O capture capacity and subsequent reduction ability were maintained for at least 15 h (10 cycles). Notably, this process can be performed at low temperatures (below 150 °C) via a simple temperature-swing operation in the presence of O_2.

3.2 Experimental details

3.2.1 Chemicals and catalyst preparation

Various zeolites were used to prepare the ion-exchanged zeolite materials: MOR (JRC-Z-HM20(5), Si/Al = 9.1, Tosoh Co.), MFI (HSZ-820NHA, Si/Al = 11.15, Tosoh Co.), CHA (Si/Al ratio = 11.15, Tosoh Co.), BEA (HSZ-920NHA, Si/Al = 8.75, Tosoh Co.), Y (HSZ-372HUA, Si/Al = 15, Tosoh Co.). The following compounds were used for zeolite ion exchange: $Mg(NO_3)_2$ (>99.2%, Kanto Chemical Co. Inc.), $Ca(NO_3)_2$ (>98.5%, Wako Pure Chemical Industries), $Sr(NO_3)_2$ (>98.0%, Kanto Chemical Co. Inc.), $Ba(NO_3)_2$ (>99.0%; Wako Pure Chemical Industries), $Ce(NO_3)_3$ (>98.0%; Wako Pure Chemical Industries). For ion exchange, 1 g of zeolite powder was mixed with 50 mL of an aqueous solution of the precursor in which the molar amount of the precursor was five times that of Al in the zeolite. The slurry was then heated at 60 °C for 4 h under stirring. The as-prepared sample was recovered by centrifugation at 4000 rpm, dried at 110 °C for 12 h, and then calcined at 500 °C for 3 h to obtain ion-exchanged zeolite materials. The La-containing Al_2O_3-supported Pd catalyst ($Pd/La/Al_2O_3$) was prepared using the impregnation method described in our previous paper.[37] The loading amount of Pd and La in $Pd/La/Al_2O_3$ are 1 wt.% and 15 wt.%, respectively.

3.2.2 Characterization

X-ray diffraction (XRD) patterns were obtained using a Rigaku MiniFlex II/AP diffractometer with Cu-Kα radiation. The quantity of the incorporated metal species was determined using energy-dispersive X-ray fluorescence spectrometry (EDX-700HS, Shimadzu).

In situ infrared (IR) spectra were collected in transmission mode using an FT/IR-4600 (JASCO) unit with a TGS detector. A self-supporting disk of the sample (40 mg) was placed in a handmade *in situ* glass cell with CaF_2 windows. For *in situ* IR experiments, N_2O was fed into the cell at 50 °C through a conventional flow reaction system at a total flow rate of 100 mL/min. Before the measurements, the catalysts were pretreated *in situ* under He flow at 500 °C for 30 min. Temperature-programmed desorption of N_2O (N_2O-TPD) was performed using a BELCAT II instrument (MicrotracBEL). After the He pretreatment at 500 °C for 30 min, the sample was exposed to 10% N_2O/He (20 mL/min) at 50 °C for 30 min, followed by purging with He for 10 min. The sample was heated to 250 °C at a rate of 10 °C/min.

3.2.3 Breakthrough reaction

Breakthrough experiments were performed with a feed of 500 ppm N_2O, 500 ppm N_2O + 5% CO_2, or 500 ppm N_2O + 3% H_2O at a total flow rate of 50 mL/min. Before the breakthrough experiment, the sample was pretreated under He flow (50 mL/min) at 500 °C for 30 min. The effluent gas stream was monitored using an online FT-IR spectrometer (JASCO FT/IR-4600) with a TGS detector (20 scans with a resolution of 4 cm^{-1}) and a custom-built gas cell (CaF_2 windows).

3.2.4 N_2O capture and reduction

N_2O capture and reduction experiments were performed using a continuously separated fixed-bed flow system (**Scheme 3.1**). Two reactors containing 300 mg of Ca-MOR zeolite were set in parallel, where one reactor captured the N_2O selectively from the mixture of 0.1% N_2O and 10% O_2 (50 mL/min, He balance), and the other released N_2O by heating the Ca-MOR zeolite from 50 to 150 °C (20 °C/min) under a flow of 4% H_2/He (50 mL/min). The effluent from the N_2O capture reactor was monitored using an online FT-IR spectrometer (JASCO FT/IR-4600) equipped with a TGS detector (20 scans at a resolution of 4 cm^{-1}). The released N_2O was then fed into a Pd/La/Al_2O_3 catalyst for the reduction of N_2O at 150 °C. The effluent of Pd/La/Al_2O_3 was monitored using a mass spectrometer (MS) apparatus (BELMass, MicrotracBEL Corp).

3.2.5 Computational methods

Periodic DFT calculations were performed using the Vienna Ab Initio Simulation Package (VASP, version 5.4.4)[38,39] and Matlantis.[40] For VASP, the Perdew–Burke–Ernzerhof functional revised for solids (PBEsol)[41] was employed in combination with the projector-augmented wave (PAW) method.[42] A kinetic energy cutoff of 400 eV was used for plane-wave basis sets. Gaussian smearing (width: 0.2 eV) was applied to occupy the electronic level. The k-point mesh included only the gamma point of the Brillouin zone (1 × 1 × 1). The van der Waals interactions are described using a dispersion-corrected DFT-D3 (BJ) function.[43] The convergence of the force on each atom was set to 0.03 eV $Å^{-1}$. The adsorption energy (E_{ads}) of a molecule is defined as:

$$E_{ads} = E_{A/S} - E_A - E_S \quad (1)$$

where $E_{A/S}$, E_A, and E_S are the electronic energies of the adsorption complex, free-state adsorbate, and the bare Ca-MOR structure, respectively.

Periodic universal neural network potential (NNP) calculations were performed using Matlantis (version 3.0.0, CRYSTAL_U0_PLUS_D3 mode: crystal systems (without Hubbard U correction) + DFT-D3 dispersion correction). All-atom energy optimizations were conducted using the Broyden–Fletcher–Goldfarb–Shanno algorithm with a force threshold of 0.01 eV Å^{-1}.

3.2.6 *Ab initio* thermodynamic analyses

Ab initio thermodynamic analysis[44,45] was performed to investigate the effects of the reaction gases (O_2 and H_2O) and temperature on the calcium oxide species in the alumina-loaded zeolites. The enthalpy and entropy at each temperature and standard state pressure (1 atm) were obtained from the NIST-JANAF Thermochemical Tables.[46] The energies of the gas molecules were obtained using a large empty unit cell (25 Å × 25 Å × 25 Å) to mimic the isolated species. The equilibrium reaction, energy change (ΔE), Gibbs free energy change (ΔG), and chemical potential change ($\Delta\mu$) under O_2 and H_2O atmospheres are given by Eqs. (2)–(5), respectively.

$$xCaO + SiO_2(Al) + \frac{1}{2}H_2O + \left(-\frac{1}{2}x + \frac{1}{2}y - \frac{1}{4}z\right)O_2 \rightarrow Ca_xO_yH_z/SiO_2(Al) \quad (2)$$

$$\Delta E = E\left[Ca_xO_yH_z/SiO_2(Al)\right] - xE[\mathrm{CaO}] - E[SiO_2(Al)] - \frac{1}{2}E[H_2O] - \left(-\frac{1}{2}x + \frac{1}{2}y - \frac{1}{4}z\right)E[O_2] \quad (3)$$

$$\Delta G(T,p) = \Delta E - \frac{1}{2}\Delta\mu_{H_2O} - \left(-\frac{1}{2}x + \frac{1}{2}y - \frac{1}{4}z\right)\Delta\mu_{O_2} \qquad \left(p = \frac{p_{gas}}{p^0}\right) \quad (4)$$

$$\Delta\mu_{gas} = \Delta\mu_{gas}(T,p^0) + RTln\left(\frac{p_{gas}}{p^0}\right) \ (\mathrm{gas} = \mathrm{O_2 \ and \ H_2O}) \quad (5)$$

Here, $Ca_xO_yH_z/SiO_2(Al)$ is the Al-loaded Ca-MOR species, $E[Ca_xO_yH_z/SiO_2(Al)]$ is the total energy of the species, $E[SiO_2(Al)]$ is the total energy of the Al-loaded MOR model, $E[O_2]$ and $E[H_2O]$ are the total energies of the gas molecules, $\Delta\mu_{gas}$ is the change in the chemical potential of the gases involved in the reaction (Eq. (5)), T is the temperature (K), p^0 is the atmospheric pressure, and p_{gas} is the partial pressure of the reaction gas.

3.3 Results and discussion

3.3.1 Catalyst properties

Figure 3.1 shows the N_2O-TPD profiles of various ion-exchanged zeolite materials. The desorption amount of N_2O in the temperature range of 50–250 °C was used to compare the adsorption capacity of N_2O. The obtained results show that the ion-exchanged Ca-MOR zeolite exhibited the highest N_2O adsorption capacity at 50 °C compared with the other samples prepared in this study. In addition, Ca-$MOR_{Si/Al=110}$ and Ca-$MFI_{Si/Al=90}$, which were prepared by ion-exchange method using zeolites with high Si/Al ratios, exhibit negligible N_2O adsorption at 50 °C, indicating that the amount of Al sites in the zeolite plays an important role in N_2O adsorption. The Ca loading amount in Ca-MOR was determined to be 1.83 wt.% (Ca/Al = 0.28) using energy-dispersive X-ray fluorescence spectrometry (EDX-700HS, Shimadzu Corp.). **Figure 3.2** shows XRD patterns of the Ca-exchanged MOR (Ca-MOR) and H-MOR samples. The XRD peaks observed for Ca-MOR are identical to those of H-MOR, without the presence of peaks for Ca species, indicating that the Ca species in Ca-MOR are well dispersed. Additionally, a Ca-loaded MOR specimen (Ca/Al = 1) was prepared as a reference with wetness impregnation method using $Ca(NO_3)_2$ as precursor. The as-prepared Ca-loaded MOR showed no ability to adsorb N_2O in the N_2O-TPD experiments (data not shown), indicating that the Ca species loaded on the surface of MOR zeolite are inefficient for the adsorption of N_2O. These results suggest that the Ca-species contributing to the N_2O adsorption are dispersed within the cage of the MOR zeolite.

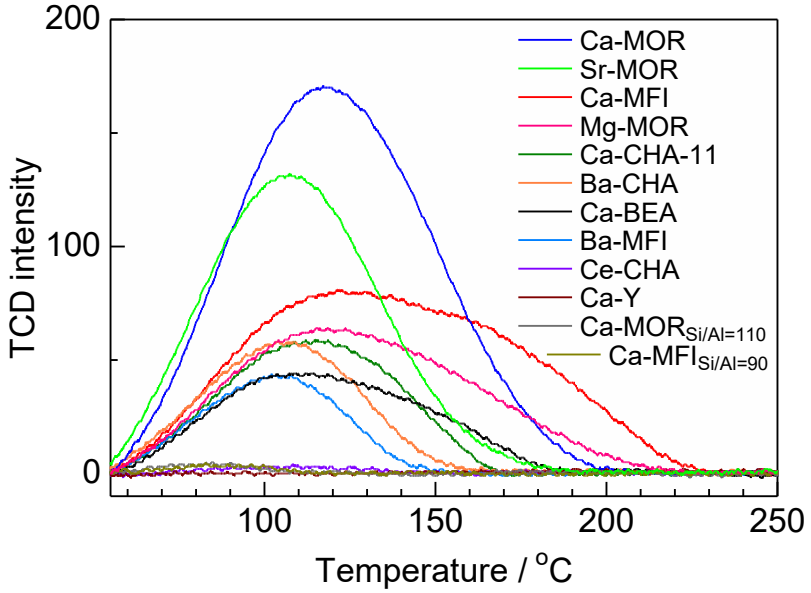

Figure 3.1 N_2O-TPD profile over different ion-exchanged zeolite materials after exposure to 10% N_2O/He at 50 °C for 30 min followed by a He purge for 10 min. The sample was heated from 50 to 250 °C at a rate of 10 °C/min.

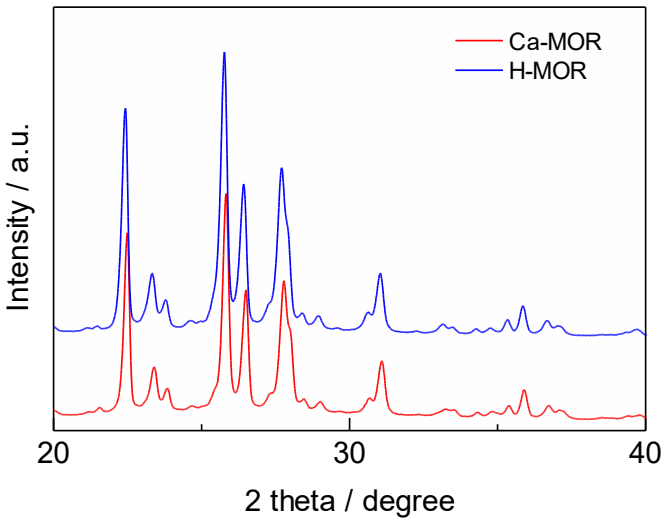

Figure 3.2 XRD patterns of H-MOR and Ca-MOR zeolites.

A computational investigation was conducted to clarify the possible structures of the CaO species introduced in the zeolite. An *ab initio* thermodynamic approach was used to evaluate the system stability under certain conditions by calculating the Gibbs free energy change (ΔG) values. Three types of MOR zeolites with different Al positions and sites were considered in this study: (i) MOR with one Al atom, (ii) MOR with two Al in an 8-membered ring (8MR), and (iii) MOR with two Al in a 5-membered ring (5MR).[47–50] The Al position in structure (VIII) is the most stable and widely used. We also investigated the position of the second Al atom by fixing the first atom and selecting structures (VII) and (II) as representative models with fairly stable structures to investigate the 5MR and 8MR as possible Al sites (**Figure 3.3**). Subsequently, various Ca oxide clusters with 1–3 Ca atoms were placed in each structure (**Figure 3.4–6**). Only the most stable structures for each chemical formulation are depicted for clarity. The valence state of Ca was set to 2+ for all structures because other valence states, such as 0 and +1, are unlikely under ambient conditions. **Figure 3.7** shows the phase diagram of the Ca oxide species with the lowest ΔG values as a function of the temperature and partial pressure of O_2. The results were obtained using VASP. Only mononuclear and dinuclear Ca species were stable in all MOR models, whereas the trimeric species were relatively unstable under these conditions.

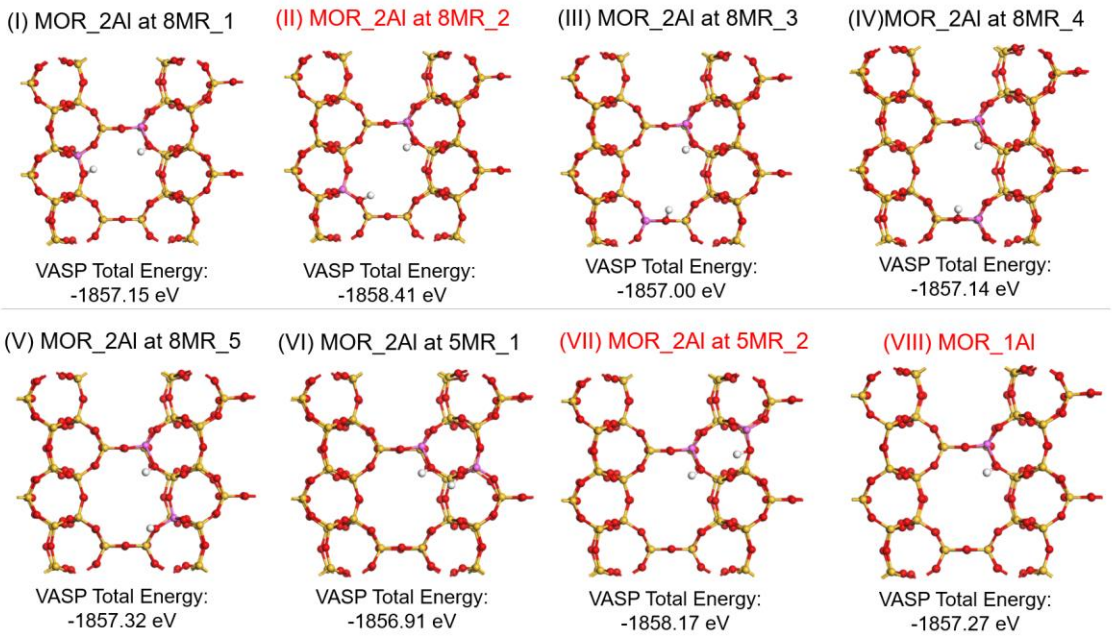

Figure 3.3 List of the MOR structures considered in this study that has different Al positions and their total energies (TOTEN in the figure) obtained using VASP; pink: Al; red: O; yellow: Si; white: H.

Number of Ca atoms	Structure of $Ca_xO_yH_z$ in MOR_1Al
1	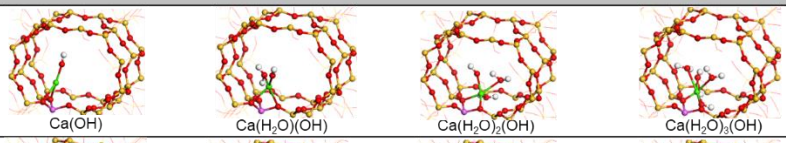
2	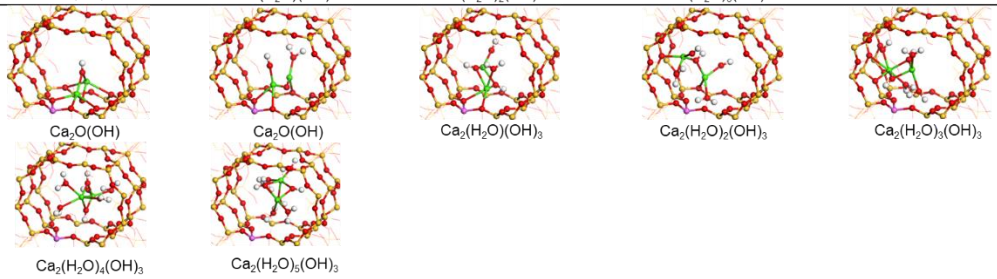
3	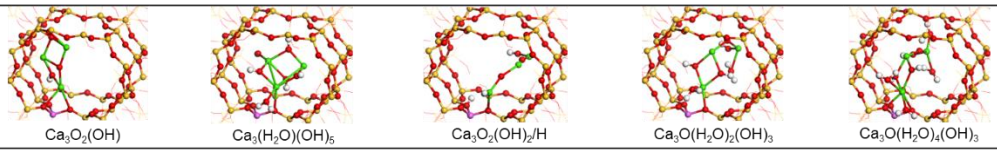

Figure 3.4 Side views of the optimized structure models of $Ca_xO_yH_z$ in MOR_1Al used for computational study (VASP). Color code: green: Ca; pink: Al; red: O; yellow: Si; white: H.

Number of Ca atoms	Structure of $Ca_xO_yH_z$ in MOR_2Al at 8MR
1	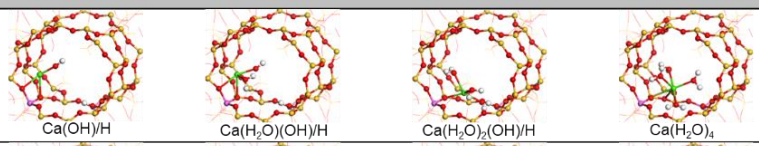
2	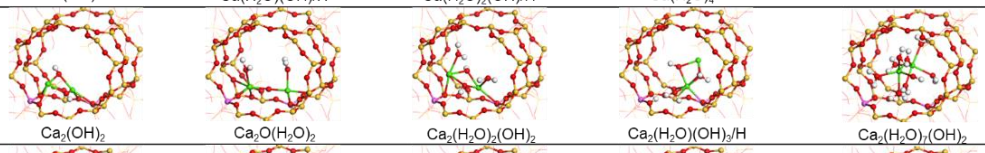
3	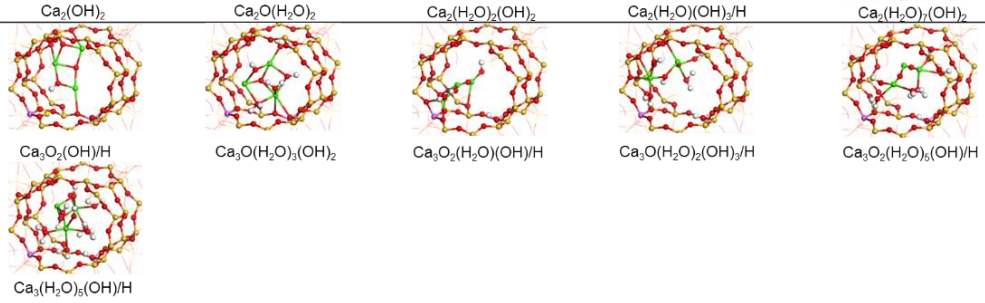

Figure 3.5 Side views of the optimized structure models of $Ca_xO_yH_z$ in MOR_2Al at 8MR used for computational study (VASP). Color code: green: Ca; pink: Al; red: O; yellow: Si; white: H.

Number of Ca atoms	Structure of $Ca_xO_yH_z$ in MOR_2Al at 5MR
1	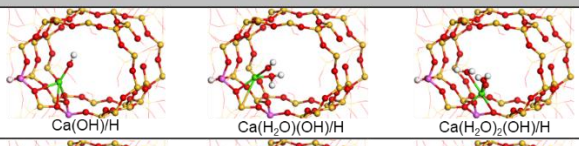
2	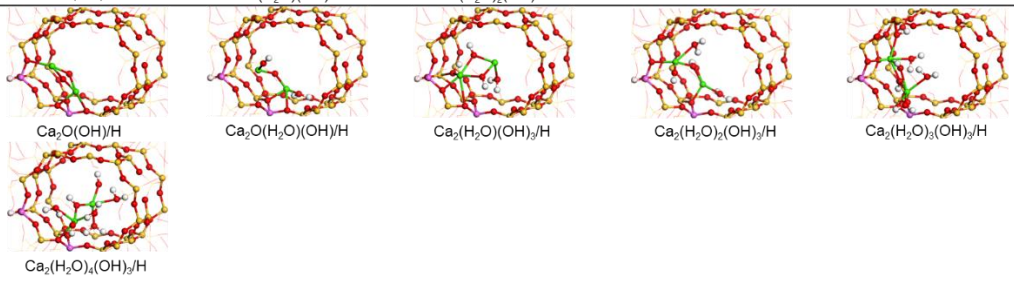
3	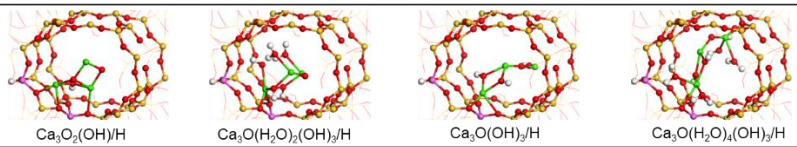

Figure 3.6 Side views of the optimized structure models of $Ca_xO_yH_z$ in MOR_2Al at 5MR used for computational study (VASP). Color code: green: Ca; pink: Al; red: O; yellow: Si; white: H.

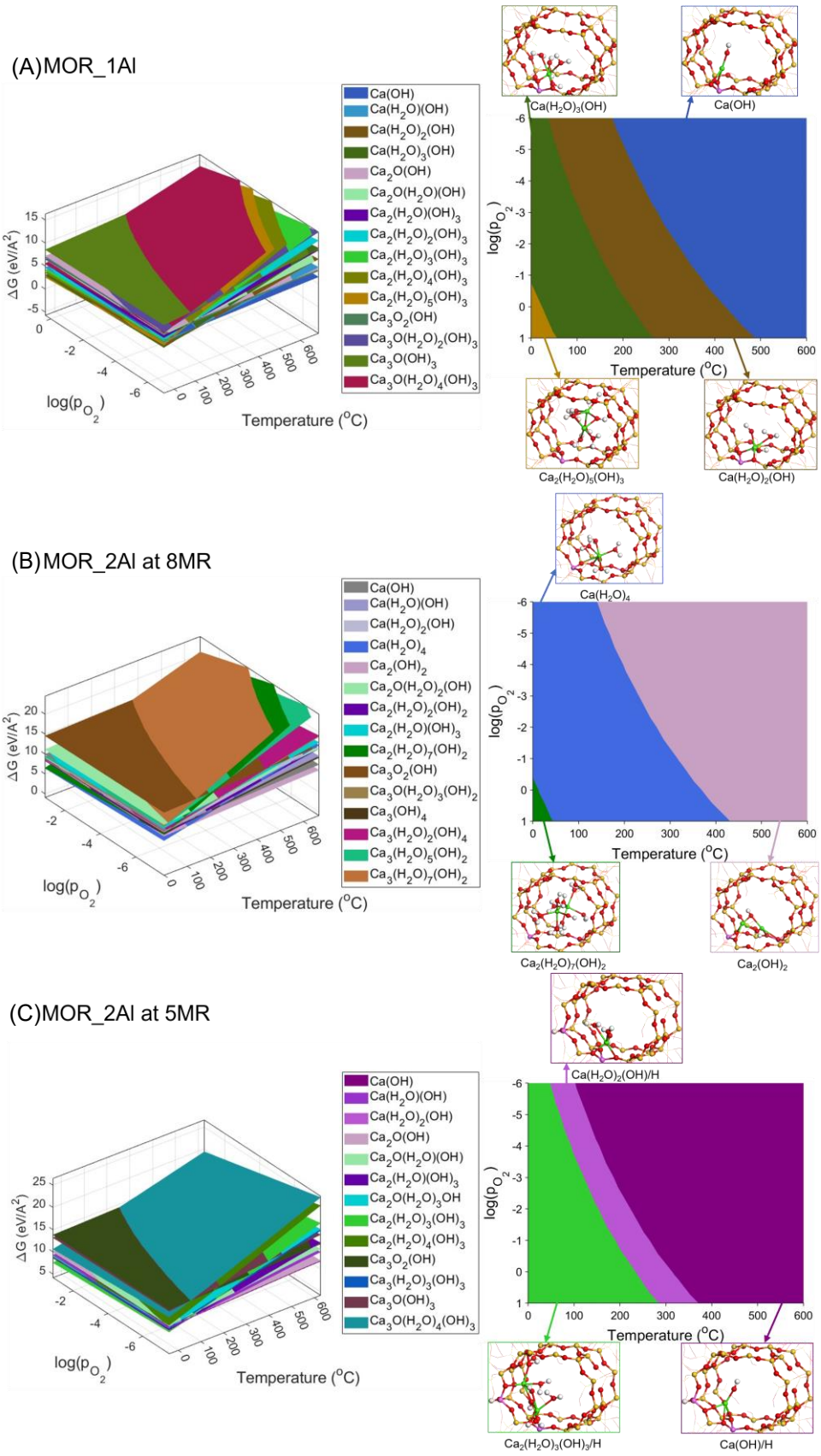

Figure 3.7 3D (left) and 2D (right) phase diagrams for (a) MOR_1Al, (b) MOR_2Al at 8MR, and (c) MOR_2Al at 5MR showing the species with the lowest Gibbs free energy change (Δ*G*) in terms of temperature and O_2 partial pressure (log scale) and possible structures. All calculations were performed using VASP (green, Ca; pink, Al; red, O; yellow, Si; white, H).

3.3.2 N_2O adsorption/desorption and breakthrough results

The *in situ* IR spectra of N_2O adsorbed on Ca-MOR and H-MOR at 50 °C are shown in **Figure 3.8A**. No adsorption peaks were observed for H-MOR, indicating that no N_2O molecules were adsorbed onto its surface. After Ca-MOR was exposed to N_2O, two peaks at 2246 and 2273 cm^{-1} were observed, which are assigned to the N–N vibrational mode of N_2O molecules adsorbed on Ca sites.[51–53] These results indicate that the Ca species in Ca-MOR account for its superior N_2O adsorption capacity. **Figure 3.8A** also shows the *in situ* IR spectra of N_2O adsorbed on Ca-MOR collected under He with increasing temperature from 50 to 150 °C after exposure to 0.1% N_2O/He for 30 min and subsequent purging under He. The intensity of the N_2O molecules adsorbed on the Ca species decreased with increasing temperature, and gaseous N_2O was detected in the effluent of the *in situ* IR cell, as shown in **Figure 3.8B**. A desorption peak of N_2O was observed at ~90 °C with a shoulder peak at ~125 °C, suggesting the presence of adsorbed N_2O molecules with different adsorption strengths.

Under practical conditions, O_2, CO_2, and H_2O often coexist in N_2O feed gas.[54,55] Therefore, breakthrough experiments were performed to investigate the effects of O_2, CO_2, and H_2O on the adsorption capacity of N_2O of Ca-MOR. The results of the breakthrough experiments (**Figure 3.9**) show that the presence of O_2 has almost no impact on the N_2O capture ability of Ca-MOR, indicating that Ca-MOR can selectively capture N_2O in the presence of O_2. However, the presence of 3% H_2O decreased the adsorption amount of N_2O on Ca-MOR significantly. The Ca-MOR only exhibited limited N_2O adsorption capacity in the presence of 5% CO_2. These results indicate that CO_2 and H_2O affect the N_2O capture ability of Ca-MOR, and thus, they should be removed from the N_2O feed to ensure that Ca-MOR maintains high efficiency for N_2O capture.[56–58] Moreover, the quantity of adsorbed N_2O was determined to be 2.40×10^{-4} mole/g_{cat} using the N_2O feeding amount during breakthrough experiments before the detect of N_2O in the effluent under the flow of N_2O/He. The efficiency of ion-exchanged Ca cations was thus determined to be 0.53 N_2O_{ad}/Ca^{2+}.

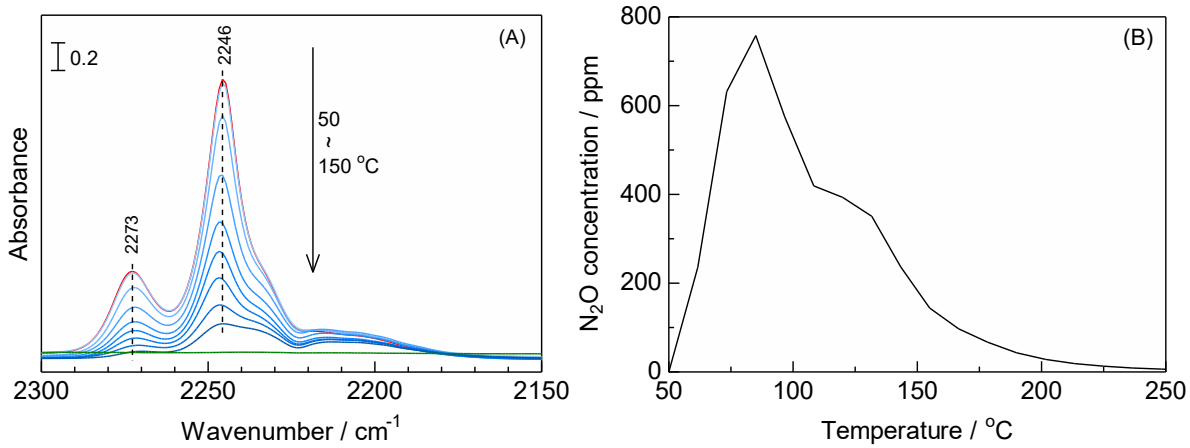

Figure 3.8 (A) *In situ* IR spectra of N_2O adsorbed on Ca-MOR under the flow of He; red/green: N_2O adsorbed on Ca-MOR/H-MOR at 50 °C after purging under He for 30 min followed by the introduction of 0.1% N_2O/He for 30 min; blue: N_2O adsorbed on Ca-MOR during heating from 50 to 150 °C. (B) Concentration of N_2O in the effluent of the *in situ* IR cell during the measurement with Ca-MOR while increasing the temperature of the *in situ* cell from 50 to 150 °C at a rate of 10 °C/min.

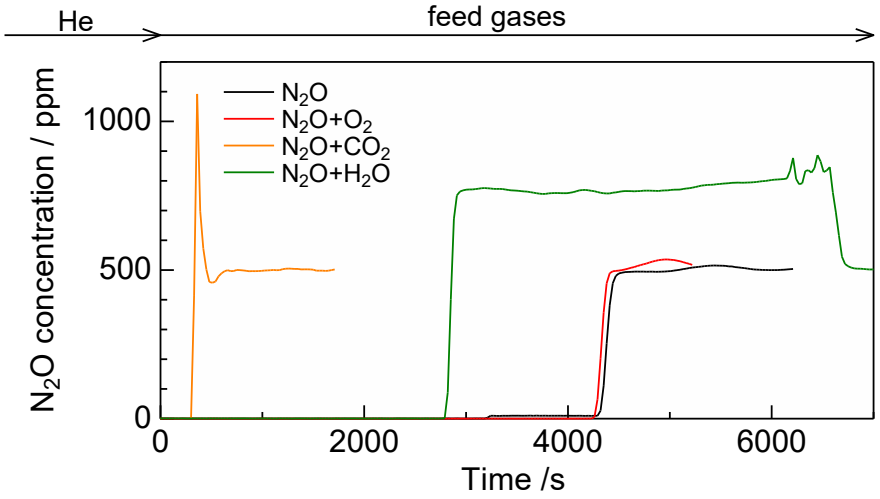

Figure 3.9 Profile of the breakthrough experiments over Ca-MOR zeolite under a flow of (a) 500 ppm N_2O, (b) 500 ppm N_2O + 10% O_2, (c) 500 ppm N_2O + 5% CO_2, and (d) 500 ppm N_2O + 3% H_2O at 50 °C. Weight of Ca-MOR: 100 mg, total flow rate = 50 mL/min, He balance. The feed gases were introduced to Ca-MOR from 0 s.

Figure 3.11 shows the *in situ* IR spectra of N_2O adsorbed on Ca/MOR after the introduction of O_2, CO_2, or H_2O. The spectra of N_2O adsorbed on Ca-MOR were collected after the introduction of 0.1% N_2O at 50 °C for 30 min. After the introduction of 10% O_2 to the N_2O feed gas, the absorbance intensity of adsorbed N_2O exhibited almost no change, indicating that the presence of O_2 negligibly affects the adsorption of N_2O, which is consistent with the results of the breakthrough experiments. After the introduction of CO_2, the intensities of the peaks at 2273 and 2246 cm^{-1} decreased, and a new peak appeared at 1377 cm^{-1} (**Figure 3.11B**). The peak at 1377 cm^{-1} was assigned to CO_2 adsorbed on Ca species in zeolite.[59] The peaks related to the adsorption of N_2O onto Ca sites were not observed after

the introduction of 5% CO_2 for 10 min. These results suggest that the presence of CO_2 inhibited the adsorption of N_2O because of the higher adsorption strength of CO_2 on Ca than that of N_2O. A similar evolution of the peaks of adsorbed N_2O was observed after the introduction of 3% H_2O (**Figure 3.11C**). After the introduction of 3% H_2O, the peak intensity of adsorbed N_2O decreased, and the peak at 1625 cm^{-1} related to adsorbed H_2O, increased.

We conducted a theoretical investigation of the adsorption energies of various adsorbates, such as N_2O, CO_2, H_2O, and O_2 on the Ca-oxo clusters in MOR zeolite, which were identified by ab initio thermodynamic analysis using VASP. Overall, we found that the adsorption of N_2O was weaker than that of CO_2 or H_2O but stronger than that of O_2 (**Figure 3.10**). These results are in good agreement with the findings of the *in situ* IR experiments.

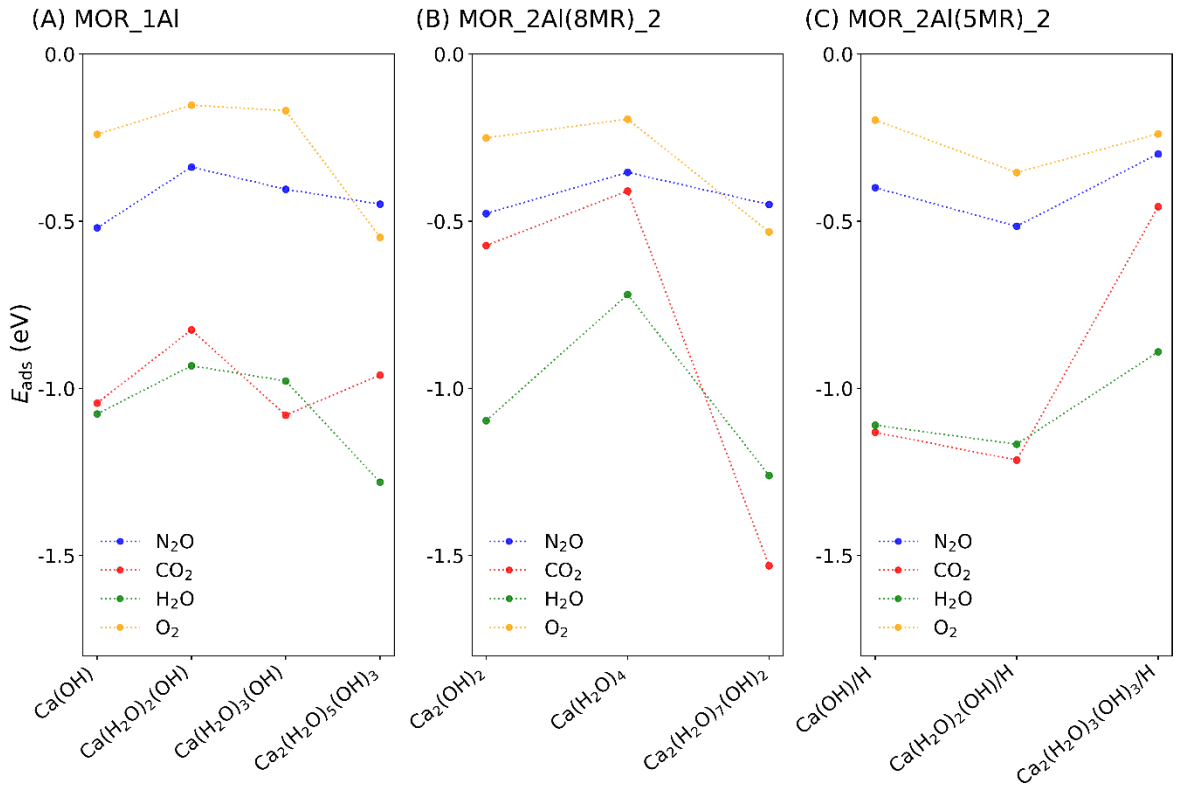

Figure 3.10 E_{ads} of N_2O, CO_2, H_2O, and O_2 on Ca-oxo clusters in the MOR zeolite with various structures.

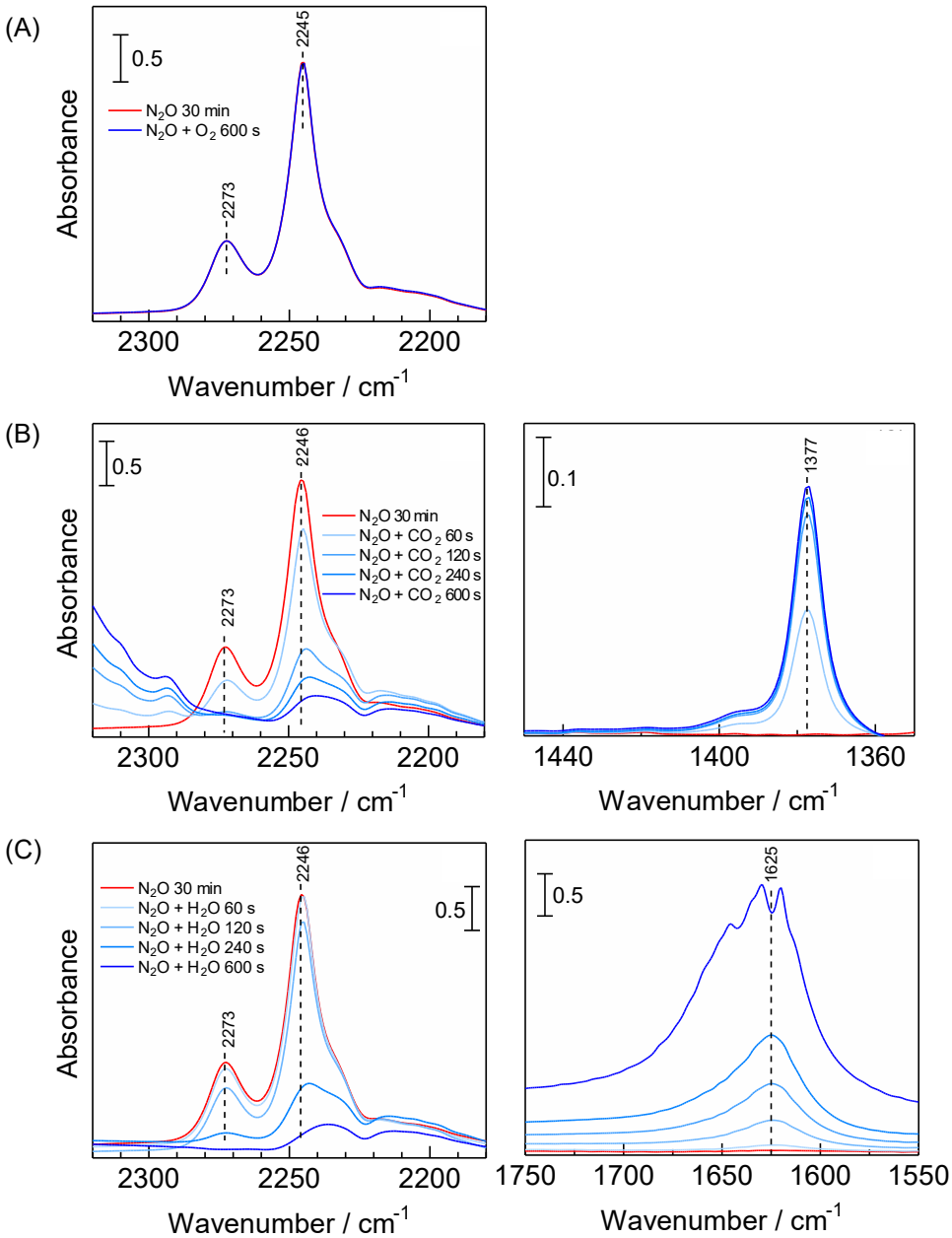

Figure 3.11 *In situ* IR spectra of Ca-MOR after the introduction of (A) 10% O_2, (B) 5% CO_2, and (C) 3% H_2O following the introduction of 0.1% N_2O at 50 °C for 30 min. Weight of Ca/MOR: 40mg, total flow rate: 50 mL/min. Before the introduction of 0.1% N_2O, the Ca-MOR pellet was pretreated under the flow of He at 500 °C for 30 min and then cooled to 50 °C.

3.3.3 N_2O adsorption and reduction

Although N_2O is considered a significant greenhouse gas, its removal from gas streams remains challenging, especially at low temperatures and in the presence of O_2, which is prevalent in various N_2O sources.[30] In this study, we developed a continuous N_2O capture and reduction system in which N_2O could be selectively captured in the presence of O_2 and reduced to N_2 at relatively low temperatures, as shown in **Scheme 3.1**. Two reactors containing Ca-MOR were set up in parallel for the capture or release of N_2O. The effluent composition for N_2O capture was monitored by IR spectroscopy. After feeding 500 ppm N_2O + 10% O_2 for 40 min, the N_2O + O_2 feed was switched to the other reactor containing the same Ca-MOR material. The captured N_2O was released by heating the Ca-MOR to 150 °C at a heating rate of 20 °C/min, and then cooling to 50 °C. The liberated N_2O was fed into the downstream section of the system, where the $Pd/La/Al_2O_3$ catalyst was positioned and maintained at 150 °C throughout the process, along with a 4% H_2 flow. The composition of the effluent gas from the reactor equipped with $Pd/La/Al_2O_3$ was monitored using mass spectrometry.

Figure 3.12 shows the performance of the continuous N_2O capture and reduction system. During the heating of Ca-MOR from 50 to 150 °C, the formation of N_2 was observed with a maximum concentration of ~12000 ppm and almost no N_2O was detected, indicating that all the N_2O released from Ca-MOR was efficiently reduced into N_2 by H_2 over $Pd/La/Al_2O_3$. In addition, no N_2O was detected using IR (data not shown), indicating that almost all of the supplied N_2O was captured by Ca-MOR. These results reveal that the N_2O capture capacity and subsequent reduction ability of the continuous N_2O capture and reduction systems were preserved for at least 15 h (10 cycles) in the presence of O_2.

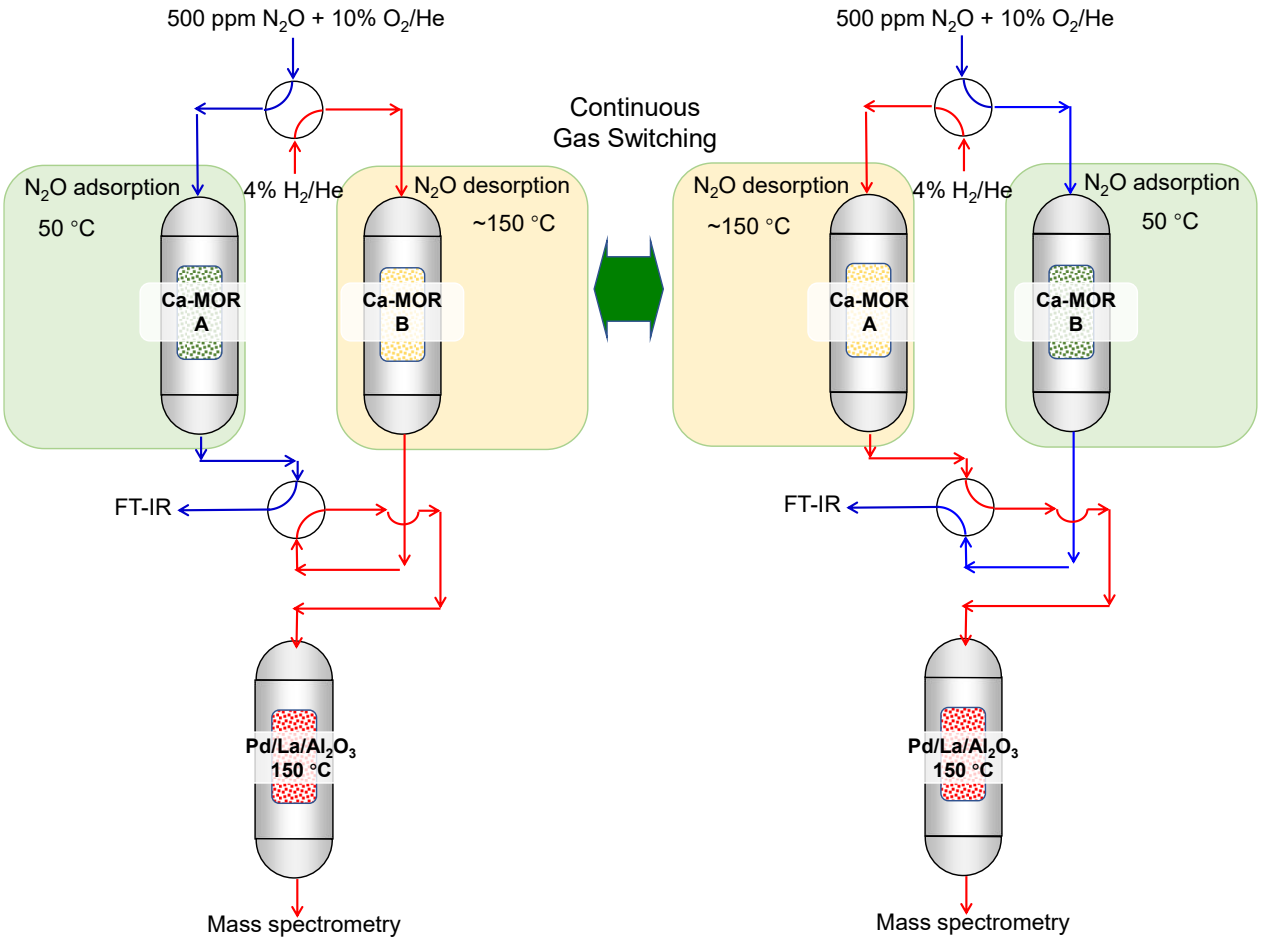

Scheme 3.1 Scheme of the continuous N_2O capture and reduction system using Ca-MOR zeolite as the N_2O capture adsorbent and Pd/La/Al_2O_3 as the reduction catalyst. The temperature of the Ca-MOR for N_2O capture was set to 50 °C, while the temperature was increased from 50 to 150 °C at a rate of 20 °C/min during the desorption phase. The downstream Pd/La/Al_2O_3 section was set at 150 °C throughout the process. The gas type was switched every 40 min.

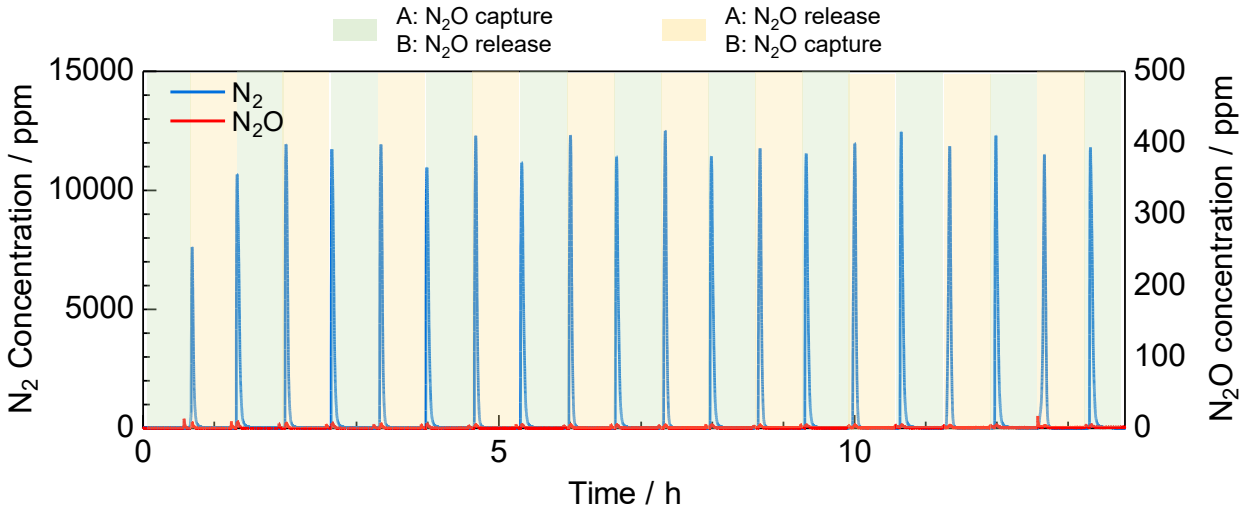

Figure 3.12 Performance of the Ca-MOR-Pd/La/Al_2O_3 continuous N_2O capture and reduction system. The gas fed to the Ca-MOR was switched between 500 ppm N_2O + 10% O_2 and 4% H_2/He every 40 min.

3.4 Conclusion

In this study, a series of alkali metal-exchanged zeolite samples were prepared, and their N_2O capture capacities were estimated. The obtained results demonstrate that Ca-MOR shows high efficiency for N_2O capture. Therefore, a continuous N_2O capture and reduction system was developed using Ca-MOR as an N_2O adsorbent and Pd/La/Al_2O_3 for N_2O reduction. This process is suitable for continuous operation under temperature-swing cycles between 50 and 150 °C, and the N_2O capture and subsequent reduction performance was preserved for at least 15 h (10 cycles). Notably, this process can operate at low temperatures (below 150 °C) through a simple temperature-swing operation in the presence of O_2.

3.5 References

(1) Ravishankara, A. R.; Daniel, J. S.; Portmann, R. W. Nitrous Oxide (N_2O): The Dominant Ozone-Depleting Substance Emitted in the 21st Century. *Science (1979)* **2009**, *326*, 123–125.

(2) Li, L.; Xu, J.; Hu, J.; Han, J. Reducing Nitrous Oxide Emissions to Mitigate Climate Change and Protect the Ozone Layer. *Environ Sci Technol* **2014**, *48*, 5290–5297.

(3) Yamashita, K.; Liu, Z.; Iyoki, K.; Chen, C. T.; Miyagi, S.; Yanaba, Y.; Yamauchi, Y.; Okubo, T.; Wakihara, T. Synthetic and Natural MOR Zeolites as High-Capacity Adsorbents for the Removal of Nitrous Oxide. *Chem. Commun.* **2021**, *57*, 1312–1315.

(4) Pérez-Ramírez, J.; Kapteijn, F.; Schöffel, K.; Moulijn, J. A. Formation and Control of N_2O in Nitric Acid Production: Where Do We Stand Today? *Appl Catal B* **2003**, *44*, 117–151.

(5) Konsolakis, M. Recent Advances on Nitrous Oxide (N_2O) Decomposition over Non-Noble-Metal Oxide Catalysts: Catalytic Performance, Mechanistic Considerations, and Surface Chemistry Aspects. *ACS Catal* **2015**, *5*, 6397–6421.

(6) Kapteijn, F.; Rodriguez-Mirasol, J.; Moulijn, J. A. Heterogeneous Catalytic Decomposition of Nitrous Oxide. *Appl Catal B* **1996**, *9*, 25–64.

(7) Kudo, A.; Mine, A. Electrocatalytic Reduction of Nitrous Oxide on Metal and Oxide Electrodes in Aqueous Solution. *Appl Surf Sci* **1997**, *121/122*, 538–542.

(8) Jabłońska, M.; Palkovits, R. Nitrogen Oxide Removal over Hydrotalcite-Derived Mixed Metal Oxides. *Catal. Sci. Technol.* **2016**, *6*, 49–72.

(9) Jabłońska, M.; Arán, M. A.; Beale, A. M.; Delahay, G.; Petitto, C.; Nocuń, M.; Palkovits, R. Understanding the Origins of N_2O Decomposition Activity in Mn(Fe)$CoAlO_x$ Hydrotalcite Derived Mixed Metal Oxides. *Appl Catal B* **2019**, *243*, 66–75.

(10) Ko, B. H.; Hasa, B.; Shin, H.; Zhao, Y.; Jiao, F. Electrochemical Reduction of Gaseous Nitrogen Oxides on Transition Metals at Ambient Conditions. *J Am Chem Soc* **2022**, *144* (3), 1258–1266.

(11) Kim, K.; Byun, J.; Kim, H.; Lee, K. S.; Lee, H. S.; Kim, J.; Hyeon, T.; Kim, J. J.; Han, J. W. Systematic Approach to Designing a Highly Efficient Core–Shell Electrocatalyst for N_2O Reduction. *ACS Catal* **2021**, *11* (24), 15089–15097.

(12) M. L. Ovcharov, V. M. G. Photocatalytic Conversion of Nitrogen Oxides: Current State and Perspectives: A Review. *Theor. Exp. Chem.* **2021**, *57*, 30–63.

(13) Oi, J.; Obuchi, A.; Bamwenda, G. R.; Ogata, A.; Yagita, H.; Kushiyama, S.; Mizuno, K. Decomposition of Nitrous Oxide over Supported Rhodium Catalysts and Dependency on Feed Gas Composition. *Appl Catal B* **1997**, *12*, 277–286.

(14) Satsuma, A.; Maeshima, H.; Watanabe, K.; Suzuki, K.; Hattori, T. Effect of Oxygen on Decomposition of Nitrous Oxide over Various Metal Oxide Catalysts. *Catal Today* **2000**, *63*, 347–353.

(15) Parres-Esclapez, S.; López-Suárez, F. E.; Bueno-López, A.; Illán-Gómez, M. J.; Ura, B.; Trawczynski, J. Rh-Sr/Al_2O_3 Catalyst for N_2O Decomposition in the Presence of O_2. *Top Catal* **2009**, *52* (13–20), 1832–1836.

(16) Kim, M. J.; Kim, Y. J.; Lee, S. J.; Ryu, I. S.; Kim, H. J.; Kim, Y.; Ko, C. H.; Jeon, S. G. Enhanced Catalytic Activity of the Rh/γ-Al_2O_3 Pellet Catalyst for N_2O Decomposition Using High Rh Dispersion Induced by Citric Acid. *Chem. Eng. Res. Des.* **2019**, *141*, 455–463.

(17) Li, Y.; Sundermann, A.; Gerlach, O.; Low, K. Bin; Zhang, C. C.; Zheng, X.; Zhu, H.; Axnanda, S. Catalytic Decomposition of N_2O on Supported Rh Catalysts. *Catal Today* **2020**, *355*, 608–619.

(18) Hinokuma, S.; Iwasa, T.; Kon, Y.; Taketsugu, T.; Sato, K. N_2O Decomposition Properties of Ru Catalysts Supported on Various Oxide Materials and SnO_2. *Sci Rep* **2020**, *10* (1).

(19) Hinokuma, S.; Iwasa, T.; Kon, Y.; Taketsugu, T.; Sato, K. Effects of Support Materials and Ir Loading on Catalytic N_2O Decomposition Properties. *Catal Commun* **2021**, *149*.
(20) Jing, Y.; Taketoshi, K.; Zhang, N.; He, C.; Toyao, T.; Maeno, Z.; Ohori, T.; Ishikawa, N.; Shimizu, K. Catalytic Decomposition of N_2O in the Presence of O_2 through Redox of Rh Oxide in a RhO_x/ZrO_2 Catalyst. *ACS Catal* **2022**, *12* (11), 6325–6333.
(21) Jing, Y.; He, C.; Zhang, N.; Murano, Y.; Toyoshima, R.; Kondoh, H.; Kageyama, Y.; Inomata, H.; Toyao, T.; Shimizu, K. Promotional Effect of Ag on the Catalytic Decomposition of N_2O in the Presence of O_2 over the Al_2O_3-Supported Rh Catalyst. *ACS Catal* **2023**, *13* (19), 12983–12993.
(22) Zhang, N.; He, C.; Jing, Y.; Qian, Y.; Toyao, T.; Shimizu, K. ichi. Enhanced N_2O Decomposition on Rh/ZrO_2 Catalysts through the Promotional Effect of Palladium. *Surfaces and Interfaces* **2024**, *46*, 104120.
(23) Mauvezin, M.; Delahay, G.; Coq, B.; Kieger, S. N_2O Decomposition in the Presence of Ammonia on Faujasite-Supported Metal Catalysts. *Appl. Catal. B.* **1999**, *23*, L79–L82.
(24) Centi, G.; Perathoner, S.; Vazzana, F.; Marella, M.; Tomaselli, M.; Mantegazza, M. Novel Catalysts and Catalytic Technologies for NO_2 Removal from Industrial Emissions Containing O_2, H_2O and SO_2. *Adv Environ Res* **2000**, *4*, 325–338.
(25) Zhang, X.; Shen, Q.; He, C.; Ma, C.; Cheng, J.; Li, L.; Hao, Z. Investigation of Selective Catalytic Reduction of N_2O by NH_3 over an Fe-Mordenite Catalyst: Reaction Mechanism and O_2 Effect. *ACS Catal* **2012**, *2* (4), 512–520.
(26) Wang, A.; Wang, Y.; Walter, E. D.; Kukkadapu, R. K.; Guo, Y.; Lu, G.; Weber, R. S.; Wang, Y.; Peden, C. H. F.; Gao, F. Catalytic N_2O Decomposition and Reduction by NH_3 over Fe/Beta and Fe/SSZ-13 Catalysts. *J Catal* **2018**, *358*, 199–210.
(27) Campa, M. C.; Pietrogiacomi, D.; Scarfiello, C.; Carbone, L. R.; Occhiuzzi, M. CoO_x and FeO_x Supported on ZrO_2 for the Simultaneous Abatement of NOx and N_2O with C_3H_6 in the Presence of O_2. *Appl Catal B* **2019**, *240*, 367–372.
(28) You, Y.; Chen, S.; Li, J.; Zeng, J.; Chang, H.; Ma, L.; Li, J. Low-Temperature Selective Catalytic Reduction of N_2O by CO over Fe-ZSM-5 Catalysts in the Presence of O_2. *J Hazard Mater* **2020**, *383*, 121117.
(29) Cheng, J.; Zheng, D.; Yu, G.; Xu, R.; Dai, C.; Liu, N.; Wang, N.; Chen, B. N_2O Catalytic Decomposition and NH_3-SCR Coupling Reactions over Fe-SSZ-13 Catalyst: Mechanisms and Interactions Unraveling via Experiments and DFT Calculations. *ACS Catal* **2023**, *13* (2), 934–947.
(30) Tian, H.; Xu, R.; Canadell, J. G.; Thompson, R. L.; Winiwarter, W.; Suntharalingam, P.; Davidson, E. A.; Ciais, P.; Jackson, R. B.; Janssens-Maenhout, G.; Prather, M. J.; Regnier, P.; Pan, N.; Pan, S.; Peters, G. P.; Shi, H.; Tubiello, F. N.; Zaehle, S.; Zhou, F.; Arneth, A.; Battaglia, G.; Berthet, S.; Bopp, L.; Bouwman, A. F.; Buitenhuis, E. T.; Chang, J.; Chipperfield, M. P.; Dangal, S. R. S.; Dlugokencky, E.; Elkins, J. W.; Eyre, B. D.; Fu, B.; Hall, B.; Ito, A.; Joos, F.; Krummel, P. B.; Landolfi, A.; Laruelle, G. G.; Lauerwald, R.; Li, W.; Lienert, S.; Maavara, T.; MacLeod, M.; Millet, D. B.; Olin, S.; Patra, P. K.; Prinn, R. G.; Raymond, P. A.; Ruiz, D. J.; van der Werf, G. R.; Vuichard, N.; Wang, J.; Weiss, R. F.; Wells, K. C.; Wilson, C.; Yang, J.; Yao, Y. A Comprehensive Quantification of Global Nitrous Oxide Sources and Sinks. *Nature* **2020**, *586* (7828), 248–256.
(31) Milam-Guerrero, J. A.; Yang, B.; To, D. T.; Myung, N. V. Nitrous Oxide Is No Laughing Matter: A Historical Review of Nitrous Oxide Gas-Sensing Capabilities Highlighting the Need for Further Exploration. *ACS Sensors*. American Chemical Society December 23, 2022, pp 3598–3610.
(32) Kar, S.; Goeppert, A.; Prakash, G. K. S. Integrated CO_2 Capture and Conversion to Formate and Methanol: Connecting Two Threads. *Acc Chem Res* **2019**, *52* (10), 2892–2903.

(33) González-Castaño, M.; Dorneanu, B.; Arellano-García, H. The Reverse Water Gas Shift Reaction: A Process Systems Engineering Perspective. *React Chem Eng* **2021**, *6*, 954–976.
(34) Kosaka, F.; Liu, Y.; Chen, S. Y.; Mochizuki, T.; Takagi, H.; Urakawa, A.; Kuramoto, K. Enhanced Activity of Integrated CO_2 Capture and Reduction to CH_4 under Pressurized Conditions toward Atmospheric CO_2 Utilization. *ACS Sustain Chem Eng* **2021**, *9* (9), 3452–3463.
(35) Li, L.; Wu, Z.; Miyazaki, S.; Toyao, T.; Maeno, Z.; Shimizu, K. Continuous CO_2 Capture and Methanation over Ni-Ca/Al_2O_3 Dual Functional Materials. *RSC Adv* **2023**, *13* (4), 2213–2219.
(36) Li, L.; Miyazaki, S.; Wu, Z.; Toyao, T.; Selyanchyn, R.; Maeno, Z.; Fujikawa, S.; Shimizu, K. Continuous Direct Air Capture and Methanation Using Combined System of Membrane-Based CO_2 Capture and Ni-Ca Based Dual Functional Materials. *Appl Catal B* **2023**, *339*, 123151.
(37) Jing, Y.; Cai, Z.; Liu, C.; Toyao, T.; Maeno, Z.; Asakura, H.; Hiwasa, S.; Nagaoka, S.; Kondoh, H.; Shimizu, K. Promotional Effect of La in the Three-Way Catalysis of La-Loaded Al_2O_3-Supported Pd Catalysts (Pd/La/Al_2O_3). *ACS Catal* **2020**, *10*, 1010–1023.
(38) Kresse, G.; Furthmüller, J. Efficient Iterative Schemes for *Ab Initio* Total-Energy Calculations Using a Plane-Wave Basis Set. *Phys Rev B* **1996**, *54* (16), 11169.
(39) Kresse, G.; Furthmüller, J. Efficiency of Ab-Initio Total Energy Calculations for Metals and Semiconductors Using a Plane-Wave Basis Set. *Comput Mater Sci* **1996**, *6* (1), 15–50.
(40) Takamoto, S.; Shinagawa, C.; Motoki, D.; Nakago, K.; Li, W.; Kurata, I.; Watanabe, T.; Yayama, Y.; Iriguchi, H.; Asano, Y.; Onodera, T.; Ishii, T.; Kudo, T.; Ono, H.; Sawada, R.; Ishitani, R.; Ong, M.; Yamaguchi, T.; Kataoka, T.; Hayashi, A.; Charoenphakdee, N.; Ibuka, T. Towards Universal Neural Network Potential for Material Discovery Applicable to Arbitrary Combination of 45 Elements. *Nat Commun* **2022**, *13* (1), 2991.
(41) Perdew, J. P.; Ruzsinszky, A.; Csonka, G. I.; Vydrov, O. A.; Scuseria, G. E.; Constantin, L. A.; Zhou, X.; Burke, K. Restoring the Density-Gradient Expansion for Exchange in Solids and Surfaces. *Phys Rev Lett* **2008**, *100* (13), 136406.
(42) Blöchl, P. E. Projector Augmented-Wave Method. *Phys Rev B* **1994**, *50* (24), 17953.
(43) Grimme, S.; Ehrlich, S.; Goerigk, L. Effect of the Damping Function in Dispersion Corrected Density Functional Theory. *J Comput Chem* **2011**, *32* (7), 1456–1465.
(44) Rogal, J.; Reuter, K. Ab Initio Atomistic Thermodynamics for Surfaces: A Primer. *Educational Notes RTO-EN-AVT-142* **2007**, *2*, 1–18.
(45) Yasumura, S.; Ide, H.; Ueda, T.; Jing, Y.; Liu, C.; Kon, K.; Toyao, T.; Maeno, Z.; Shimizu, K. Transformation of Bulk Pd to Pd Cations in Small-Pore CHA Zeolites Facilitated by NO. *JACS Au* **2021**, *1* (2), 201–211.
(46) CHASE, M. W. *NIST-JANAF Thermochemical Tables.*; American Chemical Society: Washington, DC, 1998.
(47) Brandle, M.; Sauer, J. Acidity Differences between Inorganic Solids Induced by Their Framework Structure. A Combined Quantum Mechanics/Molecular Mechanics Ab Initio Study on Zeolites. *J Am Chem Soc* **1998**, *120*, 1556–1570.
(48) Grybos, R.; Hafner, J.; Benco, L.; Raybaud, P. Adsorption of NO on Pd-Exchanged Mordenite: Ab Initio DFT Modeling. *J. Phys. Chem. C* **2008**, *112* (32), 12349–12362.
(49) Grundner, S.; Markovits, M. A. C.; Li, G.; Tromp, M.; Pidko, E. A.; Hensen, E. J. M.; Jentys, A.; Sanchez-Sanchez, M.; Lercher, J. A. Single-Site Trinuclear Copper Oxygen Clusters in Mordenite for Selective Conversion of Methane to Methanol. *Nat Commun* **2015**, *6*, 7546.

(50) Xia, H. Monomolecular Dehydration of Ethanol into Ethylene over H-MOR Studied by Density Functional Theory. *ACS Omega* **2020**, *5* (17), 9707–9713.
(51) Miller, T. M.; Grassian, V. H. Environmental Catalysis: Adsorption and Decomposition of Nitrous Oxide on Zirconia. *J. Am. Chem. Soc* **1995**, *117*, 10969–10975.
(52) Pietrogiacomi, D.; Campa, M. C.; Carbone, L. R.; Tuti, S.; Occhiuzzi, M. N_2O Decomposition on CoO_x, CuO_x, FeO_x or MnO_x Supported on ZrO_2: The Effect of Zirconia Doping with Sulfates or K+ on Catalytic Activity. *Appl Catal B* **2016**, *187*, 218–227.
(53) Yue, B.; Lian, X.; Liu, S.; Wu, G.; Xu, J.; Li, L. Efficient Nitrous Oxide Capture by Cationic Forms of FAU and CHA Zeolites. *Chemical Engineering Journal* **2023**, *462*, 142300.
(54) Wang, L.; Liu, J.; Lin, C.; Shang, H.; Yang, J.; Li, L.; Li, J. Effects of Different Alkali Metal Cations in FAU Zeolites on the Separation Performance of CO_2/N_2O. *Chemical Engineering Journal* **2022**, *431*, 134257.
(55) Meloni, E.; Martino, M.; Pierro, M.; Pullumbi, P.; Brandani, F.; Palma, V. MW-Assisted Regeneration of 13X Zeolites after N_2O Adsorption from Concentrated Streams: A Process Intensification. *Energies (Basel)* **2022**, *15* (11), 4119.
(56) James A. Ritter; Armin D. Ebner. US Patent, 11, 007, 473 B2, May 18, 2021.
(57) Wang, L.; Ye, Z.; Lin, C.; Wang, Y.; Li, J.; Yang, J. The Research into N_2O-CO_2 Separation on Na/Ag-Y Zeolite. *Ind Eng Chem Res* **2024**, *63* (26), 11552–11558.
(58) Wang, L.; Lin, C.; Boldog, I.; Yang, J.; Janiak, C.; Li, J. Inverse Adsorption Separation of N_2O/CO_2 in AgZK-5 Zeolite. *Angewandte Chemie - International Edition* **2024**, *63* (4).
(59) Ohlin, L.; Berezovsky, V.; Öberg, S.; Farzaneh, A.; Holmgren, A.; Grahn, M. Effect of Water on the Adsorption of Methane and Carbon Dioxide in Zeolite Na-ZSM-5 Studied Using in Situ ATR-FTIR Spectroscopy. *J. Phys. Chem. C* **2016**, *120* (51), 29144–29152.

Chapter 4

Enhanced N_2O capture and reduction system using Cu/zeolite adsorbent and $Pd/La/Al_2O_3$ catalyst under O_2-CO_2-rich conditions

4.1 Introduction

N_2O is a potent anthropogenic greenhouse gas possessing a global warming potential approximately 310 times higher than that of CO_2. It is also a primary contributor to the stratospheric ozone depletion.[1,2] N_2O emissions are expected to nearly double by 2050, unless effective mitigation strategies are implemented by each country.[3] Various techniques, including thermal, photocatalytic, and electrocatalytic methods, are available for converting N_2O into harmless N_2.[4–10] While photocatalytic and electrocatalytic systems can function at room temperature, these approaches are, however, not implemented in industrial-scale applications.[11,12] Conversely, N_2O can be decomposed through thermal catalysis, by utilizing either direct decomposition ($2N_2O \rightarrow 2N_2 + O_2$)[13–20] or selective catalytic reduction.[21–26] These thermal processes typically require high temperatures (*ca.* T > 300 °C), even for commercial Fe-zeolite catalyst, which is one of the most commonly employed catalytic systems for N_2O decomposition.[16,17,25]

Although a wide variety of catalytic materials have been developed for N_2O decomposition, some of which demonstrate promising low-temperature activity with the T_{50} value (temperature at which 50% of N_2O is degraded) below 200 °C,[27] their activities are significantly reduced in the presence of complex exhaust gas mixtures.[28–41] This presents a major challenge for their application because N_2O is commonly generated as a byproduct in processes including industries that burn biomass, use fossil fuels, or during nitric and adipic acid production.[42] For example, the adipic acid tail gas contains O_2 and CO_2 besides N_2O, indicating the critical need for effective N_2O removal from mixed tail gas.

Adsorption and separation technologies using porous adsorbents have attracted considerable attention owing to their low energy consumption.[43–51] While the separation of N_2O from O_2 can be achieved due to their distinct physical properties,[52] selectively capturing N_2O in the presence of CO_2 remains challenging as N_2O and CO_2 share similar molecular size and physical properties.[53–55] For the separation of N_2O and CO_2, several studies have investigated metal–organic frameworks (MOFs) and Ag exchanged zeolites as selective N_2O adsorbents.[55–57] While these materials have demonstrated promising N_2O/CO_2 separation under mild conditions with high N_2O/CO_2 volume ratios (e.g., v_{N2O}/v_{CO2} = 1:1), studies under conditions with extremely low N_2O/CO_2 volume ratios relevant to industrial applications remain notably lacking. In addition, MOF synthesis is generally complex, and silver is an expensive component. To address high energy consumption during N_2O decomposition and

low efficiency of N_2O/CO_2 separation, it is significant to develop a cost-efficient approach to separate or enrich N_2O for industrial applications.

Integrated capture and conversion systems using dual-functional materials have recently emerged as a promising approach for several chemical transformations, particularly for CO_2 utilization.[58,59] This technique utilizes distinct reactors to selectively adsorb CO_2, and subsequent reduction with H_2, thus circumventing the hindrance typically caused by the presence of inhibitors during reduction.[60–62] In our previous study, inspired by these integrated capture and conversion strategies, an N_2O capture and reduction system was developed using Ca-exchanged zeolite (Ca-zeolite) as an N_2O adsorbent and Pd nanoparticles on La-loaded Al_2O_3 (Pd/La/Al_2O_3) as a reduction catalyst.[52] This process enables the effective capture and reduction of N_2O in the presence of O_2. However, its performance was significantly impeded in the presence of CO_2 with the N_2O capture capacity of Ca-zeolite reduced by over 90%. This highlights the necessity for finding efficient materials capable of environments containing O_2 and CO_2.

In this study, we investigated a series of materials to test N_2O adsorption and found that Cu oxides supported on CHA-type zeolite (Cu/CHA) is an efficient N_2O adsorbent in environments containing both O_2 and CO_2. Using the Cu/CHA adsorbent, we developed an N_2O capture and reduction system that could operate effectively in the presence of O_2 and CO_2 at low temperatures (below 150 °C) for at least 12 h.

4.2 Experimental details

4.2.1 Chemicals and catalyst preparation

All adsorbents, excluding MOFs, were prepared using either impregnation or the ion-exchange method. The following zeolite materials are used for adsorbent preparation: MOR (JRC-Z-HM20(5), Si/Al = 9.1, Tosoh Co.), MFI (HSZ-820NHA, Si/Al = 11.15, Tosoh Co.), CHA (Si/Al ratio = 11.15, Tosoh Co.), BEA (HSZ-920NHA, Si/Al = 8.75, Tosoh Co.), Y (HSZ-372HUA, Si/Al = 15, Tosoh Co.). The samples prepared via the impregnation method were denoted as Metal(X)/Support, with X indicating the metal loading in wt.%. For impregnated zeolite materials, the samples were labeled as Metal(X)/Zeolite(Y), in which “Zeolite” represents the zeolite framework type and Y is the Si/Al ratio of zeolites. A mixture of a specified amount of support and the corresponding aqueous solution of the metal nitrate was added in a 100 mL glass vessel containing an appropriate amount of deionized water and stirred at 200 rpm for 30 min at 50 °C. The mixture was evaporated to dryness at 50 °C, then dried at 110 °C for 1 h and calcined in air at 500 °C for 3 h. For the ion exchange process, 1 g of zeolite powder was mixed with 50 mL of an aqueous solution of the precursor in which the molar amount of the precursor was five times that of Al in the zeolite.[52] The slurry was then heated at 60 °C for 4 h with continuous stirring. The as-prepared sample was recovered by centrifugation at 4000 rpm, washed with distilled water, and subsequently dried at 110 °C for 12 h, followed by calcination at 500 °C for 3 h to obtain ion-exchanged zeolite materials. An La-containing Al_2O_3-supported Pd catalyst ($Pd/La/Al_2O_3$) was prepared using the impregnation method described in our previous study.[63] The Pd and La loadings in $Pd/La/Al_2O_3$ are 1 wt.% and 15 wt.%, respectively.

MOF materials including HKUST-1, UiO-66, ZIF-8, and ZIF-67 were synthesized according to published procedures with slight modifications.[64–67] For HKUST-1, 1,3,5-benzenetricarboxylic acid (250 mg) was dissolved in 40 mL of a 1:1 mixture of ethanol/N,N-dimethylformamide (DMF). In another flask, $Cu(NO_3)_2 \cdot 3H_2O$ (519 mg) was dissolved in 15 mL of water. The two solutions were mixed and stirred for 10 min. Then, the mixture was heated at 373 K for 10 h. After cooling to room temperature, the obtained blue powder was treated with ethanol at 70 °C for 2 h and then dried at 150 °C for 12 h under vacuum. For UiO-66, $ZrCl_4$ (212 mg) and terephthalic acid (220 mg) were dissolved in DMF (40 mL) and stirred for a few minutes at room temperature. The mixture was then placed in a Teflon-lined stainless-steel autoclave and heated in an oven at 393 K for 48 h. After cooling to room temperature, the precipitate was filtered, washed repeatedly with methanol, and dried at room

temperature for 24 h. For ZIF-8, a mixture of 2-methylimidazole (1.32 g), zinc nitrate tetrahydrate ($Zn(NO_3)_2 \cdot 4H_2O$, 0.60 g) and methanol (44 mL) was vigorously stirred at room temperature for 24 h. The generated precipitate was collected by centrifugation, washed repeatedly with methanol and dried at 333 K for 12 h. For ZIF-8, 0.45 g cobalt nitrate hexahydrate was dissolved in 3 mL of deionized (DI) water; then 5.5 g 2-methylimidazole was dissolved in 20 mL of DI water. Those two solutions were mixed and stirred for 6 h at room temperature, then the resulting purple precipitates were collected by centrifuging, washed with water and methanol subsequently for 3 times, and finally vacuum-dried at 80 °C for 24h.

4.2.2 Characterization

X-ray diffraction (XRD) patterns were obtained using a Rigaku MiniFlex II/AP diffractometer with Cu-Kα radiation. High-angle annular dark-field scanning transmission electron microscopy (HAADF-STEM) and energy-dispersive X-ray spectroscopy (EDX) were performed using an FEI Titan G2 microscope. The samples were prepared by dropping an ethanolic solution of the catalyst onto a carbon-supported Mo grid. X-ray fluorescence spectroscopy (EDX-700HS, Shimadzu Corp.) revealed Cu loading amounts for the ion-exchanged Cu-CHA sample. The surface area was measured by N_2 adsorption and determined by the Brunauer–Emmett–Teller (BET) method.

Cu K-edge X-ray absorption spectra (XAS) were recorded in the transmission mode at the BL01B1 beamline with a Si(111) double crystal monochromator (proposal 2024B1749). The powder samples were pelletized into a diameter of 7 mm disk and mounted on an aluminum holder attached to a cryostat. For comparison, the spectra of bulk Cu_2O and CuO were also acquired. All spectra were recorded using the quick-scan XAFS method at 10 K. The XAS results were analyzed using the Athena software ver. 0.9.25, which is included in the Demeter package [68].

Ex situ Electron paramagnetic resonance (EPR) spectra were measured on a EMX plus spectrometer (Bruker Biospin, Rheinstetten Germany), equipped with Super-High-Q resonator (Bruker Biospin) operating at X-band frequencies (~9.8 GHz). The parameters for all EPR measurements were shown as **Table 4.1**. About 20 mg of the calcinated sample were loaded in 5 mm quartz tubes with screw valve (JEOL Ltd.) For the dehydrated samples, the sample in the tubes were heated to 500 °C in a flow of dry synthetic air for 2h to remove water subsequently the valve was closed to avoid rehydration. All Spectra were measured at room temperature. 20 mg of a hydrated Cu-exchanged CHA(Cu wt.% = 0.7) was used as a

reference sample to quantify the EPR detectable Cu copper amount in each sample. The fully hydrated spectrum of low loading ion-exchanged Cu-CHA material is expected to represent the total amount of Cu^{2+} in the zeolite.[68] All the sample possess a very similar height and were placed at the same position in the Resonator to minimize uncertainties.[69]

Table 4.1 EPR parameters for all measurement

Sweep width [mT]	Modulation frequency [kHz]	Modulation amplitude [mT]	Points	Conversion time [ms]	Time constant [ms]	Power attenuation [dB]
200	100	0.4	2048	20	20	24

The intensity of the cw EPR spectrum is proportionally related to the first derivative of the magnetic susceptibility of the sample at a certain temperature and external magnetic field strength. Accordingly, the double integral of the EPR spectrum is a direct measure of the total number of spins in the sample.[70] Note that generally an uncertainty of about 10-15% is assumed by comparing different samples with a reference sample.[69]

In situ infrared (IR) spectra were collected in transmission mode using an FT/IR-4600 (JASCO) unit with a Mercury-Cadmium-Telluride (MCT) detector. A self-supporting disk of the sample (70 mg) was placed in a handmade *in situ* glass cell with CaF_2 windows. For *in situ* IR experiments, N_2O was fed into the cell at 50 °C through a conventional flow reaction system at a total flow rate of 40 mL/min. Before the measurements, the catalysts were pretreated *in situ* under a flow of 20% O_2/He at 500 °C for 30 min. Temperature-programmed desorption of N_2O (N_2O-TPD) was performed using a BELCAT II instrument (MicrotracBEL). After pretreated by 10% O_2/He (30 mL/min) at 500 °C for 30 min, the sample was exposed to 5% N_2O + 5% CO_2 or 5% N_2O in He (30 mL/min) at 50 °C for 30 min, followed by purging with He for 10 min. The sample was heated to 200 °C at a rate of 10 °C/min.

4.2.3 Breakthrough reaction

Breakthrough experiments were carried out at 50 °C under two different gas mixtures: 1500 ppm N_2O + 10% O_2 + 5% CO_2 or 1500 ppm N_2O + 10% O_2 (He balance, 40 mL/min). Prior to the experiments, the samples were pretreated at 500 °C for 30 min with either 10% O_2 + 5% CO_2 or 10% O_2 (He balance, 40 mL/min). The effluent gas composition was monitored using an online IR spectrometer (JASCO FT/IR-4600) with a TGS detector (5 scans with a resolution of 4 cm^{-1}) and a custom-built gas cell (CaF_2 windows).

4.2.4 N_2O capture and reduction

A separate fixed-bed flow system was utilized to continuously perform N_2O capture and reduction experiments (**Scheme 4.1**). Two parallel reactors filled with Cu/CHA(11) zeolite were employed, where one reactor selectively captured N_2O from a mixture of 0.15% N_2O, 10% O_2, 5% CO_2 and 1% H_2O (if applicable) balanced with He, and the other released N_2O under a flow of He by heating the Cu/CHA(11) zeolite from 50 to 150 °C (20 °C/min). The effluent from the N_2O capture reactor was recorded using an online FT-IR spectrometer (JASCO FT/IR-4600) equipped with a TGS detector (5 scans at a resolution of 4 cm^{-1}). The desorbed N_2O was subsequently fed into the N_2O reduction reactor containing a 400 mg $Pd/La/Al_2O_3$ catalyst under a flow of 4% H_2/He (40 mL/min) at 150 °C. The effluent gas of $Pd/La/Al_2O_3$ was monitored using an online IR spectrometer (JASCO FT/IR-4600) equipped with a TGS detector (5 scans at a resolution of 4 cm^{-1}) and a gas chromatography (490 Micro GC, Agilent Technologies).

4.3 Results and discussion

4.3.1 Adsorbent properties

Breakthrough experiments were conducted using a series of materials to determine the optimal sorbent for N_2O adsorption in the presence of O_2 and CO_2 (**Figure 4.1** and **Table 4.2**). These materials included alkali metal-loaded (Li, Na, K, Rb, Cs), alkaline earth metal-loaded (Mg, Ca, Sr, Ba), transition metal-loaded (Cr, Mn, Fe, Co, Ni, Cu, Zn), and lanthanide metal-loaded (Eu, Gd, Tb) samples.

Under conditions where only O_2 was present (without CO_2), the alkaline earth metal-loaded samples demonstrated significant N_2O capture abilities, consistent with previous studies,[43–45] in which Sr-loaded CHA exhibited the highest adsorption capacity. For nearly all materials, the presence of CO_2 significantly reduced the N_2O adsorption capacity, with the time at which the N_2O concentration at the outlet reached 100 ppm (t_{100}) generally below 200 s. However, for Cu(10)/CHA(11), the t_{100} value was 585 s under O_2-only conditions and 443 s under O_2 + CO_2 conditions, indicating only a minor decrease. Thus, Cu(10)/CHA(11) exhibited the highest adsorption capacity among the tested samples. The influence of different supports on N_2O adsorption was also examined. Cu-loaded non-microporous materials such as Al_2O_3, SiO_2, TiO_2, and SiO_2-Al_2O_3 were tested and found to exhibit limited N_2O adsorption capacity. In addition, microporous metal–organic frameworks (MOFs) such as HKUST-1, UiO-66, ZIF-8, and ZIF-67 were evaluated and showed lower N_2O adsorption capacity in the presence of CO_2 compared to most of the metal-loaded zeolites. These results indicate that a well-defined porous structure, specifically a zeolite framework, is essential for effective N_2O adsorption capacity. Cu-loaded zeolites with similar Si/Al ratios around 10 but different framework types (BEA, MOR, MFI, and FER) were investigated. Zeolites with smaller pore sizes of 3-5 Å, such as CHA, ZSM-5, and FER, showed higher N_2O adsorption capacity compared to those with larger pore sizes around 7 Å, such as BEA and MOR. Furthermore, zeolite samples of the same topology (BEA and MFI) with varying Si/Al ratios were tested to evaluate the impact of Al contents. N_2O adsorption was found to be more favorable in Al-rich zeolites, while Al-poor zeolites exhibited significantly lower adsorption capacities. Additional tests in the presence of H_2O confirmed this trend persisted, with Al-rich BEA and MFI zeolites maintaining high N_2O adsorption capacities compared to their Al-poor counterparts. These observations suggest that the high Al content in CHA zeolite likely promotes the formation of efficient Cu species for selective N_2O capture, even in the presence of H_2O. Please note that since CHA-type zeolites with varied Si/Al ratios are not readily

accessible, we instead employed BEA- and MFI-type zeolites for comparison in this study. A Cu-exchanged CHA(11) (Cu-CHA(11)) was prepared using the ion-exchange method. The Cu loading in Cu-CHA(11) was determined to be 2.8 wt.% (Cu/Al = 0.33) using energy-dispersive X-ray fluorescence spectrometry. The N_2O adsorption capacity of Cu-CHA(11) was much lower than that of impregnated Cu(10)/CHA(11), indicating that highly dispersed Cu species are not the primary contributor to N_2O adsorption.

To further understand the impact of O_2, CO_2 and H_2O on the N_2O adsorption ability, which are known as coexisting gases under practical conditions,[46] additional breakthrough experiments were conducted (**Figure 4.2**). The results indicate that O_2 showed negligible effect on the N_2O capture ability of Cu/CHA(11) whereas CO_2 caused a slight decrease. In contrast, the presence of H_2O resulted in significant suppression of N_2O adsorption capacity. These results indicate that the N_2O capture ability of Cu/CHA was notably diminished by H_2O but not by O_2 and CO_2, underscoring the necessity to remove H_2O from the N_2O feed to maintain high performance of Cu/CHA(11).

Having identified a high-performance adsorbent for N_2O adsorption, the optimal Cu loading amount was investigated (**Figure 4.3**). Breakthrough experiments of N_2O in the presence of CO_2 were conducted over Cu/CHA(11) with different loadings. As the Cu loading increased from 1 wt.% to 10 wt.%, an increase in the breakthrough time was observed, whereas a further increase beyond 10 wt.% led to a decrease. This trend indicates that Cu/CHA(11) with 10 wt.% Cu exhibited the highest N_2O capture ability in the presence of CO_2, which was further confirmed through the result of temperature-programmed desorption of N_2O (N_2O-TPD). The quantity of adsorbed N_2O per Cu was determined using the desorbed N_2O amount during N_2O-TPD experiments. The results depicted that Cu(10)/CHA(11) had the largest amount of adsorbed N_2O per Cu, which was determined to be 0.022 N_2O_{ad}/Cu. This finding suggests that the predominant adsorption sites were neither the mononuclear Cu species, which are too small, nor the larger particulate Cu species, but rather moderately aggregated Cu species. It was also confirmed from the N_2O-TPD experiment under the CO_2-free condition that the amount of adsorbed N_2O did not significantly change even in the presence of CO_2.

The *in situ* IR spectra of N_2O adsorbed on Cu/CHA(11) with different loadings (3 wt.%, 10 wt.%, 20 wt.%) are present in **Figure 4.4**. Spectra were recorded after exposure of the samples to 0.15% N_2O at 50 °C for 30 min, followed by purging with He for 10 min. A distinct

absorption band at 2287 cm^{-1}, assigned to N–N stretching vibrations of adsorbed N_2O,[14] was observed on Cu/CHA(11) samples. This shift from the typical gaseous N_2O range (2260-2180 cm^{-1}) suggests the chemisorption of N_2O on adsorbent surface. Although additional weak bands for adsorbed N_2O (e.g., at 2247 and 2231 cm^{-1}) have been reported for Fe-exchanged CHA zeolite system,[14] the overlap with the gas-phase N_2O makes them difficult to resolve. Only Cu(10)/CHA(11) retained a pronounced adsorption band after He purging, indicating its superior N_2O adsorption capacity compared to the other loadings.

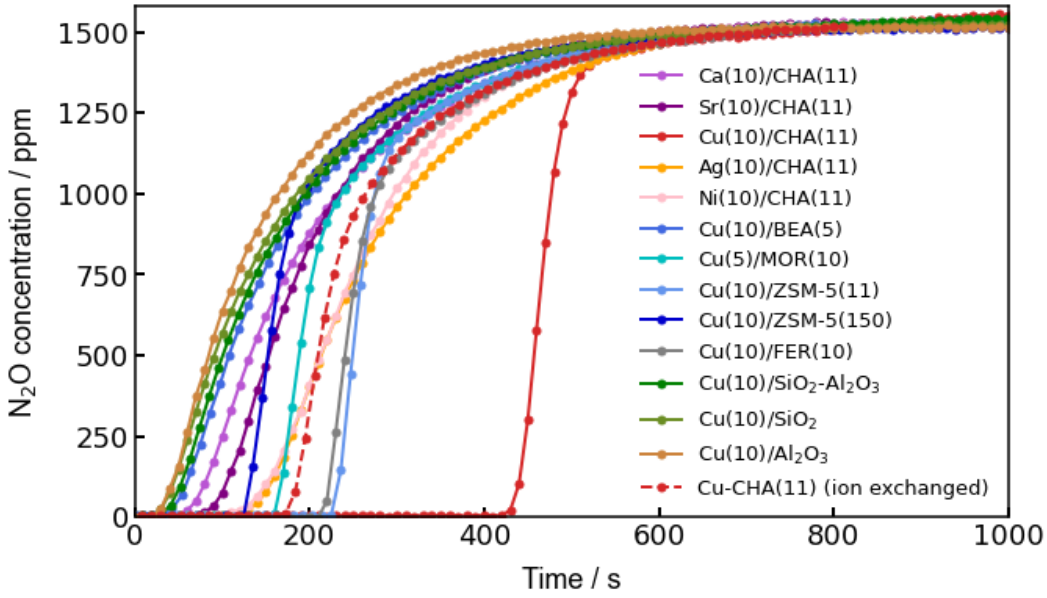

Figure 4.1 Profile of the breakthrough experiments over various materials under a flow of 1500 ppm N_2O + 10% O_2 + 5% CO_2 at 50 °C, total flow rate = 40 mL/min, He balance. Weight of adsorbents: 150 mg. The feed gases were introduced to the adsorbents from 0 s.

Table 4.2 Results of the breakthrough experiments over zeolite materials under a flow of 1500 ppm N_2O + 10% O_2 + 5% CO_2 or 1500 ppm N_2O + 10% O_2 at 50 °C, total flow rate = 40 mL/min, He balance. Weight of adsorbents: 150 mg. The feed gases were introduced to adsorbents from 0 s.

Adsorbent	t_{100} (s)	
	(i) $N_2O + O_2 + CO_2$	(ii) $N_2O + O_2$
Li(10)/CHA(11)	21	53
Na(10)/CHA(11)	30	48
Mg(10)/CHA(11)	77	528
K(10)/CHA(11)	27	77
Ca(10)/CHA(11)	90	1133
Cr(2)/CHA(11)	70	166
Cr(10)/CHA(11)	69	164
Mn(2)/CHA(11)	102	623
Mn(10)/CHA(11)	114	771
Fe(2)/CHA(11)	75	202
Fe(10)/CHA(11)	90	191
Co(10)/CHA(11)	150	722
Ni(10)/CHA(11)	164	701
Cu(2)/CHA(11)	141	225
Cu(10)/CHA(11)	443	585
Zn(2)/CHA(11)	76	692
Rb(10)/CHA(11)	107	130
Sr(10)/CHA(11)	114	1626
Ag(10)/CHA(11)	167	421
Cs(10)/CHA(11)	79	206
Ba(10)/CHA(11)	106	1076
Eu(2)/CHA(11)	126	298
Eu(10)/CHA(11)	71	360
Gd(2)/CHA(11)	48	345
Gd(10)/CHA(11)	72	307
Tb(2)/CHA(11)	52	400
Au(2)/CHA(11)	96	175
Au(10)/CHA(11)	96	193
Cu(10)/BEA(5)	134	-
Cu(10)/BEA(20)	133	-
Cu(10)/BEA(255)	107	-
Cu(5)/MOR(10)	178	-
Cu(10)/FER(10)	226	-
Cu(10)/ZSM-5(11)	242	-
Cu(10)/ZSM-5(45)	229	-
Cu(10)/ZSM-5(150)	141	-
Cu(10)/SiO_2-Al_2O_3	78	-
Cu(10)/SiO_2	50	-
Cu(10)/Al_2O_3	51	-
Cu(10)/TiO_2	50	-
HKUST-1	54	-
ZIF-8	55	-
ZIF-67	67	-
UiO-66	24	-
Cu-CHA(11) (ion exchanged)	98	-

[a] In the breakthrough experiments, the time when the N_2O concentration at the outlet reaches 100 ppm (t_{100}) is utilized to determine the N_2O adsorption capacity of various materials

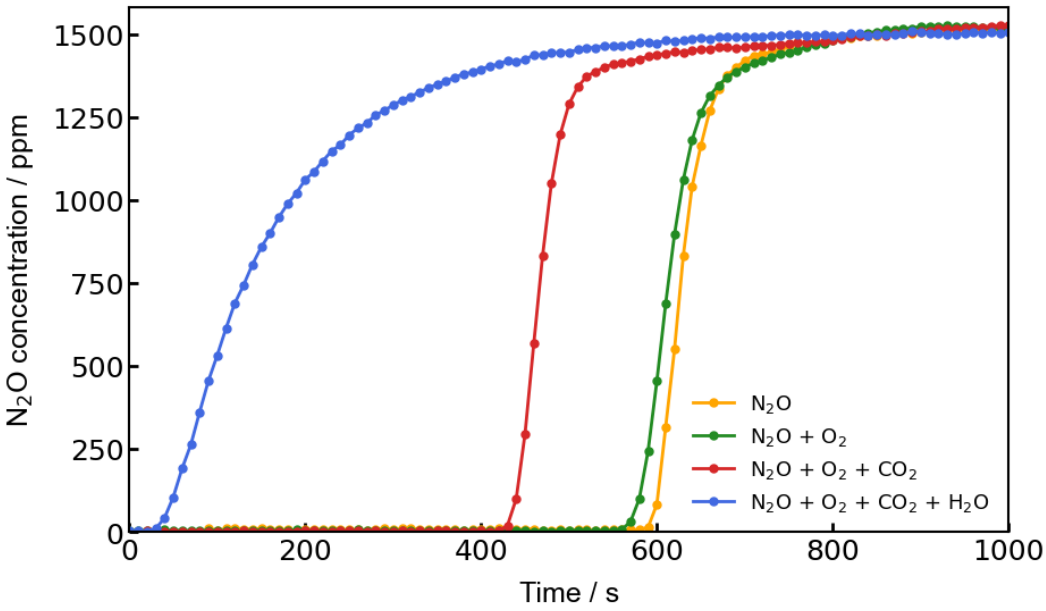

Figure 4.2 Profile of the breakthrough experiments over Cu(10)/CHA(11) zeolite under a flow of (a) 1500 ppm N_2O, (b) 1500 ppm N_2O + 10% O_2, and (c) 1500 ppm N_2O+ 10% O_2 + 5% CO_2, (d) 1500 ppm N_2O+ 10% O_2 + 5% CO_2 + 1% H_2O at 50 °C, total flow rate = 40 mL/min, He balance. Weight of adsorbents: 150 mg. The feed gases were introduced to adsorbents from 0 s.

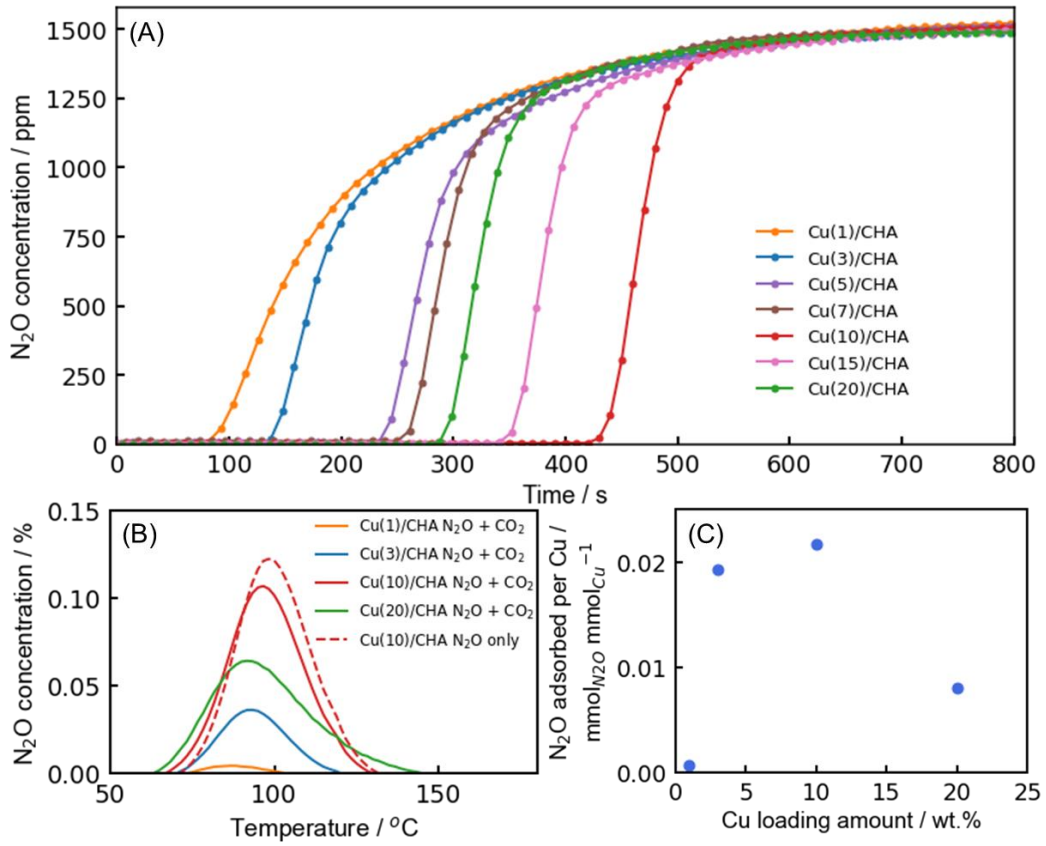

Figure 4.3 (A) Breakthrough curves of Cu/CHA(11) zeolites with various loadings under a flow of 1500 ppm N_2O + 10% O_2 + 5% CO_2 at 50 °C, total flow rate = 40 mL/min, He balance. Weight of adsorbents: 150 mg. The feed gases were introduced to adsorbents from 0 s. (B) N_2O-TPD profiles over different loading Cu/CHA(11) zeolites after exposure to 5% N_2O + 5% CO_2/He at 50 °C for 30 min followed by a He purge for 10 min. The sample was heated from 50 to 200 °C at a rate of 10 °C/min. N_2O-TPD profile over Cu(10)/CHA(11) after exposure to 5% N_2O/He was used as a reference. (C) The amount of N_2O adsorbed per Cu, calculated from N_2O-TPD results, is plotted versus the Cu loading.

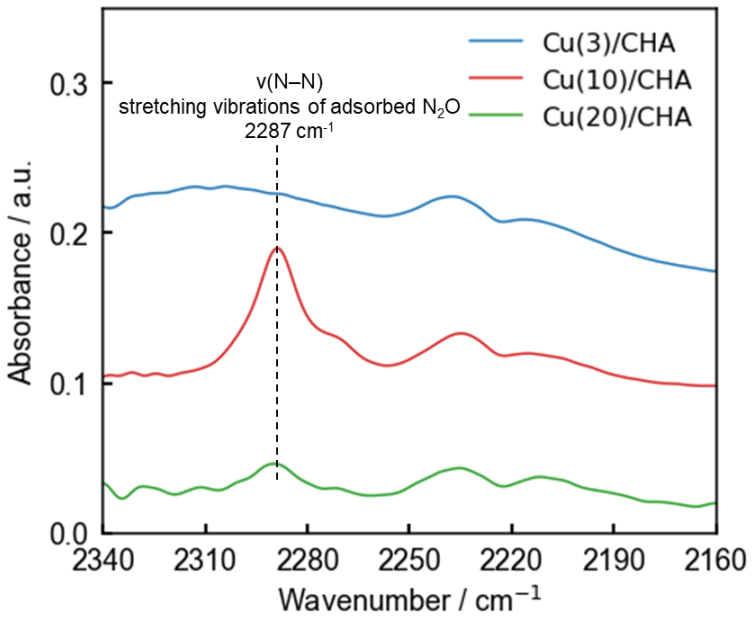

Figure 4.4 *In situ* IR spectra of Cu/CHA(11) zeolites with different loadings after the introduction of 0.15% N_2O at 50 °C for 30 min, followed by a He purge for 10 min. Before N_2O introduction, each Cu/CHA(11) pellet was pretreated at 500 °C for 30 min under a flow of 20% O_2/He and then cooled to 50 °C. followed by a 10-minute He purge. Weight of Cu/CHA(11) pellets: 70 mg, total flow rate: 40 mL/min.

4.3.2 Characterization of Cu/CHA(11)

Figure 4.5 shows the XRD patterns of Cu/CHA(11) with different loadings, using CHA(11) as a reference. The XRD patterns of Cu(10)/CHA(11), Cu(15)/CHA(11), and Cu(20)/CHA(11) exhibit characteristic peaks at 35.5°, 38.7°, 48.6°, and 58.3°, respectively, corresponding to monoclinic CuO.[71–73] In contrast, the Cu(1)/CHA(11), Cu(3)/CHA(11), and Cu(5)/CHA(11) specimens exhibited diffraction peaks corresponding only to the CHA(11) zeolite, with no diffraction peaks attributed to CuO species. This suggested that at low Cu loadings, the Cu species were highly dispersed, whereas at relatively high Cu loadings, they formed crystalline CuO. STEM and EDX mapping analyses (**Figure 4.6**) were performed for Cu(10)/CHA(11). Nanoparticles with a mean diameter of 2.9 nm were observed, confirming the presence of CuO nanoparticles on CHA(11). We also performed N_2 adsorption experiments for these Cu/CHA(11) samples. The BET specific surface areas were calculated to be 715, 665, 551, and 468 m^2/g for CHA(11), Cu(3)/CHA(11), Cu(10)/CHA(11), and Cu(20)/CHA(11), respectively. This result indicates that although the BET surface area decreases with increasing Cu loading, the microporous structure originating from the CHA zeolite remains largely preserved even at higher Cu loadings. This observation is consistent with the results from XRD.

Although X-ray absorption spectroscopy (XAS) effectively elucidates the structure and electronic states of elements, the quality of data can suffer from thermal disorder within the copper species.[74] To obtain high-resolution spectra, Cu K-edge XANES and Fourier transform (FT) of k^3-weighted EXAFS spectra of the Cu/CHA(11) zeolites with various copper loadings (3 wt. %, 10 wt.%, 20 wt.%) were investigated at cryogenic temperatures (**Figure 4.7**). XANES enables the determination of the oxidation state of Cu in zeolites and provides insights into the local symmetry of the corresponding species.[75] The absorption edge positions of the XANES spectra of Cu(3)/CHA(11), Cu(10)/CHA(11), and Cu(20)/CHA(11) were similar to those of bulk CuO, suggesting that the Cu species predominantly existed as Cu^{2+}. The presence of the dipole-forbidden pre-edge peak, mostly deriving from 1s → 3d transition (8978 eV) is another confirmation of the largely dominant presence of Cu^{2+}. [74,76] We also observed a decrease in the intensity of a shoulder peak at 8986 eV and an increase in the intensity of the white line peak at 8999 eV with decreasing Cu loadings, indicating geometric differences in the Cu^{2+} species in Cu/CHA(11) with different loadings.

The FT-EXAFS data for Cu(3)/CHA(11), Cu(10)/CHA(11), and Cu(20)/CHA(11) are provided along with the bulk CuO as a reference. All samples had distinct peaks for both Cu–O and Cu–O–Cu(Si/Al) contributions. **Table 4.3** presents the curve-fitting analysis results for the EXAFS data. Cu(3)/CHA(11), Cu(10)/CHA(11), and Cu(20)/CHA(11) indicated the same coordination numbers of 4.3 for Cu–O path and coordination numbers of 0.3, 1.4 and 1.7 for Cu–O–Cu(Si/Al) paths at about 2.9 Å, respectively. For Cu–O–Cu(Si/Al) paths at about 3.4 Å, Cu(10)/CHA(11) and Cu(20)/CHA(11) indicated the coordination numbers of 0.8 and 2.8, respectively, whereas Cu(3)/CHA(11) showed no Cu–O–Cu(Si/Al) contribution at 3.4 Å, revealing its highly dispersed nature. The decreasing second-shell coordination number for Cu–O–Cu(Si/Al) paths suggests that the average particle size of CuO decreases with decreasing Cu loadings, which is consistent with the XRD results.

These results indicate that the structure and dispersion of Cu species vary with the Cu loadings which are closely related to their N_2O adsorption performance. Specifically, Cu(10)/CHA(11), with moderately aggregated CuO nanoparticles and retained microporosity, exhibited the highest N_2O adsorption capacity. In contrast, low Cu loadings with highly dispersed Cu species and high loadings with more aggregated particles led to inferior N_2O adsorption. Therefore, the formation of accessible CuO nanoparticles in CHA framework appears crucial for optimizing selective N_2O capture.

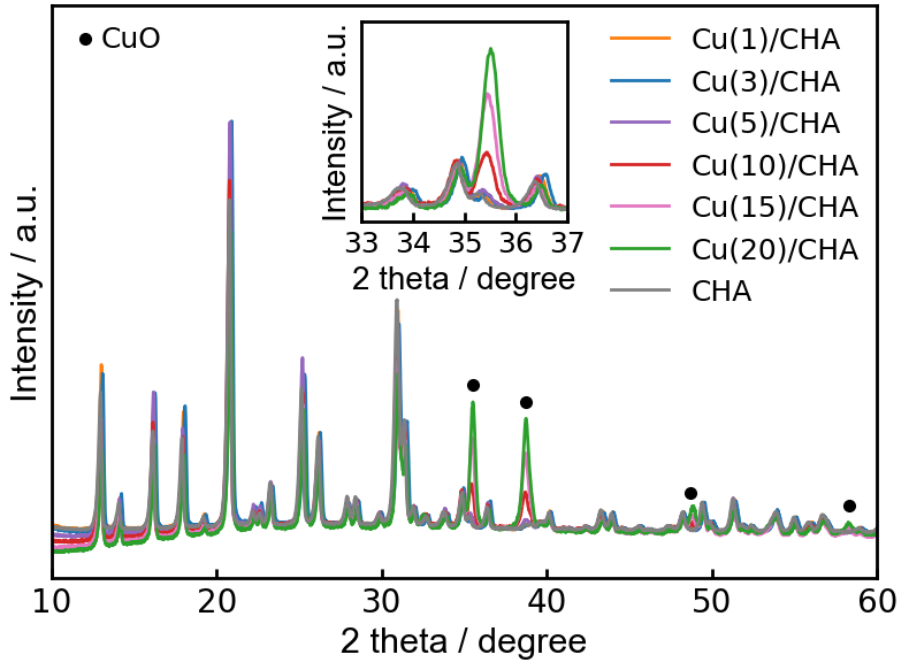

Figure 4.5 XRD patterns of CHA(11) and Cu/CHA(11) zeolites with different Cu loadings

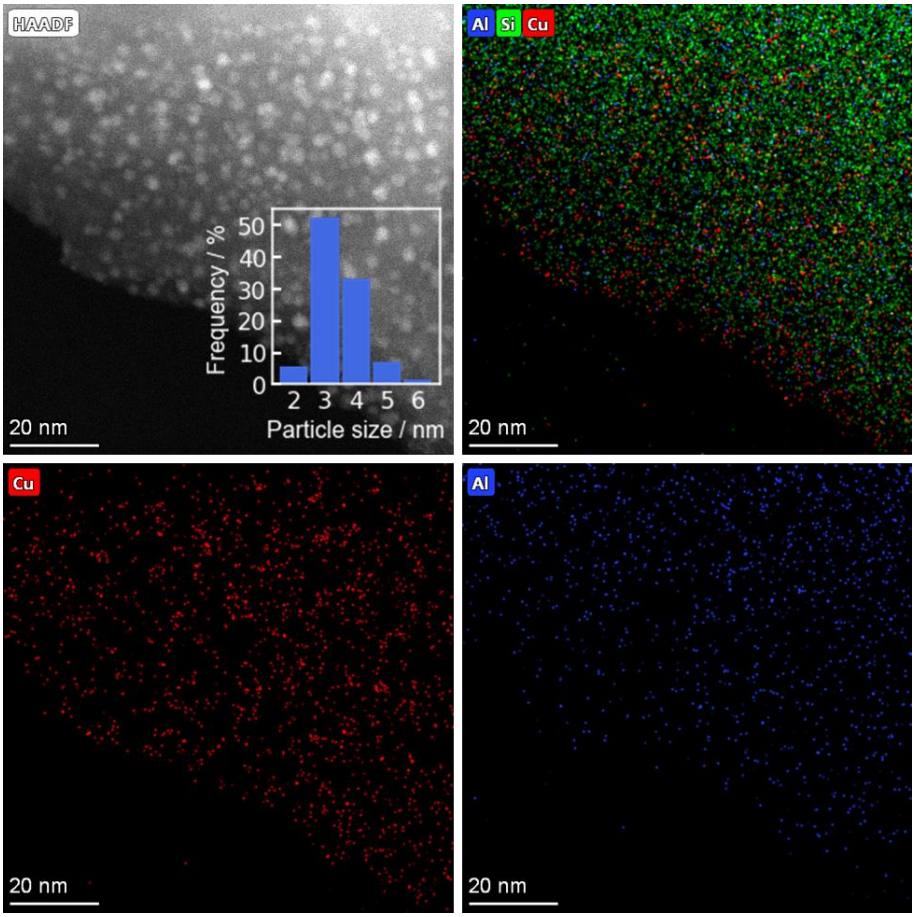

Figure 4.6 HAADF-STEM image and the corresponding EDX mapping images for Cu(10)/CHA(11).

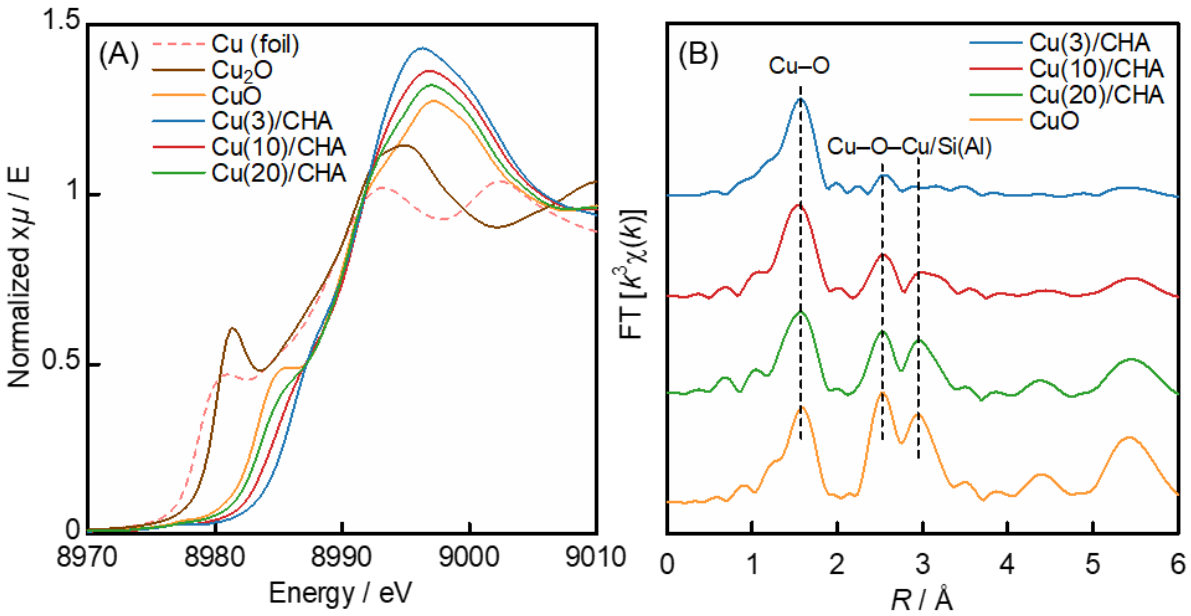

Figure 4.7 (A) Cu K-edge XANES and (B) Fourier transform of k^3-weighted EXAFS spectra of Cu/CHA(11) zeolites with various Cu loadings at 10 K. For reference samples, spectra for Cu_2O and CuO were recorded at 10 K, while that for Cu foil was recorded at room temperature.

Table 4.3 Curve-fitting analysis of the Cu/CHA(11) zeolites having various Cu loading amount.

Sample	Shell	CN [a]	*R* (Å) [b]	σ^2 (Å^2) [c]	R_f (%) [d]
CuO	Cu–O	4	1.94	0.003	1.4
	Cu–O–Cu	2.1	2.88	0.001	
	Cu–O–Cu	4.3	3.40	0.004	
Cu(20)/CHA(11)	Cu–O	4.3	1.94	0.004	1.8
	Cu–O–Cu(Al/Si)	1.7	2.88	0.003	
	Cu–O–Cu	2.8	3.40	0.003	
Cu(10)/CHA(11)	Cu–O	4.3	1.94	0.004	1.3
	Cu–O–Cu(Al/Si)	1.4	2.90	0.005	
	Cu–O–Cu	0.8	3.39	0.003	
Cu(3)/CHA(11)	Cu–O	4.3	1.94	0.003	0.3
	Cu–O–Cu(Al/Si)	0.3	2.91	0.001	

[a] Coordination number. [b] Bond distance. [c] Debye-Waller factor. [d] Residual factor.

To gain further insight into Cu speciation in different Cu/CHA(11) materials, *ex situ* continuous-wave (CW) EPR experiments were performed on dehydrated and hydrated zeolites (**Figure 4.8A**). Monomeric Cu^{2+} (d^9) species exhibit a characteristic EPR signal with a hyperfine quartet owing to the interaction with the Cu nucleus (I = 3/2). In contrast, dimeric species, Cu_xO_y clusters, and nanoparticles are typically undetectable under standard EPR conditions.[77]

The CW EPR spectra of the hydrated zeolites were dominated by an isotropic contribution originating from fully hydrated Cu^{2+} complexes centered at approximately 3200 G (g = 2.1).[68] The double integral of the Cu(1)/CHA(11) spectrum was difficult to assess due to a broad underlying feature. However, for the Cu(3)/CHA(11) sample, the measured

intensity corresponded well with the expected 3 wt.% Cu content (**Table 4.4**). As the Cu content increased, the observed Cu EPR intensity decreased, presumably because of the increased Cu–Cu interactions, which render Cu species EPR-silent or broaden their signals beyond detection.[77] This makes it difficult to quantify monomeric Cu^{2+} species in hydrated samples with high Cu loadings.

Dehydration leads to the loss of water ligands, and the CW EPR spectra of the dehydrated samples revealed two distinct species with g_{II} values of 2.328 and 2.37 (**Figure 4.9**). The first is indicative of isolated Cu^{2+} species in the 6MR of the zeolite framework, while the second likely originates from Cu^{2+} species coordinated to both the framework and residual H_2O molecules, suggesting incomplete dehydration.[78] Quantifying the Cu(1)/CHA(11) intensity is challenging (vide supra). The Cu(3)/CHA(11) sample exhibited approximately 50% isolated monomeric Cu^{2+} species, which is in good agreement with previous studies on dehydrated samples near the full exchange limit.[79,80] The remaining Cu^{2+} species likely formed dimers, given that their monomeric precursors were observed in the hydrated sample. The Cu(10)/CHA(11) and Cu(20)/CHA(11) samples displayed a similar amount of monomeric Cu^{2+} centers, suggesting that the majority of Cu in these materials was present as Cu_xO_y clusters and/or nanoparticles (**Figure 4.8B**). Considering that the trend of monomeric Cu^{2+} amount does not correspond to that of the adsorbed N_2O as the Cu loading increases, the EPR spectra indicate that the monomeric Cu^{2+} center is not the primary adsorption site for N_2O. This finding is in line with the results from the N_2O-TPD measurements. At this stage, the precise nature of the N_2O adsorption sites remains unclear. However, we found that Cu species should be neither too small (e.g., mononuclear species), nor too large to be effective.

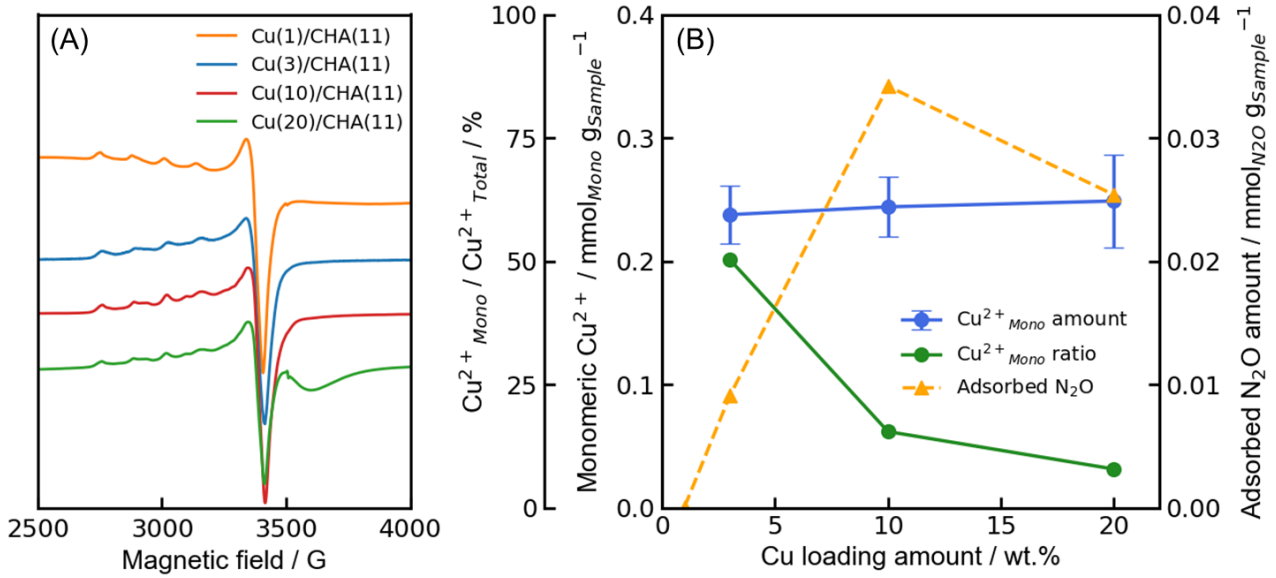

Figure 4.8 (A) *Ex situ* EPR spectra of dehydrated Cu/CHA(11) zeolites with various Cu loadings. (B) Effect of Cu loadings on EPR-active monomeric Cu^{2+} amount, its ratio and the adsorbed N_2O amount integrated from N_2O-TPD results.

Table 4.4 Sample overview with the columns corresponding to the Cu content introduced during preparation; Monomeric Cu^{2+} observed by EPR in the dehydrated samples; Cu^{2+} species observed by EPR in the hydrated samples.

Sample	Cu content(wt.%)	Monomeric Cu^{2+} observed in the dehydrated samples (wt.%)	Cu^{2+} species observed in the hydrated samples (wt.%)
Cu-CHA(6.5)	0.7	-	0.7
Cu(3)/CHA(11)	3	1.51	3.2
Cu(10)/CHA(11)	10	1.55	1.8
Cu(20)/CHA(11)	20	1.58	0.9

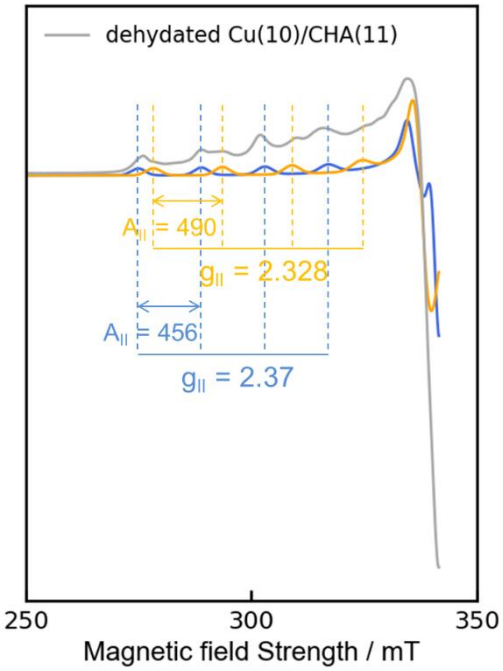

Figure 4.9 The simulation spectra for two monomeric Cu^{2+} species in a dehydrated Cu/CHA sample. All cw EPR simulations were performed with the MATLAB toolbox Easyspin.

4.3.3 N_2O capture and reduction

To assess the stability and regeneration capability of Cu(10)/CHA(11) under practical conditions, we developed a continuous N_2O capture and reduction system. This system is capable of selectively capturing N_2O in the presence of CO_2 and O_2 and reducing it to N_2 at low temperatures (**Scheme 4.1**).[52] The system comprised two parallel reactors filled with 2.5 g of Cu(10)/CHA(11) for alternating N_2O capture and release. Initially, one reactor was fed with a mixture of 1500 ppm N_2O + 10% O_2 + 5% CO_2 for 40 min. Subsequently, the feed was switched to the other containing the same adsorbent. The other reactor released N_2O under a flow of He (40 mL/min) by heating the Cu/CHA(11) zeolite to 150 °C (20 °C/min). The captured N_2O was released by heating Cu(10)/CHA(11) to 150 °C at a heating rate of 20 °C/min, and then cooling it back to 50 °C. The effluent gas for N_2O capture was analyzed using IR spectroscopy. The liberated N_2O was then directed to a downstream section housing the Pd/La/Al_2O_3 catalyst, which was maintained at 150 °C throughout the process, along with a 4% H_2 flow. The composition of the effluent gas from the reactor equipped with Pd/La/Al_2O_3 was monitored using IR spectroscopy and gas chromatography.

Figure 4.10 shows the performance of the continuous N_2O capture and reduction system. During the heating of Cu(10)/CHA(11) from 50 to 150 °C, the formation of N_2 was observed with a maximum concentration of ~20,000 ppm. Despite fluctuations in N_2 concentrations during the experiment, the amount of N_2 released remained consistent with almost no N_2O emissions, demonstrating effective reduction to N_2 by the Pd/La/Al_2O_3 catalyst. Furthermore, only negligible amounts of N_2O were detected using IR spectroscopy, indicating high stability and regeneration capability of Cu(10)/CHA(11). Notably, although a portion of CO_2 was adsorbed and subsequently desorbed during this process, no CO or CH_4 was detected in the effluent gas, indicating that no detrimental byproducts were produced. These results revealed that the continuous N_2O capture and reduction system maintained its N_2O capture capacity and subsequent reduction ability for at least 12 h (9 cycles) in the presence of CO_2 and O_2.

To further evaluate the applicability of this system under realistic exhaust conditions, additional cyclic experiments were conducted in the presence of H_2O, along with O_2 and CO_2 (**Figure 4.11**). Although the N_2O adsorption capacity of Cu(10)/CHA(11) decreased under H_2O-containing conditions, our N_2O capture and reduction system maintained effective operation for at least 12 h without noticeable N_2O slip. The stability can be achieved through periodic regeneration of the Cu/CHA adsorbent by calcination at 500 °C under a flow of 10%

O_2/He, which would remove accumulated water on the adsorbent. These results confirm that the system can operate under an O_2-CO_2-H_2O-containing environment, while highlighting the need for the future development of more water-tolerant adsorbents to further enhance long-term performance and enable more economical and robust operation.

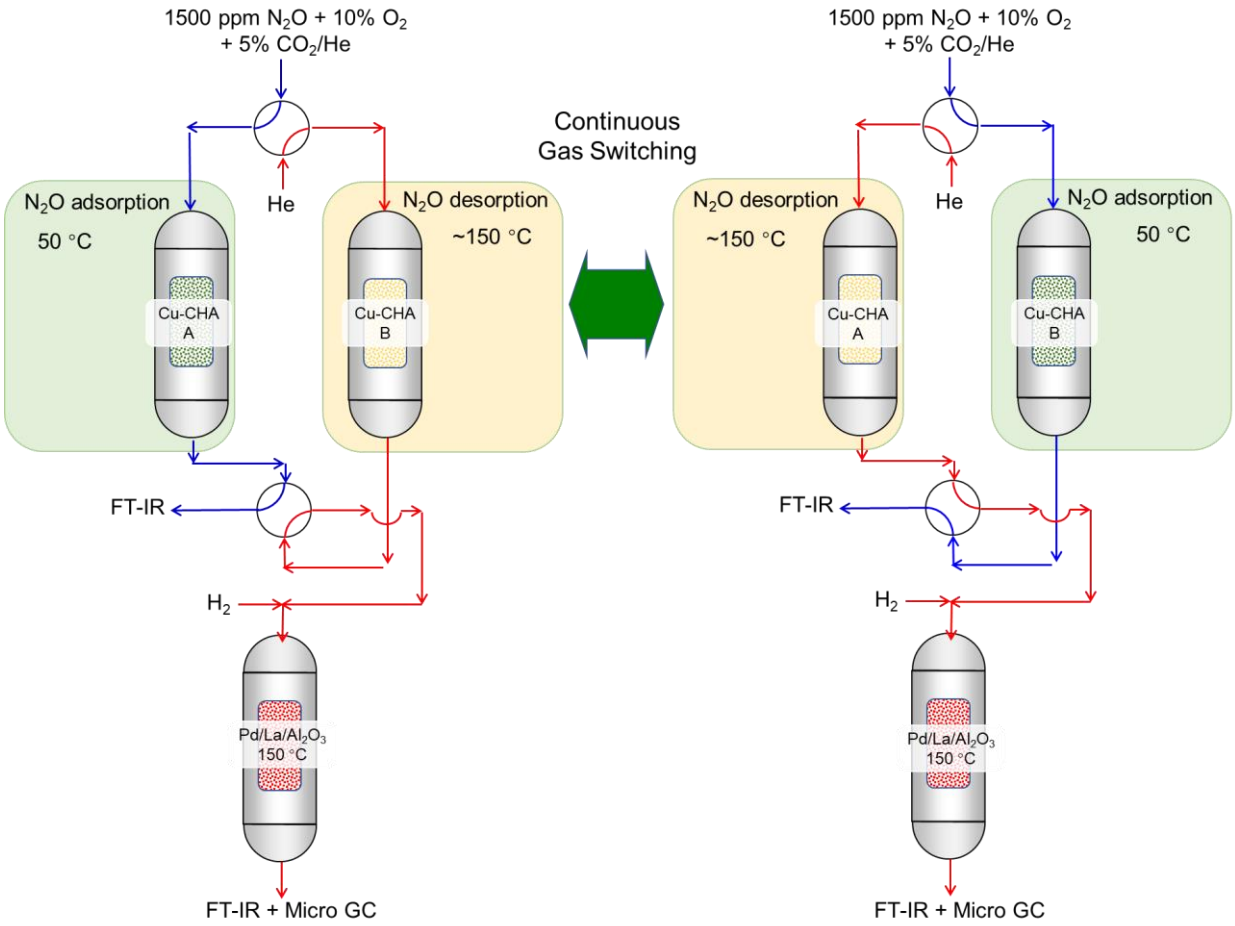

Scheme 4.1. Scheme of the continuous N_2O capture and reduction system using Cu(10)/CHA(11) zeolite as the N_2O capture adsorbent and Pd/La/Al_2O_3 as the reduction catalyst. The temperature of Cu(10)/CHA(11) for N_2O capture was set at 50 °C, whereas the temperature was increased from 50 to 150 °C at a rate of 20 °C/min during the desorption phase. The downstream Pd/La/Al_2O_3 section was maintained at 150 °C throughout the process. Gas composition: 1500 ppm N_2O + 10% O_2 + 5% CO_2 for N_2O adsorption and 4% H_2/He for N_2O reduction. The gas feed was switched every 40 min.

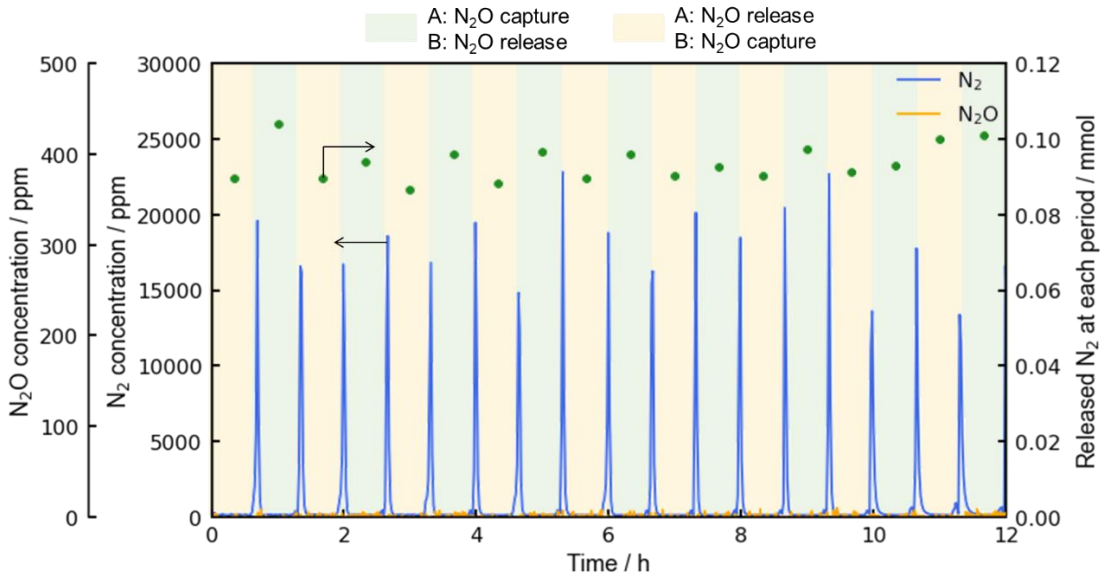

Figure 4.10 Performance of the Cu/CHA(11)-Pd/La/Al_2O_3 continuous N_2O capture and reduction system. Gas composition: 1500 ppm N_2O + 10% O_2 + 5% CO_2 for N_2O adsorption and 4% H_2/He for N_2O reduction. Total flow rate: 40 mL/min. The gas feed was switched every 40 min (1 period). Adsorbent amount in each N_2O capture reactor: 2.5 g. The N_2 and N_2O concentrations detected throughout the process are indicated by blue and orange lines, respectively. The amount of N_2 released during each period is plotted as green dots.

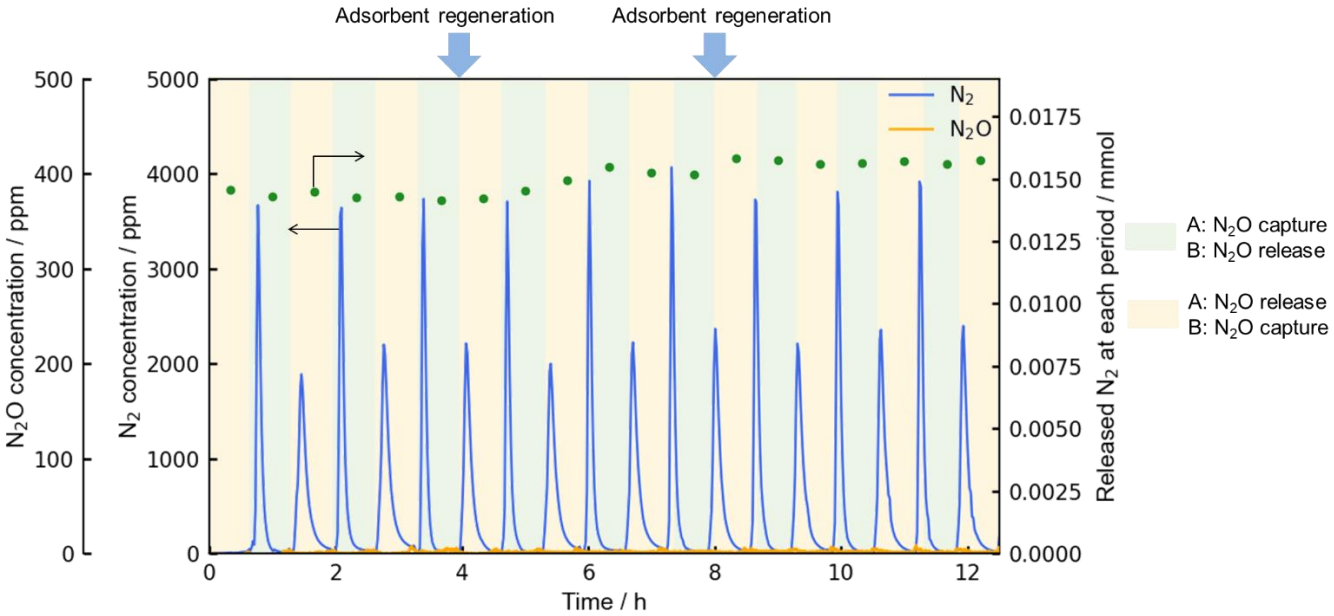

Figure 4.11 Performance of the Cu/CHA(11)-Pd/La/Al_2O_3 continuous N_2O capture and reduction system in the presence of H_2O. Gas composition: 500 ppm N_2O + 10% O_2 + 5% CO_2 + 1% H_2O for N_2O adsorption and 4% H_2/He for N_2O reduction. Total flow rate: 20 mL/min. The gas feed was switched every 40 min (1 period). Adsorbent amount in each N_2O capture reactor: 8 g. The Cu/CHA adsorbents were regenerated every 4 hours through calcination at 500 °C under a flow of 10% O_2/He. The N_2 and N_2O concentrations detected throughout the process are indicated by blue and orange lines, respectively. The amount of N_2 released during each period is plotted as green dots.

4.4 Conclusion

Given the significant global warming potential of N_2O and its rapidly increasing emissions, the development of effective post-treatment technologies for N_2O elimination is crucial. The challenge of controlling N_2O emissions from combustion and industrial sources is compounded by the presence of co-existing gases such as O_2 and CO_2. In this study, a series of materials were prepared, and their N_2O capture capacities in the presence of O_2 and CO_2 were estimated. We found that the CHA-type zeolite loaded with 10 wt.% Cu (Cu(10)/CHA(11)) was particularly effective. Utilizing Cu(10)/CHA(11) as an adsorbent and Pd nanoparticles supported on La-doped Al_2O_3 (Pd/La/Al_2O_3) as a reduction catalyst, we developed a two-step system for capturing and reducing N_2O. This system reliably maintained its N_2O adsorption and reduction performance for at least 12 h, operating continuously through the temperature fluctuations between 50 and 150 °C. Notably, the nature of the active Cu species contributed to the N_2O adsorption in Cu(10)/CHA(11) was also investigated. We found that Cu species should be neither too small nor too large to be effective. CHA zeolites are essential for the formation of effective adsorption sites.

4.5 References

(1) Ravishankara, A. R.; Daniel, J. S.; Portmann, R. W. Nitrous Oxide (N_2O): The Dominant Ozone-Depleting Substance Emitted in the 21st Century. *Science (1979)* **2009**, *326* (5949), 123–125.

(2) Li, L.; Xu, J.; Hu, J.; Han, J. Reducing Nitrous Oxide Emissions to Mitigate Climate Change and Protect the Ozone Layer. *Environ. Sci. Technol.* **2014**, *48* (9), 5290–5297.

(3) Konsolakis, M. Recent Advances on Nitrous Oxide (N_2O) Decomposition over Non-Noble-Metal Oxide Catalysts: Catalytic Performance, Mechanistic Considerations, and Surface Chemistry Aspects. *ACS Catal* **2015**, *5*, 6397–6421.

(4) Kapteijn, F.; Rodriguez-Mirasol, J.; Moulijn, J. A. Heterogeneous Catalytic Decomposition of Nitrous Oxide. *Appl Catal B* **1996**, *9*, 25–64.

(5) Kudo, A.; Mine, A. Electrocatalytic Reduction of Nitrous Oxide on Metal and Oxide Electrodes in Aqueous Solution. *Appl Surf Sci* **1997**, *121/122*, 538–542.

(6) Jabłońska, M.; Palkovits, R. Nitrogen Oxide Removal over Hydrotalcite-Derived Mixed Metal Oxides. *Catal. Sci. Technol.* **2016**, *6*, 49–72.

(7) Jabłońska, M.; Arán, M. A.; Beale, A. M.; Delahay, G.; Petitto, C.; Nocuń, M.; Palkovits, R. Understanding the Origins of N_2O Decomposition Activity in Mn(Fe)CoAlO_x Hydrotalcite Derived Mixed Metal Oxides. *Appl Catal B* **2019**, *243*, 66–75.

(8) Ko, B. H.; Hasa, B.; Shin, H.; Zhao, Y.; Jiao, F. Electrochemical Reduction of Gaseous Nitrogen Oxides on Transition Metals at Ambient Conditions. *J Am Chem Soc* **2022**, *144* (3), 1258–1266.

(9) Kim, K.; Byun, J.; Kim, H.; Lee, K. S.; Lee, H. S.; Kim, J.; Hyeon, T.; Kim, J. J.; Han, J. W. Systematic Approach to Designing a Highly Efficient Core–Shell Electrocatalyst for N_2O Reduction. *ACS Catal* **2021**, *11* (24), 15089–15097.

(10) M. L. Ovcharov, V. M. G. Photocatalytic Conversion of Nitrogen Oxides: Current State and Perspectives: A Review. *Theor. Exp. Chem.* **2021**, *57*, 30–63.

(11) Wu, X.; Du, J.; Gao, Y.; Wang, H.; Zhang, C.; Zhang, R.; He, H.; Lu, G.; Wu, Z. Progress and Challenges in Nitrous Oxide Decomposition and Valorization. *Chem. Soc. Rev.* **2024**, *53* (16), 8379–8423.

(12) Xue, T.; Li, J.; Chen, L.; Li, K.; Hua, Y.; Yang, Y.; Dong, F. Photocatalytic NO_x Removal and Recovery: Progress, Challenges and Future Perspectives. *Chem. Sci.* Royal Society of Chemistry May 20, 2024, pp 9026–9046.

(13) Satsuma, A.; Maeshima, H.; Watanabe, K.; Suzuki, K.; Hattori, T. Effects of Methane and Oxygen on Decomposition of Nitrous Oxide over Metal Oxide Catalysts. *Catal. Today* **2000**, *63*.

(14) Lin, F.; Andana, T.; Wu, Y.; Szanyi, J.; Wang, Y.; Gao, F. Catalytic Site Requirements for N_2O Decomposition on Cu-, Co-, and Fe-SSZ-13 Zeolites. *J. Catal.* **2021**, *401*, 70–80.

(15) Bols, M. L.; Snyder, B. E. R.; Rhoda, H. M.; Cnudde, P.; Fayad, G.; Schoonheydt, R. A.; Van Speybroeck, V.; Solomon, E. I.; Sels, B. F. Coordination and Activation of Nitrous Oxide by Iron Zeolites. *Nat. Catal.* **2021**, *4* (4), 332–340.

(16) Buttignol, F.; Rentsch, D.; Alxneit, I.; Garbujo, A.; Biasi, P.; Kröcher, O.; Ferri, D. Aging of Industrial Fe-Zeolite Based Catalysts for Nitrous Oxide Abatement in Nitric Acid Production Plants. *Catal. Sci. Technol.* **2022**, *12* (24), 7308–7321.

(17) Buttignol, F.; Fischer, J. W. A.; Clark, A. H.; Elsener, M.; Garbujo, A.; Biasi, P.; Czekaj, I.; Nachtegaal, M.; Jeschke, G.; Kröcher, O.; Ferri, D. Iron-Catalysed Cooperative Redox Mechanism for the Simultaneous Conversion of Nitrous Oxide and Nitric Oxide. *Nat. Catal.* **2024**, *7* (3), 1305.

(18) Long, Y.; Zhu, X.; Gao, C.; Si, W.; Li, J.; Peng, Y. Modulation of Co Spin State at Co_3O_4 Crystalline-Amorphous Interfaces for CO Oxidation and N_2O Decomposition. *Nat. Commun.* **2025**, *16* (1), 1048.

(19) Kaczmarczyk, J.; Zasada, F.; Janas, J.; Indyka, P.; Piskorz, W.; Kotarba, A.; Sojka, Z. Thermodynamic Stability, Redox Properties, and Reactivity of Mn_3O_4, Fe_3O_4, and Co_3O_4 Model Catalysts for N_2O Decomposition: Resolving the Origins of Steady Turnover. *ACS Catal.* **2016**, *6* (2), 1235–1246.
(20) Kondratenko, E. V.; Pérez-Ramírez, J. Mechanism and Kinetics of Direct N_2O Decomposition over Fe-MFI Zeolites with Different Iron Speciation from Temporal Analysis of Products. *J. Phys. Chem. B* **2006**, *110* (45), 22586–22595.
(21) Zhuang, Z.; Guan, B.; Chen, J.; Zheng, C.; Zhou, J.; Su, T.; Chen, Y.; Zhu, C.; Hu, X.; Zhao, S.; Guo, J.; Dang, H.; Zhang, Y.; Yuan, Y.; Yi, C.; Xu, C.; Xu, B.; Zeng, W.; Li, Y.; Shi, K.; He, Y.; Wei, Z.; Huang, Z. Review of Nitrous Oxide Direct Catalytic Decomposition and Selective Catalytic Reduction Catalysts. *Chem. Eng. J.* **2024**, *486*.
(22) Zhang, X.; Shen, Q.; He, C.; Ma, C.; Cheng, J.; Li, L.; Hao, Z. Investigation of Selective Catalytic Reduction of N_2O by NH_3 over an Fe-Mordenite Catalyst: Reaction Mechanism and O_2 Effect. *ACS Catal.* **2012**, *2* (4), 512–520.
(23) Wang, A.; Wang, Y.; Walter, E. D.; Kukkadapu, R. K.; Guo, Y.; Lu, G.; Weber, R. S.; Wang, Y.; Peden, C. H. F.; Gao, F. Catalytic N_2O Decomposition and Reduction by NH_3 over Fe/Beta and Fe/SSZ-13 Catalysts. *J. Catal.* **2018**, *358*, 199–210.
(24) Cheng, J.; Zheng, D.; Yu, G.; Xu, R.; Dai, C.; Liu, N.; Wang, N.; Chen, B. N_2O Catalytic Decomposition and NH_3-SCR Coupling Reactions over Fe-SSZ-13 Catalyst: Mechanisms and Interactions Unraveling via Experiments and DFT Calculations. *ACS Catal.* **2023**, *13* (2), 934–947.
(25) Buttignol, F.; Garbujo, A.; Biasi, P.; Kröcher, O.; Ferri, D. N_2O Activation and NO Adsorption Control the Simultaneous Conversion of N_2O and NO Using NH_3 over Fe-ZSM-5. *J. Am. Chem. Soc.* **2025**, *147* (10), 8978.
(26) Beale, A. M.; Gao, F.; Lezcano-Gonzalez, I.; Peden, C. H. F.; Szanyi, J. Recent Advances in Automotive Catalysis for NOx Emission Control by Small-Pore Microporous Materials. *Chem. Soc. Rev.* **2015**, *44* (20), 7371–7405.
(27) Konsolakis, M. Recent Advances on Nitrous Oxide (N_2O) Decomposition over Non-Noble-Metal Oxide Catalysts: Catalytic Performance, Mechanistic Considerations, and Surface Chemistry Aspects. *ACS Catal.* **2015**, *5* (11), 6397–6421.
(28) Centi, G.; Perathoner, S.; Vazzana, F.; Marella, M.; Tomaselli, M.; Mantegazza, M. Novel Catalysts and Catalytic Technologies for N_2O Removal from Industrial Emissions Containing O_2, H_2O and SO_2. *Adv. Environ. Res.* **2000**, *4* (4), 325–338.
(29) Oi, J.; Obuchi, A.; Bamwenda, G. R.; Ogata, A.; Yagita, H.; Kushiyama, S.; Mizuno, K. Decomposition of Nitrous Oxide over Supported Rhodium Catalysts and Dependency on Feed Gas Composition. *Appl. Catal., B* **1997**, *12*, 277–286.
(30) Parres-Esclapez, S.; López-Suárez, F. E.; Bueno-López, A.; Illán-Gómez, M. J.; Ura, B.; Trawczynski, J. Rh-Sr/Al_2O_3 Catalyst for N_2O Decomposition in the Presence of O_2. *Top. Catal.* **2009**, *52* (13–20), 1832–1836.
(31) Hinokuma, S.; Iwasa, T.; Kon, Y.; Taketsugu, T.; Sato, K. N_2O Decomposition Properties of Ru Catalysts Supported on Various Oxide Materials and SnO_2. *Sci. Rep.* **2020**, *10* (1), 21605.
(32) Kim, M. J.; Kim, Y. J.; Lee, S. J.; Ryu, I. S.; Kim, H. J.; Kim, Y.; Ko, C. H.; Jeon, S. G. Enhanced Catalytic Activity of the Rh/Γ-Al_2O_3 Pellet Catalyst for N_2O Decomposition Using High Rh Dispersion Induced by Citric Acid. *Chem. Eng. Res. Des.* **2019**, *141*, 455–463.
(33) Jing, Y.; Taketoshi, K.; Zhang, N.; He, C.; Toyao, T.; Maeno, Z.; Ohori, T.; Ishikawa, N.; Shimizu, K. I. Catalytic Decomposition of N_2O in the Presence of O_2 through Redox of Rh Oxide in a RhO_x/ZrO_2 Catalyst. *ACS Catal.* **2022**, *12* (11), 6325–6333.
(34) Jing, Y.; He, C.; Zhang, N.; Murano, Y.; Toyoshima, R.; Kondoh, H.; Kageyama, Y.; Inomata, H.; Toyao, T.; Shimizu, K. I. Promotional Effect of Ag on the Catalytic Decomposition

of N_2O in the Presence of O_2 over the Al_2O_3-Supported Rh Catalyst. *ACS Catal.* **2023**, *13* (19), 12983–12993.
(35) Zhang, N.; He, C.; Jing, Y.; Qian, Y.; Obuchi, M.; Toyoshima, R.; Kondoh, H.; Oka, K.; Wu, B.; Li, L.; Anzai, A.; Toyao, T.; Shimizu, K. I. Enhanced Nitrous Oxide Decomposition on Zirconium-Supported Rhodium Catalysts by Iridium Augmentation. *Environ. Sci. Technol.* **2025**, *59* (3), 1598–1607.
(36) Zhang, N.; He, C.; Jing, Y.; Qian, Y.; Toyao, T.; Shimizu, K. ichi. Enhanced N_2O Decomposition on Rh/ZrO_2 Catalysts through the Promotional Effect of Palladium. *Surf. Interface* **2024**, *46*.
(37) Bao, S.; Lu, X.; Yu, L.; Song, Y.; Fu, H.; Qu, X.; Park, J. Y.; Zheng, S. Uniform and Fully Exposed Rh Clusters on Defect-Rich CeO_2 Enable Efficient Catalytic N_2O Decomposition. *Appl. Catal., A* **2025**, *693* (January), 120122.
(38) Mauvezin, M.; Delahay, G.; Coq, B.; Kieger, S. N_2O Decomposition in the Presence of Ammonia on Faujasite-Supported Metal Catalysts. *Appl. Catal., B* **1999**, *23* (2–3), 79–82.
(39) Campa, M. C.; Pietrogiacomi, D.; Scarfiello, C.; Carbone, L. R.; Occhiuzzi, M. CoO_x and FeO_x Supported on ZrO_2 for the Simultaneous Abatement of NO_x and N_2O with C_3H_6 in the Presence of O_2. *Appl. Catal., B* **2019**, *240* (x), 367–372.
(40) You, Y.; Chen, S.; Li, J.; Zeng, J.; Chang, H.; Ma, L.; Li, J. Low-Temperature Selective Catalytic Reduction of N_2O by CO over Fe-ZSM-5 Catalysts in the Presence of O_2. *J. Hazard. Mater.* **2020**, *383* (August 2019), 121117.
(41) Lin, B.; Guo, Z.; Tang, J.; Chen, P.; Ye, D.; Hu, Y. Modulating the Microstructure and Surface Acidity of MnO_2 by Doping-Induced Phase Transition for Simultaneous Removal of Toluene and NO_x at Low Temperature. *Environ. Sci. Technol.* **2024**, *58* (23), 10398–10408.
(42) Pérez-Ramírez, J.; Kapteijn, F.; Schöffel, K.; Moulijn, J. A. Formation and Control of N_2O in Nitric Acid Production: Where Do We Stand Today? *Appl. Catal., B* **2003**, *44* (2), 117–151.
(43) Yamaguchi, S.; Hu, P.; Ya, H.; Xiao, P.; Nakata, A.; Miyazaki, T.; Morikawa, Y.; Kondo, J. N.; Tange, K.; Tonokura, K.; Takemoto, M.; Yonezawa, Y.; Yokoi, T.; Iyoki, K.; Okubo, T.; Wakihara, T. Adsorption Behavior of Low-Concentration Nitrous Oxide on Natural Mordenite Zeolite. *Microporous and Mesoporous Materials* **2025**, *388*.
(44) Yue, B.; Lian, X.; Liu, S.; Wu, G.; Xu, J.; Li, L. Efficient Nitrous Oxide Capture by Cationic Forms of FAU and CHA Zeolites. *Chemical Engineering Journal* **2023**, *462*.
(45) Hiraki, S.; Baba, H.; Kobayashi, I.; Oda, A.; Ohkubo, T.; Ikemoto, Y.; Moriwaki, T.; Kuroda, Y. Excellent Capture of N2O Functioning at RT and Lower Pressure by Utilizing an NaCaA-85 Zeolite. *Chemical Communications* **2024**, *60* (34), 4597–4600.
(46) Meloni, E.; Martino, M.; Pierro, M.; Pullumbi, P.; Brandani, F.; Palma, V. MW-Assisted Regeneration of 13X Zeolites after N2O Adsorption from Concentrated Streams: A Process Intensification. *Energies (Basel)* **2022**, *15* (11).
(47) Saha, D.; Bao, Z. Adsorption of CO_2, CH_4, N_2O, and N_2 on MOF-5, MOF-177, and Zeolite 5A. *Environ. Sci. Technol.* **2010**, *44* (5), 1820–1826.
(48) Tolman, W. B. Binding and Activation of N_2O at Transition-Metal Centers: Recent Mechanistic Insights. *Angew. Chem. Int. Ed.* **2010**, *49* (6), 1018–1024.
(49) Yang, J.; Du, B.; Liu, J.; Krishna, R.; Zhang, F.; Zhou, W.; Wang, Y.; Li, J.; Chen, B. MIL-100Cr with Open Cr Sites for a Record N_2O Capture. *Chem. Commun.* **2018**, *54* (100), 14061–14064.
(50) Wu, T.; Shen, Y.; Feng, L.; Tang, Z.; Zhang, D. Adsorption Properties of N_2O on Zeolite 5A, 13X, Activated Carbon, ZSM-5, and Silica Gel. *J. Chem. Eng. Data* **2019**, *64* (8), 3473–3482.

(51) Yamashita, K.; Liu, Z.; Iyoki, K.; Chen, C. T.; Miyagi, S.; Yanaba, Y.; Yamauchi, Y.; Okubo, T.; Wakihara, T. Synthetic and Natural MOR Zeolites as High-Capacity Adsorbents for the Removal of Nitrous Oxide. *Chem. Commun.* **2021**, *57* (11), 1312–1315.
(52) Jing, Y.; He, C.; Wan, L.; Tong, J.; Zhang, J.; Mine, S.; Zhang, N.; Kageyama, Y.; Inomata, H.; Shimizu, K. I.; Toyao, T. Continuous N_2O Capture and Reduction to N_2 Using Ca-Zeolite Adsorbent and Pd/La/Al_2O_3 Reduction Catalyst. *ACS EST Engg.* **2024**.
(53) Ballesteros-Plata, D.; Cecilia, J. A.; Barroso-Martín, I.; Jiménez-Jiménez, J.; Infantes-Molina, A.; Rodríguez-Castellón, E. Materials Design for N_2O Capture: Separation in Gas Mixtures. *Catalysts*. MDPI December 1, 2022.
(54) Denysenko, D.; Jelic, J.; Magdysyuk, O. V.; Reuter, K.; Volkmer, D. Elucidating Lewis Acidity of Metal Sites in MFU-4l Metal-Organic Frameworks: N_2O and CO_2 Adsorption in MFU-4l, CuI-MFU-4l and Li-MFU-4l. *Microporous Mesoporous Mater.* **2015**, *216*, 146–150.
(55) Wang, L.; Lin, C.; Boldog, I.; Yang, J.; Janiak, C.; Li, J. Inverse Adsorption Separation of N_2O/CO_2 in AgZK-5 Zeolite. *Angew. Chem. Int. Ed.* **2024**, *63* (4).
(56) Zhang, X.; Chen, W.; Shi, W.; Cheng, P. Highly Selective Sorption of CO_2 and N_2O and Strong Gas-Framework Interactions in a Nickel(II) Organic Material. *J. Mater. Chem. A* **2016**, *4* (41), 16198–16204.
(57) Wang, L.; Li, Y.; Wang, Y.; Yang, J.; Li, L.; Li, J. Research on CO_2-N_2O Separation Using Flexible Metal Organic Frameworks. *Sep. Purif. Technol.* **2020**, *251*.
(58) Kar, S.; Goeppert, A.; Prakash, G. K. S. Integrated CO_2 Capture and Conversion to Formate and Methanol: Connecting Two Threads. *Acc Chem Res* **2019**, *52* (10), 2892–2903.
(59) González-Castaño, M.; Dorneanu, B.; Arellano-García, H. The Reverse Water Gas Shift Reaction: A Process Systems Engineering Perspective. *React Chem Eng* **2021**, *6*, 954–976.
(60) Kosaka, F.; Liu, Y.; Chen, S. Y.; Mochizuki, T.; Takagi, H.; Urakawa, A.; Kuramoto, K. Enhanced Activity of Integrated CO_2 Capture and Reduction to CH_4 under Pressurized Conditions toward Atmospheric CO_2 Utilization. *ACS Sustain Chem Eng* **2021**, *9* (9), 3452–3463.
(61) Li, L.; Wu, Z.; Miyazaki, S.; Toyao, T.; Maeno, Z.; Shimizu, K. Continuous CO_2 Capture and Methanation over Ni-Ca/Al_2O_3 Dual Functional Materials. *RSC Adv* **2023**, *13* (4), 2213–2219.
(62) Li, L.; Miyazaki, S.; Wu, Z.; Toyao, T.; Selyanchyn, R.; Maeno, Z.; Fujikawa, S.; Shimizu, K. Continuous Direct Air Capture and Methanation Using Combined System of Membrane-Based CO_2 Capture and Ni-Ca Based Dual Functional Materials. *Appl Catal B* **2023**, *339*, 123151.
(63) Jing, Y.; Cai, Z.; Liu, C.; Toyao, T.; Maeno, Z.; Asakura, H.; Hiwasa, S.; Nagaoka, S.; Kondoh, H.; Shimizu, K. Promotional Effect of La in the Three-Way Catalysis of La-Loaded Al_2O_3-Supported Pd Catalysts (Pd/La/Al_2O_3). *ACS Catal* **2020**, *10*, 1010–1023.
(64) Horiuchi, Y.; Toyao, T.; Fujiwaki, M.; Dohshi, S.; Kim, T. H.; Matsuoka, M. Zeolitic Imidazolate Frameworks as Heterogeneous Catalysts for a One-Pot P-C Bond Formation Reaction via Knoevenagel Condensation and Phospha-Michael Addition. *RSC Adv.* **2015**, *5* (31), 24687–24690.
(65) Toyao, T.; Fujiwaki, M.; Miyahara, K.; Kim, T. H.; Horiuchi, Y.; Matsuoka, M. Design of Zeolitic Imidazolate Framework Derived Nitrogen-Doped Nanoporous Carbons Containing Metal Species for Carbon Dioxide Fixation Reactions. *ChemSusChem* **2015**, *8* (22), 3905–3912.
(66) Toyao, T.; Miyahara, K.; Fujiwaki, M.; Kim, T. H.; Dohshi, S.; Horiuchi, Y.; Matsuoka, M. Immobilization of Cu Complex into Zr-Based MOF with Bipyridine Units for Heterogeneous Selective Oxidation. *J. Phys. Chem. C* **2015**, *119* (15), 8131–8137.

(67) Abou-Elyazed, A. S.; Ftooh, A. I.; Sun, Y.; Ashry, A. G.; Shaban, A. K. F.; El-Nahas, A. M.; Yousif, A. M. Solvent-Free Synthesis of HKUST-1 with Abundant Defect Sites and Its Catalytic Performance in the Esterification Reaction of Oleic Acid. *ACS Omega* **2024**, *9* (36), 37662–37671.
(68) Godiksen, A.; Stappen, F. N.; Vennestrøm, P. N. R.; Giordanino, F.; Rasmussen, S. B.; Lundegaard, L. F.; Mossin, S. Coordination Environment of Copper Sites in Cu-CHA Zeolite Investigated by Electron Paramagnetic Resonance. *J. Phys. Chem. C* **2014**, *118* (40), 23126–23138.
(69) Mazur, M. A Dozen Useful Tips on How to Minimise the Influence of Sources of Error in Quantitative Electron Paramagnetic Resonance (EPR) Spectroscopy - A Review. *Anal Chim Acta* **2006**, *561* (1–2), 1–15.
(70) Czoch, R. Quantitative EPR - Sensitivity to Experimental Conditions and Optimal Setting of Recording Parameters. *Appl Magn Reson* **1996**, *10* (1–3), 293–317.
(71) Siddiqui, H.; Parra, M. R.; Qureshi, M. S.; Malik, M. M.; Haque, F. Z. Studies of Structural, Optical, and Electrical Properties Associated with Defects in Sodium-Doped Copper Oxide (CuO/Na) Nanostructures. *J. Mater. Sci.* **2018**, *53* (12), 8826–8843.
(72) Pakharukova, V. P.; Moroz, E. M.; Zyuzin, D. A.; Ishchenko, A. V.; Dolgikh, L. Y.; Strizhak, P. E. Structure of Copper Oxide Species Supported on Monoclinic Zirconia. *J. Phys. Chem. C* **2015**, *119* (52), 28828–28835.
(73) Oruç, Ç.; Altındal, A. Structural and Dielectric Properties of CuO Nanoparticles. *Ceram. Int.* **2017**, *43* (14), 10708–10714.
(74) Sushkevich, V. L.; Safonova, O. V.; Palagin, D.; Newton, M. A.; van Bokhoven, J. A. Structure of Copper Sites in Zeolites Examined by Fourier and Wavelet Transform Analysis of EXAFS. *Chem. Sci.* **2020**, *11* (20), 5299–5312.
(75) Lamberti, C.; van Bokhoven, J. A. *X-Ray Absorption and Emission Spectroscopy for Catalysis*; 2015; Vol. 2–2.
(76) Borfecchia, E.; Pappas, D. K.; Dyballa, M.; Lomachenko, K. A.; Negri, C.; Signorile, M.; Berlier, G. Evolution of Active Sites during Selective Oxidation of Methane to Methanol over Cu-CHA and Cu-MOR Zeolites as Monitored by Operando XAS. *Catal. Today* **2019**, *333* (July 2018), 17–27.
(77) Godiksen, A.; Vennestrøm, P. N. R.; Rasmussen, S. B.; Mossin, S. Identification and Quantification of Copper Sites in Zeolites by Electron Paramagnetic Resonance Spectroscopy. *Top. Catal.* **2017**, *60* (1–2), 13–29.
(78) Bruzzese, P. C.; Salvadori, E.; Jäger, S.; Hartmann, M.; Civalleri, B.; Pöppl, A.; Chiesa, M. 17O-EPR Determination of the Structure and Dynamics of Copper Single-Metal Sites in Zeolites. *Nat. Commun.* **2021**, *12* (1).
(79) Brenig, A.; Fischer, J. W. A.; Klose, D.; Jeschke, G.; van Bokhoven, J. A.; Sushkevich, V. L. Redox and Kinetic Properties of Composition-Dependent Active Sites in Copper-Exchanged Chabazite for Direct Methane-to-Methanol Oxidation. *Angew. Chem. Int. Ed.* **2024**, No. x.
(80) Bruzzese, P. C.; Salvadori, E.; Civalleri, B.; Jäger, S.; Hartmann, M.; Pöppl, A.; Chiesa, M. The Structure of Monomeric Hydroxo-CuIISpecies in Cu-CHA. A Quantitative Assessment. *J. Am. Chem. Soc.* **2022**, *144* (29), 13079–13083.

Chapter 5

General conclusion

In this work, I focused on developing catalysts and capture–reduction processes for N_2O abatement. By combing advanced data science and *in situ* characterizations, we not only discovered the high-performance catalysts for direct N_2O decomposition, but also uncovered the roles of each element in contributing to superior activity. Considering high temperatures required to decompose N_2O in complex exhaust-gas mixtures, we developed an N_2O capture and reduction system that uses zeolite-based materials as N_2O adsorbents and Pd nanoparticles on La-containing Al_2O_3 ($Pd/La/Al_2O_3$) as the reduction catalyst. The main conclusions are summarized as follows:

Chapter 2 introduces a machine learning (ML)-assisted discovery strategy using experimentally measured performance under controlled conditions and extensive closed-loop ML–experiment iterations to develop efficient catalysts for direct N_2O decomposition. Starting with an initial dataset of 51 catalysts, we performed 37 cycles of the closed-loop discovery system (ML prediction + experiment) and experimentally tested 633 catalysts. The composition of the best catalyst identified by this approach was $Rh(1)–Pd(2)/ZrO_2$_EP with a T_{20} (the temperature required for 20% N_2O conversion during the light-off experiment) of 355 °C. Experimental mechanistic studies using *in situ* techniques were also performed to elucidate the role of each catalyst component and the reaction mechanism. The obtained results indicated that RhO_x acts as a redox species, whereas PdO_x facilitates the redox reaction of RhO_x under steady-state conditions.

Chapter 3 displays a continuous N_2O capture and reduction system that uses CaO-incorporated zeolite (Ca-zeolite) as the N_2O adsorbent and $Pd/La/Al_2O_3$ as the reduction catalyst. This process is suitable for continuous operation under temperature-swing cycles between 50 and 150 °C, and the N_2O capture and subsequent reduction performance was preserved for at least 15 h (10 cycles). Notably, this process can operate at low temperatures (below 150 °C) through a simple temperature-swing operation in the presence of O_2.

Chapter 4 describes the high selective adsorption of N_2O in the presence of O_2 and CO_2 over a CHA-type zeolite loaded with 10 wt.% Cu (Cu(10)/CHA(11)). Utilizing Cu(10)/CHA(11) as an adsorbent, the continuous N_2O capture and reduction system was employed and reliably maintained its N_2O adsorption and reduction performance for at least 12 h. The nature of the active Cu species contributed to the N_2O adsorption in Cu(10)/CHA(11) was also investigated. We found that Cu species should be neither too small nor too large to be effective. CHA zeolites are essential for the formation of effective adsorption sites.

Acknowledgement

I would like to extend my deepest gratitude to my supervisor, Prof. Ken-ichi Shimizu, for providing me with the opportunity to be a part of his laboratory and for generously sharing his knowledge and expertise. My sincere appreciation goes to Prof. Takashi Toyao for his daily support and excellent supervision throughout my research. I am also grateful to Prof. Akihiko Anzai for his valuable advice and kind assistance. Under the guidance of Prof. Shimizu, Prof. Toyao and Prof. Anzai, I have grown significantly in scientific critical thinking, experimental skills, and achievement presentation.

I am also extremely grateful to Prof. Ichigaku Takigawa from Hokkaido University, Prof. Hiroshi Kondoh from Keio University, Lecturer. Ryo Toyoshima from the University of Tokyo, Prof. Ningqiang Zhang from Northeastern University, as well as Dr. Shinya Mine and Dr. Yuan Jing, postdoctoral fellows from the Shimizu Lab, for their technical expertise, which made this work possible.

I would also like to acknowledge the Advanced Graduate School and EXEX Doctoral Fellowship of Hokkaido University for providing me with the valuable opportunity and financial support to obtain my PhD degree.

I am thankful to all other members of Prof. Shimizu's laboratory for their assistance and camaraderie.

Chenxi He